High-performance FMCW LiDAR with MEMS Optical Beam Scanner

Xiaosheng Zhang

Electrical Engineering and Computer Sciences
University of California, Berkeley

Technical Report No. UCB/EECS-2023-26
http://www2.eecs.berkeley.edu/Pubs/TechRpts/2023/EECS-2023-26.html

May 1, 2023

High-performance FMCW LiDAR with MEMS Optical Beam Scanner

By

Xiaosheng Zhang

A dissertation submitted in partial satisfaction of the

requirements for the degree of

Doctor of Philosophy

in

Engineering – Electrical Engineering and Computer Sciences

in the

Graduate Division

of the

University of California, Berkeley

Committee in charge:

Professor Ming C. Wu, Chair
Professor Vladimir Stojanovic
Professor Austin Roorda

Summer 2021

High-performance FMCW LiDAR with MEMS Optical Beam Scanner

Xiaosheng Zhang

Abstract

High-performance FMCW LiDAR with MEMS Optical Beam Scanner

by

Xiaosheng Zhang

Doctor of Philosophy in Engineering – Electrical Engineering and Computer Sciences

University of California, Berkeley

Professor Ming C. Wu, Chair

3D imaging sensors are crucial components for modern intelligent machines to detect and perceive the surrounding world. Among different 3D sensing technologies, light detection and ranging (LiDAR) systems offer high distance and lateral resolutions and are able to work in darkness, therefore have applications that span several industries and markets, from metrology, robotic control, autonomous vehicles, to consumer electronics.

Compared with other LiDAR principles such as the pulsed time-of-flight, frequency-modulated continuous-wave (FMCW) LiDAR can achieve high-resolution distance and velocity measurements without fast electronics or high peak optical power thanks to the coherent detection advantages, but it typically requires narrow-linewidth lasers with complex feedback circuits to generate linear chirps. In this dissertation, we will summarize our research on linearizing the laser chirp by iterative learning pre-distortion of the drive waveform and compensating for the laser phase noise in post-processing. With these two methods, high-performance FMCW LiDAR can be achieved with commercial semiconductor lasers and a simple setup.

Besides the laser ranging system, the optical beam scanner is an essential component in scanning LiDAR. An integrated optical beam scanner with fast speed, large field-of-view, high resolution, and low power consumption is an essential element for solid-state LiDAR. In this dissertation, we will introduce two integrated beam scanner architectures based on micro-electromechanical system (MEMS), (1) grating-based 2D optical phased array (OPA), and (2) 2D focal plane switch array (FPSA) with MEMS optical switches. We will discuss their operation principles as well as the advantages and challenges, and we will show the design, fabrication, and characterization of a 160×160-element OPA, a 20×20-element FPSA, and a 128×128-element FPSA. We will also demonstrate the implementation of the 128×128-element FPSA beam scanner on an FMCW LiDAR for 3D imaging. We believe these highly scalable integrated beam scanners are very promising candidates for chip-scale solid-state LiDAR sensors.

To my parents

Table of Contents

List of Figures

List of Tables

List of Symbols

Symbol	Description	Unit
A	Amplitude	–
B	Bandwidth	Hz or nm
C	Constant coefficient	–
c	Speed of light	m/s
d	Object distance	m
d_{rx}	Receiver optical aperture diameter	m
E	Electrical field	V/m
e	Elementary charge	C
F	Force	N
f	Focal length	m
f	Frequency	Hz
f_{b}	Beat frequency	Hz
f_{D}	Doppler frequency shift	Hz
f_{s}	ADC sample rate	Samples/s
g	Gap	m
G_{TIA}	TIA gain	V/A
I	Current	A
i	Imaginary unit	–
k	Wavenumber	1/m
k_{B}	Boltzmann constant	J/K
k_{s}	Spring constant	N/m
L	Array size	m
l	Array pitch	m
N, n	An integer	–
P	Optical power	W
q	Gaussian beam complex beam parameter	m
R	Gaussian beam phase front radius of curvature	m
R	Photodiode responsivity	A/W
r_{CMRR}	Common-mode rejection ratio	–
r_{ref}	Power split ratio to reference path	–

Symbol	Description	Unit
S	Power spectral density	W/Hz
T	Laser chirp duration	s
t	Thickness	m
t	Time	s
T_{temp}	Temperature	K
$u(t)$	Laser drive waveform	V or A
V	Object velocity	m/s
V	Voltage	V
V_{ADC}	ADC voltage range	V
W	Grating/antenna size	m
w	Beam radius	m
x, y, z	Coordinates	m
α, θ	Angle	degree or rad
γ	Laser chirp rate	Hz/s
δd	Distance resolution	m
δV	Velocity resolution	m/s
Δx	Displacement	m
Δv	Laser frequency excursion	Hz
ε	Permittivity	F/m
η	Optical efficiency	–
Λ	Grating period	m
λ	Wavelength	m
ξ	Spatial frequency	1/m
ρ	Object reflectivity	–
σ	Amplitude spectral density	$\text{V/Hz}^{-1/2}$
τ	Roundtrip light travel time to the object	s
τ_{c}	Laser coherence time	s
τ_{m}	Monitor MZI delay	s
φ	Phase	rad

Abbreviation	Description
ADC	Analog-to-digital converter
AMCW	Amplitude-modulated continuous-wave
AR/VR	Augmented reality and virtual reality
ASD	Amplitude spectral density
BPD	Balanced photodetectors
CMOS	Complementary metal-oxide-semiconductor
CMRR	Common-mode rejection ratio
DFB	Distributed feedback
EDFA	Erbium-doped fiber amplifier
FDTD	Finite-difference time-domain
FFT	Fast Fourier Transform
FMCW	Frequency-modulated continuous-wave
FoV	Field-of-view
FPGA	Field-programmable gate array
FPSA	Focal plane switch array
FT	Fourier Transform
FWHM	Full-width half-maximum
GPS	Global positioning system
HT	Hilbert Transform
IR	Infrared
LiDAR	Light detection and ranging
MEMS	Micro-electromechanical system
MSSR	Main-to-side lobe suppression ratio
MZI	Mach-Zehnder interferometer
MZM	Mach-Zehnder modulator
OCT	Optical coherence tomography
OFDR	Optical frequency domain reflectometry
OPA	Optical phased array
PC	Personal computer
PCB	Printed circuit board
PGA	Pin grid array
PSD	Power spectral density

Abbreviation	Description
RCWA	Rigorous coupled-wave analysis
Ref	Reference
RF	Radio frequency
RIN	Relative intensity noise
RMCW	Random-modulated continuous-wave
RMS	Root-mean-square
ROI	Region of interest
Rx	Receive
SEM	Scanning electron microscope
SiN	Silicon nitride
SNR	Signal-to-noise ratio
SOI	Silicon-on-insulator
SSOCT	Swept-source optical coherence tomography
TIA	Trans-impedance amplifier
ToF	Time-of-flight
Tx	Transmit

Acknowledgments

I would like to express my great gratitude to my advisor Professor Ming C. Wu. The memories of our first meetings shortly after I received the offer from UC Berkeley are still fresh, and I really enjoy the four-year graduate school journey working with him. His profound knowledge, extensive experiences, sharp insights, constant guidance, and openness to new ideas are invaluable for my growth and progress. I also want to thank my qualifying exam and dissertation committee members Professor Vladimir Stojanovic, Professor Austin Roorda, and Professor Avideh Zakhor for their support and feedback.

I would like to especially thank all the members of the Integrated Photonics Lab. My mentors Dr. Phillip Sandborn and Dr. Youmin Wang led me into the research on LiDAR and beam scanners. Dr. Kyungmok Kwon has the excellent skills to cook the best devices in the cleanroom and the best barbecue at home. Johannes Henriksson, Jianheng Luo, and Dr. Tae Joon Seok know the science and art to design cutting-edge MEMS optical switches. Dr. Guan-Lin Su and Dr. Jean-Etienne Tremblay have provided precious advice on device design, packaging, and test. Dr. Jodi Loo, Dr. Nicolas Andrade, and Philip Jacobson are great fellow lab safety officers. Jazz Pouls, Margaret Zhang, and Musaiel Gebremariam made their important contributions to the research projects as undergraduate researchers. I also enjoy the time working and talking with my officemates from the Chang-Hasnain Group, the Kante Group, and the Yablonovitch Group.

I would like to thank my fellow EECS students and friends Xiaoer Hu, Shiekh Zia Uddin, Jianheng Luo, and Jonathan Tyler Reichanadter for spending time together preparing the preliminary exam, discussing literature and research projects, and chatting about graduate school life. I would like to thank the Berkeley Sensor and Actuator Center (BSAC) for funding the research projects and building the bridge between academia and industry. I also want to thank Shirley Salanio, Therese George, and all the EECS and ERSO staff for their help and support.

I am very lucky and grateful to enjoy the journey from college to graduate school then to the future together with Heyin. You make my life happy and bright. I look forward to celebrating your graduation in the near future. I love you.

Last but the most, I want to share the happiness of reaching this important milestone with my parents. Thank you Mom and Dad for everything you did for me and with me. You are always my role models. This dissertation is dedicated to you.

1 Introduction

1.1 3D imaging sensors

1.1.1 Motivation and demand for 3D imaging sensors

As human beings, our senses of sight, hearing, and touch give us an understanding of the surrounding world. We see the scene around us, hear the sound, touch the surfaces, and then perceive the important physical quantities of each object, for example, location, distance, speed, shape, color, etc. With this information, we are able to classify the objects, predict their behavior, and make decisions on our own reactions.

With the development of integrated circuits and computer sciences, modern machines are no longer only performing repetitive work according to straightforward commands from humans. Instead, they are expected to be intelligent and autonomous, i.e. to be able to process information, make their own decisions, and accomplish complicated tasks with fast response, low cost, no mistake, and little human supervision. This requires machines to sense and perceive the surroundings like human beings. For example, a robot needs to detect the locations of objects of interest and the barriers along its path, an autonomous vehicle needs to know the movement of pedestrians and other vehicles, and a smartphone needs to recognize the user's face and even gestures. All these functions require 3D imaging sensors that detect the 3D coordinates of objects and surfaces, which help machines reconstruct a 3D model of the surrounding scene and extract useful information for their decision-making.

Nowadays 3D imaging sensors have been widely used for many applications from scientific research, industrial metrology, autonomous robots, vehicles, and aircraft, to consumer electronics [1]. Although different applications emphasize different aspects of the 3D sensor specifications, most of them are demanding a long detection range, high resolution and accuracy, large field-of-view (FoV), and high frame rate with reasonable size, cost, and power consumption. These applications and demands motivate the research and development of 3D imaging sensors with a variety of working principles.

1.1.2 3D imaging sensor technologies

Common 3D imaging sensors include camera-based sensors, ultrasonic sensors, radio detection and ranging (radar) sensors, and light detection and ranging (LiDAR) sensors. A comparison of them is summarized in Table 1-1. Each sensor has distinct advantages and disadvantages, and a machine may require a fusion of multiple types of sensors to realize the desired 3D imaging range and resolution.

2D photography with cameras has been invented for about two hundred years, and digital camera sensors have now become the standard feature of almost all cellphones and laptop computers. Cameras are cheap and compact thanks to the mature complementary metal-oxide-semiconductor (CMOS) image sensor technology, and they can provide additional color information of objects. To detect 3D coordinates, i.e. add depth information to 2D camera images, two or more cameras located at some distances away from each other can form a stereo vision system and depth can be solved from the relative positions of the same object on the images taken by different cameras, similar to the stereoscopic vision of humans [2]. However,

the depth resolution of stereo vision systems degrades when the object distance increases and when the distances between cameras decrease. With the development of computer vision and deep neural networks, recent research works have shown that depth information can also be assigned to a single 2D camera image by analyzing the layout of the scene and learning from similar training images [3].

Table 1-1. Comparison of 3D imaging sensor technologies

Technology	Range	Resolution	Cost	Advantages
Camera	Short/Medium	Medium	Low	Color information Technology maturity
Structured light	Short/Medium	Medium/High	Medium	Improved resolution versus camera
Ultrasonic	Short	Medium	Low	Low cost
Radar	Long	Low	Medium	Works in bad weather and darkness
LiDAR	Medium/Long	High	High	Works in darkness Velocity information

3D sensing by a single camera can also be achieved by actively project some illumination patterns on the object, for example, an array of dots, stripes, or checkerboard patterns. By analyzing the distortion of the pattern in the captured image, the depth variation of the object surface can be derived [4]. This is typically called structured light technology, and one of the famous applications is the Face ID facial recognition system. Structured light technology offers improved depth resolution and is a good solution for 3D surface reconstruction in a short to medium distance range.

Ultrasonic sensors detect object distance by measuring the travel time of the transmitted and reflected ultrasonic wave. They are widely used for short-range obstacle detection such as the proximity sensors around the cars. 3D imaging can be achieved by using an array of ultrasonic sensors or steering the direction of the transmitting ultrasonic wave [5].

Radar was invented in the early 20th century and is now widely used in applications from aviation, meteorology, to the automobile [6]. Radar measures object distance using electromagnetic waves in the radio frequency (RF) range on the order of 0.1 – 100 GHz. 3D imaging can be achieved by scanning the beam. Thanks to the relatively long wavelength, the radio wave is able to penetrate common weather conditions such as fog, cloud, and rain, therefore radar can achieve long-distance detection and can work in bad weather as well as in darkness. However, the long wavelength also leads to lower detection resolution in the longitudinal and lateral directions, therefore details of object shape may not be detected by a radar sensor.

Similar to radar, LiDAR also works with electromagnetic waves but operates in the optical frequency range on the order of 100 THz. Due to the short light wavelength and high collimation of the laser source, LiDAR can achieve high resolution in both the longitudinal and lateral directions [7]. The cost of LiDAR is still higher than other types of 3D imaging sensors due to

the complex system design, expensive components, and lack of integration. However, the recent development of silicon photonics and micro-electromechanical systems (MEMS) technologies opens up some promising routes towards compact and low-cost LiDAR sensors, and some of them will be discussed in this dissertation.

1.2 Light detection and ranging (LiDAR) systems

1.2.1 LiDAR overview

The speed of electromagnetic wave (speed of light) c, the light travel time τ, and the light travel distance d, satisfy the simple equation $d = c\tau$. Back in the 19th century, this relation was used to determine the speed of light by measuring the light travel time over a very long distance due to the extremely high speed. Since then the speed of light had been measured with higher and higher precision, and multiple theories and experiments in physics had shown that it is a constant. In 1983 the speed of light in the vacuum was eventually defined as a constant c = 299,792,458 m/s [8]. This directly connects the definitions of the SI units of length and time, i.e. meter and second, and has become the most important approach in metrology to precisely link the length measurements to the cesium atomic clock standard, i.e. the definition of second, with the development of the optical frequency comb technology in recent decades [9].

Converting distance measurements to time measurements by the traveling electromagnetic waves was first realized in the radio frequency range with the invention of radar. Moving from radio frequency to optical frequency offers significant resolution improvement due to the much shorter optical wavelength. With the invention of the laser, practical light ranging systems were realized in the 1960s, and the first applications span from satellite tracking, cloud monitoring, to moon surface mapping in the Apollo missions.

A schematic of a LiDAR system is shown in Figure 1-1. Light emitted from the laser is sent to the object via the transmitter. The reflected or scattered light from the object is received by the receiver and the detector. By counting the roundtrip light travel time τ, the distance from the LiDAR to the object can be determined by $d = c\tau/2$. Although the figure shows transmitting and receiving using separate optical apertures, they can also share the same aperture. To capture the 3D image of the entire object instead of a single point, the output light needs to be transmitted to different directions by an optical beam scanner, a laser emitter array, or flood illumination. These different configurations will be discussed in section 1.2.2.

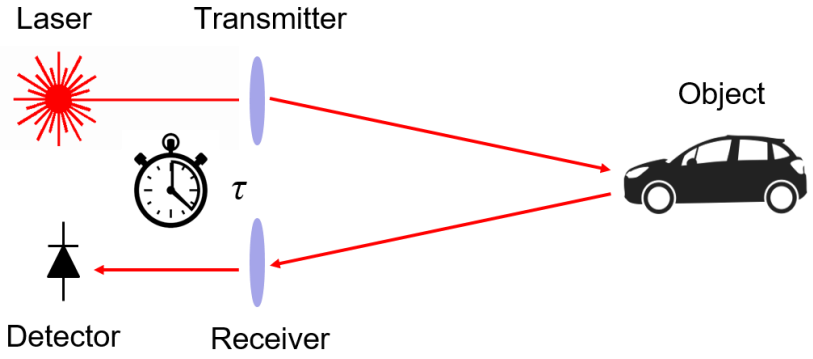

Figure 1-1. Schematic of LiDAR.

The fast speed of light means the transmitted light will return in a very short time. For example, the roundtrip time for an object at 150 m away is about 1 μs. This introduces both advantages and challenges for a LiDAR system. On the one hand, the frame rate can be fast since for each measurement the receiver only needs to wait for the returned signal for a short time. On the other hand, the system needs to be able to measure this short time with high accuracy, where nanosecond to picosecond level timing resolution is usually required. While directly counting the time by fast electronics is a feasible and common approach, converting the time to other properties of light waves, such as the amplitude, frequency, and phase, often helps mitigate the detection bandwidth requirement and offers other special advantages. The ranging principles of LiDAR will be discussed in section 1.2.3.

Although the speed of light in the vacuum is a defined constant, most LiDAR systems operate in the atmosphere, therefore the speed of light in air, or the refractive index of air, is one of the important parameters to be considered. The refractive index of air is approximately 1.0003 and it varies depending on atmospheric parameters such as temperature, pressure, and humidity [10]. For metrology applications where high-precision absolute distance measurements are desired, the speed of light in the air needs to be calculated from the atmospheric conditions. However, in most practical applications, the difference between the speed in the vacuum and air is negligible, and the speed of light can simply be approximated using the vacuum value.

1.2.2 LiDAR configurations

LiDAR systems can be classified from different perspectives, one of which is the transmitting and receiving apertures. Figure 1-2 shows schematics of a bistatic LiDAR, where the transmitter and receiver use separate optical apertures, and a monostatic LiDAR, where the transmitter and receiver share the same optical aperture.

The bistatic configuration offers flexibility in the transmitter and receiver designs. Different transmitter and receiver architectures can be implemented, and a larger receiver aperture can be used to capture more returned optical power. In addition, the reflection from optical components in the transmitter will not be captured by the receiver, resulting in a cleaner received signal. On the other hand, the monostatic configuration can be more compact with only one optical aperture. More importantly, it does not require optical alignment and numerical aperture matching between the transmitter and the receiver, eliminating the requirement of special beam scanner designs or complex alignment procedures. Both configurations have been successfully implemented on practical LiDAR systems, and the selection depends on the transmitter and receiver designs, and the LiDAR link budget.

LiDAR systems can also be classified from the beam scanner and detector configurations, shown in Figure 1-3. A scanning LiDAR outputs a laser beam and measures the distance in one direction at each time, and the beam direction is steered by an optical beam scanner to capture the entire object. The received light is detected by a single-point photodetector. A flash LiDAR illuminates the entire object by the light at the same time like the flash on a camera, called flood illumination, and a 2D detector array detects the returned light from different points on the object to reconstruct the 3D image. The flood illumination can also be achieved by an array of laser emitters.

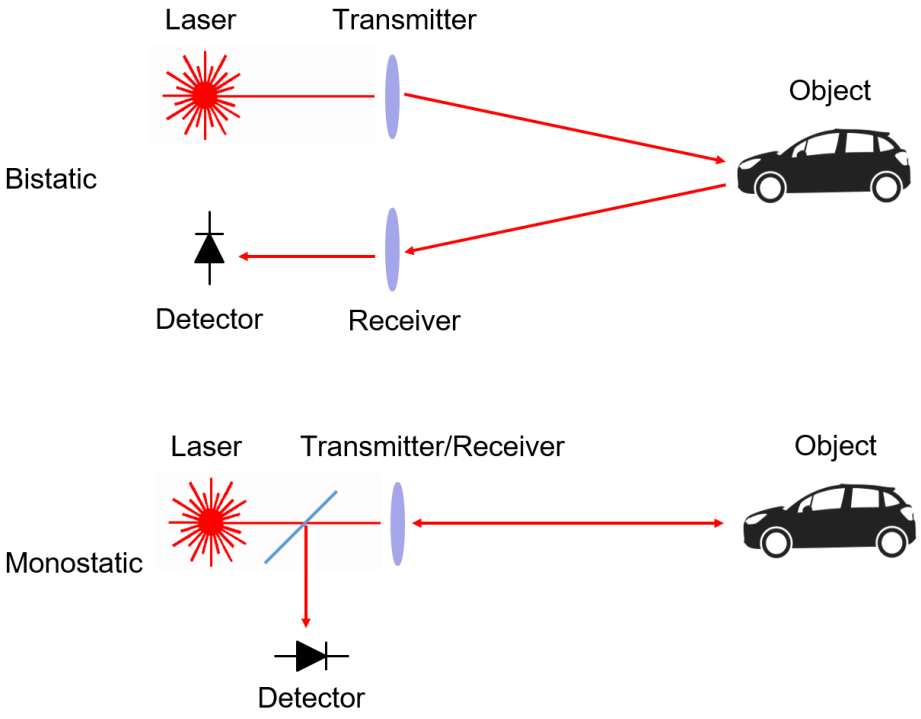

Figure 1-2. Bistatic and monostatic LiDAR configurations.

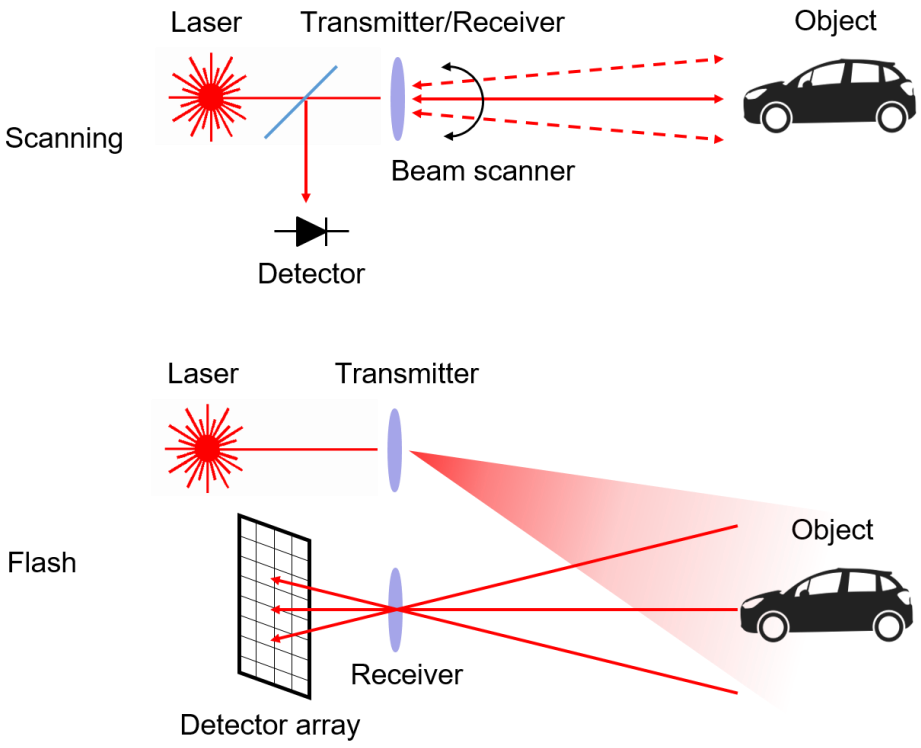

Figure 1-3. Scanning LiDAR and flash LiDAR.

Compared with the flash LiDAR where the optical power is distributed to the entire scene, the scanning LiDAR concentrates all the optical power in one direction. With a certain amount of optical power it can detect objects at a longer distance or with lower reflectivity, thus is suitable for LiDAR sensors on autonomous vehicles and aircraft. The flash LiDAR can achieve a fast frame rate due to the parallel operation without the need to scan the output beam, thus it is widely used for short-range LiDAR sensors on consumer electronics.

Both the scanning LiDAR and flash LiDAR have key components that are crucial for their performance and are under intensive research and development. The 2D detector array in flash LiDAR needs to have high sensitivity and fast readout. Time-of-flight flash LiDAR typically requires a single photon detector array. For the scanning LiDAR, an optical beam scanner with fast speed, large FoV, high resolution, and low power consumption is usually desired, which will be one of the main topics of this dissertation.

1.2.3 Ranging principles

In general, in a LiDAR sensor, the object distance d is computed from the roundtrip time τ according to $d = c\tau/2$. However, the roundtrip time τ can be measured in multiple different ways, and some common ranging principles are discussed below and shown in Figure 1-4.

By transmitting pulsed light, the roundtrip time can be counted directly by an electronic clock. This ranging principle is called the pulsed time-of-flight (ToF) or direct ToF [11]. The transmitted pulse triggers the start of the timer, and the received pulse triggers the stop of the timer. Due to the high speed of light, the clock needs to be fast to achieve a high distance resolution, which requires large circuit bandwidth. For example, a 0.1 ns clock resolution (10 GHz bandwidth) is required for a 1.5 cm distance resolution. The pulsed ToF method can be implemented on a simple optical setup, typically using an avalanche photodiode or single-photon detector as the receiver. The system is vulnerable to ambient light or light transmitted from other LiDAR units since the interference light can potentially trigger the timer and become a false target. Multiple different approaches have been reported to solve this issue, including adding a band pass optical filter at the receiver to filter out ambient light, measuring the same point by multiple pulses to obtain the distance from the histogram, and modulating the transmitted pulse by a unique code. The pulsed ToF method has been widely used in commercial LiDAR systems due to its straightforward principle and relatively simple setup.

A mode-locked laser can generate a pulse train with a stable repetition period and short pulse width thus can be used as an advanced light source for a pulsed ToF LiDAR. Instead of direct detection of the received light intensity, coherent detection can be employed to align the transmitted pulse with a time-delayed received pulse and measure the roundtrip time precisely thanks to the coherence among pulses generated by a mode-locked laser. Wavelength level distance resolution can be achieved [12].

The roundtrip time information can be converted to other properties of the light wave. An amplitude-modulated continuous-wave (AMCW) LiDAR transmits a light wave that is amplitude modulated, typically in a sinusoidal fashion [13]. The received light from the object has the same amplitude modulation, with an envelope phase delay due to the light travel time. The sinusoidal amplitude modulation on a continuous-wave laser is easy to generate, and the phase difference can be measured by an analog circuit such as an RF mixer and a low-pass filter, therefore the AMCW method has a simple setup and is commonly used in commercial laser range finder

products. However, the 2π ambiguity of phase measurement introduces a tradeoff between range and resolution for an AMCW LiDAR. To increase the distance resolution, the amplitude modulation frequency needs to be increased, resulting in a shorter envelope wavelength thus a shorter unambiguous range. This issue can be solved by measuring the same object using multiple different modulation frequencies, at the cost of measurement speed and system complexity.

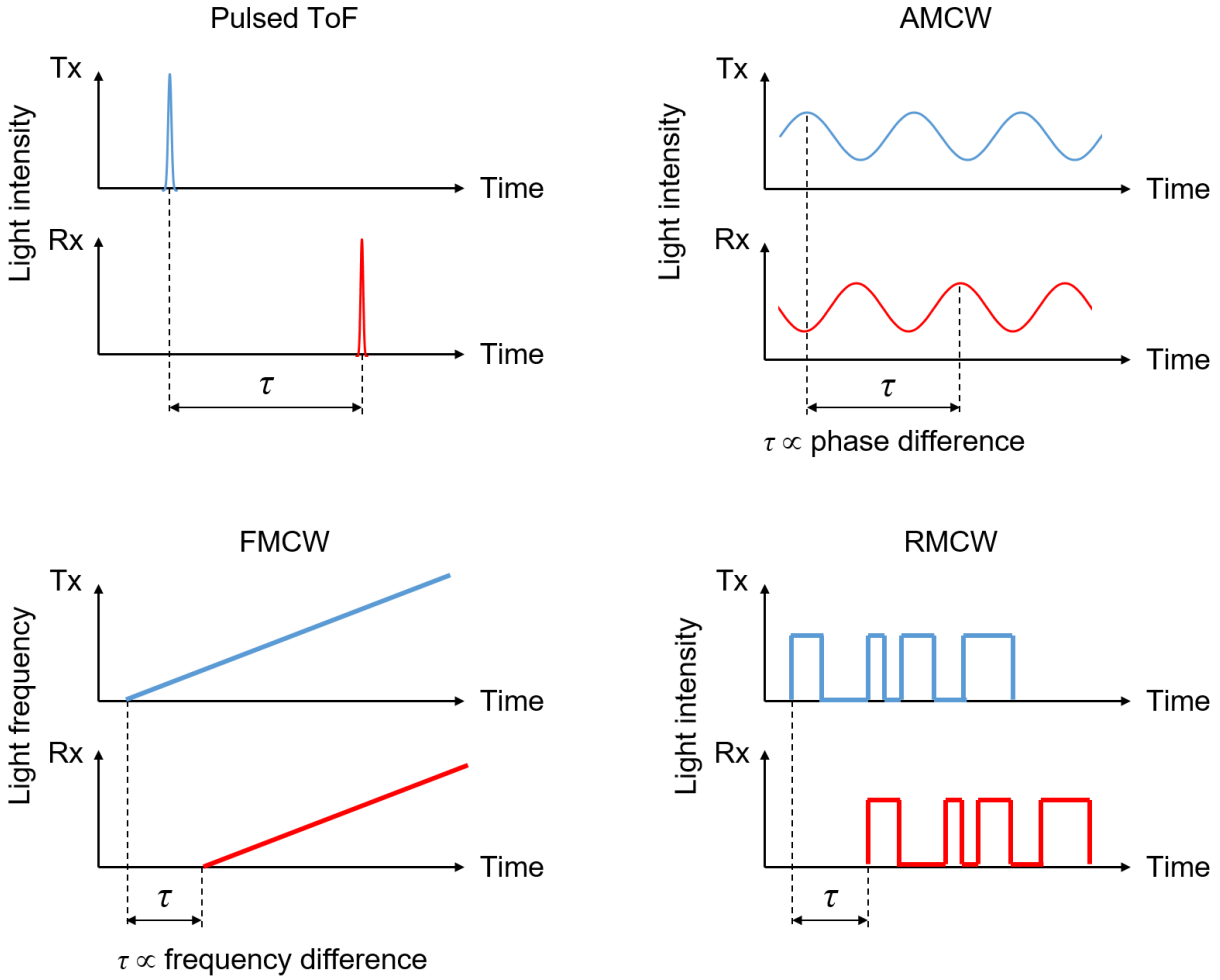

Figure 1-4. LiDAR ranging principles.

A frequency-modulated continuous-wave (FMCW) LiDAR transmits a light wave that is frequency modulated, typically in a linear or triangular wave fashion. The received light and transmitted light have an optical frequency difference that is proportional to the roundtrip time delay. This optical frequency difference can be obtained by mixing the transmitted and received light at the photodetector to generate an RF beat signal. The beat frequency equals the optical frequency difference and can be extracted by digital signal processing methods such as a Fast Fourier Transform (FFT) [14]. The coherent detection of mixing two light signals at the photodetector offers many unique advantages and challenges to FMCW LiDAR, such as the optical gain, the interference immunity, and the laser coherence requirements. These topics will be discussed in Chapter 2 of this dissertation.

A random-modulated continuous-wave (RMCW) LiDAR transmits a light wave that is intensity-modulated by a pseudo-random pattern [15]. The roundtrip time, i.e. the time delay of the received light signal versus the transmitted one, can be extracted by a cross-correlation process, similar to the RF ranging method used in the global positioning system (GPS). The received light can be directly detected, or mixed with the transmitted light for coherent detection. The unique pseudo-random modulation pattern makes the system immune to interference from other LiDAR units and ambient light.

1.3 Optical beam scanners

1.3.1 Mechanical beam scanners

The optical beam scanner is an important component for scanning LiDAR systems as well as many other applications such as free-space optical communication, augmented reality and virtual reality (AR/VR) display, and ion probing in quantum computing systems. Reflection by a mirror is the most common way to change the direction of an optical beam without affecting its other properties, therefore the conventional way to scan the optical beam is to rotate a mirror with mechanical actuators [16]. Spinning a flat mirror or a polygon mirror by a motor can achieve a 360° FoV beam steering at tens of revolutions per second or a smaller FoV at a higher rate. Rotating a mirror by a galvanometer system is another common approach.

For LiDAR systems with 360° spinning mirror optical heads, the other dimension of the 2D FoV is usually composed of an array of transmitters and receivers in parallel without active beam steering. For polygon mirror and galvanometer mirror beam scanners, 2D beam steering can be realized by sequentially reflecting the beam on two rotating mirrors with different rotation axes. A schematic of a 2D galvanometer mirror system (Thorlabs GVS102) is shown in Figure 1-5. In this two-mirror configuration, the second mirror needs to have a size much larger than the beam diameter to capture the scanning beam from the first mirror due to the gap between the two mirrors, which increases the weight of the second mirror and reduces its speed.

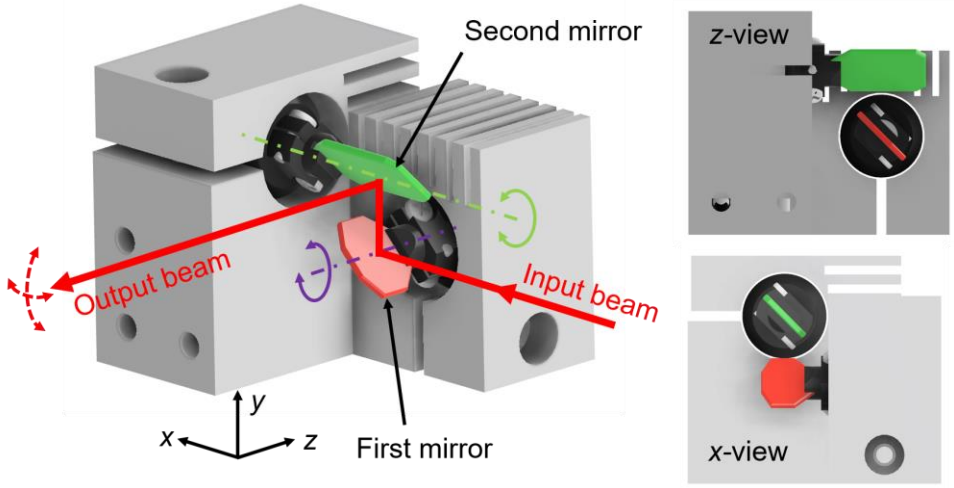

Figure 1-5. Schematic of a 2D galvanometer beam scanner.

Reproduced based on the 3D model from [17].

Mechanical beam scanners employ mature technologies and are widely used in commercial LiDAR products. However, the mechanical actuators tend to be bulky and slow. In addition, their reliability is often questionable under the mechanical vibration and shock of a driving vehicle. Miniaturizing the mirror and the mechanical structure using MEMS technology helps reduce the mirror mass, increase the scanning speed, and increase the intrinsic frequency so the system is less vulnerable to external vibrations [18].

MEMS scanning mirror is composed of a flat mirror located on a 2D gimbal suspension with 2-axis actuators (typically electromagnetic actuators). To achieve a 10 kHz level scanning speed, one of the 2 axes, called the fast axis, is actuated in the resonant mode, where the mirror is scanned at the resonant frequency of the structure. The other axis is actuated in the linear mode. Thanks to the development of MEMS technology, MEMS scanning mirrors have become a mature technology and have been used in commercial LiDAR products. Due to the resonant-mode actuation, the scanning pattern and speed are fixed, and there is a tradeoff between the mirror size and the scanning speed. While a small mirror size increases the structure resonant frequency thus increases the speed, it also reduces the optical aperture and degrades the far-field beam divergence.

1.3.2 Integrated beam scanners

Integrated optical beam scanner without the rotating mirror architecture is the key to realize chip-scale compact LiDAR sensors and is under intensive research and development. Several architectures have been shown promising, including the optical phased array (OPA) and the focal plane switch array (FPSA). OPA and FPSA beam scanners will be discussed in detail in Chapters 3 and 4 of this dissertation respectively.

Another commonly used integrated beam steering approach is dispersive scanning [19]. By tuning the wavelength of an optical beam passing through a dispersive element such as a grating, the direction of the diffracted beam can be steered. Dispersive scanning can alone achieve a 2D FoV by dispersive elements in two directions, or it can also be combined with the OPA or FPSA technology for scanning along one axis in the FoV. It usually requires a large wavelength tuning range to achieve a large FoV and introduces extra complexity of wavelength tuning and control. However, dispersive scanning can be especially applicable if a frequency-tunable or broad-band laser source is used, such as the frequency-modulated laser in an FMCW LiDAR or an optical frequency comb.

1.4 MEMS and silicon photonics technologies

Two important technologies enable the work in this dissertation, namely the MEMS technology and silicon photonics technology. Both of them miniaturize conventionally bulky structures onto integrated platforms, inspired by the microfabrication technologies developed in the semiconductor integrated circuits industry.

MEMS technology enables the fabrication of micrometer to nanometer scale mechanical structures driven by electrical signals [20]. MEMS devices are typically made on silicon wafers, as well as other materials like polymers and metals. Miniaturized mechanical structures offer low mass, high resonant frequency, small thermal constant, low power consumption, and low cost. In addition, the small gaps between structures significantly enhance the electrostatic force, which is

the most common actuation mechanism for MEMS devices. The motions of mechanical structures can be applied for a wide range of applications such as timing (MEMS oscillators), sensing (MEMS accelerometers, gyroscopes, microphone, and pressure sensor), actuating (MEMS speakers, ultrasonic transducers, scanning mirrors, and micro-robots), and switching (MEMS optical switches, digital micromirror devices).

Silicon photonics is the study of optic and photonic systems on silicon platforms [21]. Light is typically confined and propagating in silicon or silicon nitride waveguides with oxide or air claddings, and manipulated by a variety of components like couplers, splitters, gratings, phase shifters, and modulators. Light generation and detection can also be integrated on silicon photonics devices with materials like silicon, germanium, and III-V semiconductor materials. With silicon photonics technologies, conventional bulky optical systems can be integrated on silicon chips and mass fabricated by silicon microfabrication techniques, significantly reducing the footprint, cost, and power consumption of optical systems.

The implementation of MEMS technology on silicon photonics makes the photonic system tunable and reconfigurable, which is a crucial and highly desired feature for many optical manipulations such as laser frequency tuning, optical path length tuning, phase shifting, light path switching, and beam steering, and will be one of the most promising development directions for many reconfigurable photonic devices.

1.5 Structure of the dissertation

This dissertation summarizes our work towards a high-performance FMCW LiDAR system with integrated optical beam scanners.

The challenges on the laser chirp linearity and phase noise requirements for FMCW LiDAR, as well as the proposed laser chirp linearization and phase noise compensation methods, are discussed in Chapter 2.

Two integrated beam scanner architectures, i.e. OPA and FPSA, and the design, fabrication, and characterization of several devices are introduced and demonstrated in Chapters 3 and 4 respectively. Chapter 4 will also introduce the implementation of an FPSA beam scanner on the FMCW LiDAR system for 3D imaging.

Chapter 5 provides a summary of the work in this dissertation and discusses some future directions of research and development.

2 Frequency-modulated continuous-wave (FMCW) LiDAR

2.1 FMCW LiDAR principle

2.1.1 Ranging of a stationary object

An FMCW LiDAR measures the distance d to a stationary target by proportionally converting the roundtrip light travel time τ to an RF beat frequency f_b.

The principle of FMCW LiDAR ranging of a stationary target is shown in Figure 2-1. The laser is linearly frequency modulated in a triangular wave fashion at a chirp rate γ. The laser output is split into a reference path as the local oscillator, and a probe path to the object. The two paths then combine at the photodetector, and their corresponding optical frequencies are shown in the figure by the blue and red curves. Due to the roundtrip time delay $\tau = 2d/c$, the optical frequencies of the reference and the probe paths have a difference of $f_b = \gamma\tau = 2\gamma d/c$. As the two paths interfere on the photodetector, an electrical beat signal at the optical frequency difference f_b is generated and the beat frequency can be extracted by performing a Fourier Transform (FT) on the beat signal. The target distance is then

$$d = cf_b/2\gamma. \tag{2-1}$$

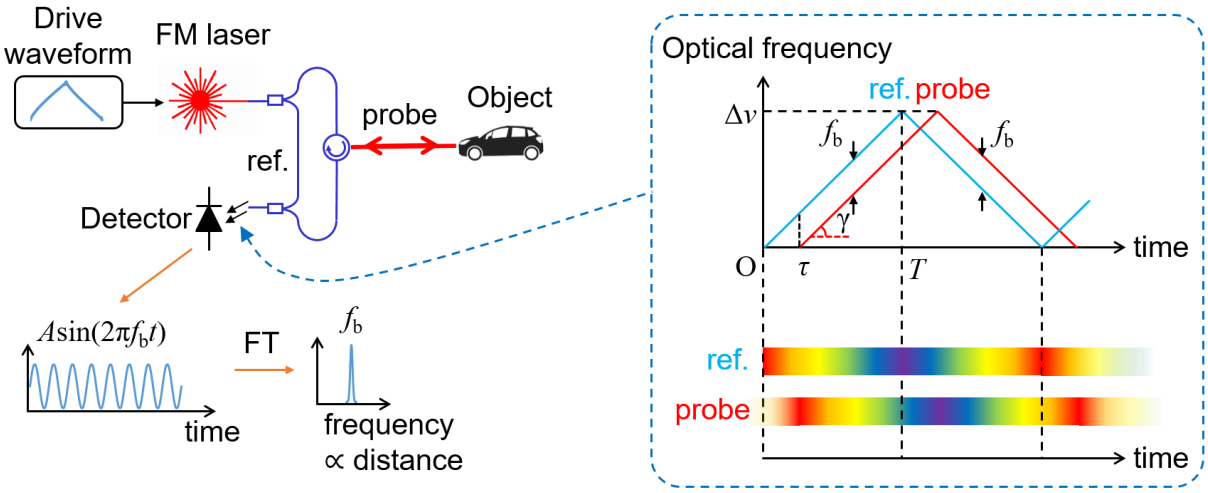

Figure 2-1. Schematic of FMCW LiDAR.

The amplitude of the photocurrent beat signal I is proportional to the square root of the product of the optical power in the reference path P_{ref} and the probe path P_{probe}, i.e.

$$I = R\sqrt{P_{ref}P_{probe}}, \tag{2-2}$$

where R is the responsivity of the photodiode. A balanced detection scheme is often employed to cancel out the DC component in the photocurrent.

For a laser chirp duration T, under the assumption $\tau << T$, the frequency resolution of the FT is $1/T$, therefore the distance resolution is

$$\delta d = c/2\gamma T = c/2\Delta\nu, \tag{2-3}$$

where Δv is the total laser frequency excursion, i.e. the frequency modulation bandwidth. Although Equation (2-3) is derived from the Fourier Transform, the inverse proportional relationship between the distance resolution and the bandwidth of the system is generally valid for radar and LiDAR systems with different ranging principles, which is typically referred to as the bandwidth-limited resolution. Some common distance resolutions and the corresponding laser frequency excursions and wavelength excursions (for a 1550 nm central wavelength) are listed in Table 2-1.

Table 2-1. FMCW ranging resolutions versus laser frequency and wavelength excursions.

Resolution	Frequency excursion (GHz)	Wavelength excursion (nm)
1 m	0.15	1.2×10^{-3}
10 cm	1.5	0.012
1 cm	15	0.12
1 mm	150	1.2
0.1 mm	1,500	12

2.1.2 Ranging and velocimetry of a moving object

The distance and velocity of a moving object can be measured at the same time by the FMCW LiDAR with the information from the up-chirp and down-chirp. For a moving target approaching the LiDAR sensor with a relative velocity that has a component V along the optical beam direction, the returned light from the object will have a frequency shift $f_D = 2V/\lambda$ due to the Doppler effect, where λ is the laser wavelength. The frequency of the reference path will not be affected. Therefore the beat frequencies in the frequency up-chirp and down-chirp are different, shown in Figure 2-2. The beat frequencies are

$$f_{b,up} = 2\gamma d/c - 2V/\lambda, \tag{2-4}$$

$$f_{b,down} = 2\gamma d/c + 2V/\lambda. \tag{2-5}$$

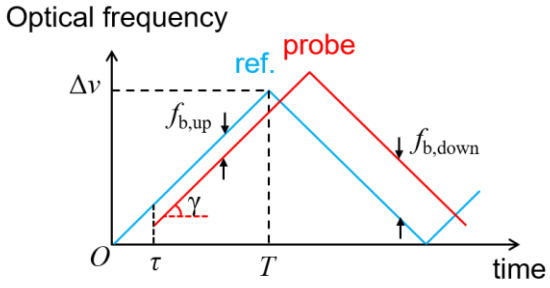

Figure 2-2. Principle of FMCW LiDAR velocimetry.

From Equations (2-4) and (2-5), the target distance and velocity can be solved, i.e.

$$d = c(f_{b,up} + f_{b,down})/4\gamma, \tag{2-6}$$

$$V = \lambda(f_{b,down} - f_{b,up})/4. \tag{2-7}$$

Note that in this derivation both beat frequencies are assumed to be positive. In case the object velocity has a large absolute value, one of the beat frequencies could become negative. With a regular photodetector that cannot detect a negative frequency, this may cause ambiguity in solving the object distance and velocity. With an in-phase and quadrature detector, the negative frequency can be distinguished from the positive frequency and the unambiguous range of distance and velocity detection can be expanded.

Similar to the derivation of Equation (2-3), the velocity detection resolution is

$$\delta V = \lambda/2T. \tag{2-8}$$

2.1.3 Advantages and laser requirements

In an FMCW LiDAR, the beat signal is generated by mixing the reference and the reflected light at the photodetector, which is the coherent detection scheme and offers many unique advantages.

(1) According to Equation (2-2) the amplitude of the beat signal is proportional to the square root of the optical power of both the reference light and the probe light. Although the probe light, i.e. the returned signal from the object, may have very low optical power, it can be optically amplified by the reference light. In addition, FMCW LiDAR outputs continuous light instead of pulsed light. Therefore, it requires lower peak optical power compared with the pulsed ToF LiDAR, which makes it more eye-safe and compatible with silicon photonics integration.

(2) The coherent detection scheme also implies that the ambient light and light from other LiDAR units cannot interfere with the reference light so they will not generate false objects, therefore FMCW LiDAR is intrinsically immune to external interference.

(3) The beat frequency is typically on the order of 10 to 1000 MHz, requiring lower electronic bandwidth.

(4) As discussed in section 2.1.2, the Doppler frequency shift of a moving object will directly change the beat frequency, enabling the simultaneous detection of distance and velocity.

The coherent detection scheme also introduces special requirements on the lasers.

(1) As shown in Equation (2-3) and Table 2-1, a high distance resolution corresponds to a large laser frequency excursion, requiring a large tuning range of an external modulator, or a highly tunable laser for direct modulation.

(2) The analyses in sections 2.1.1 and 2.1.2 all assume a linear laser chirp. For a laser under direct modulation, a linear frequency chirp is not straightforward to achieve due to the nonlinear laser dynamics. We have shown in [22] that a nonlinear frequency chirp will degrade the distance resolution. Therefore linearization or post-processing is necessary to ensure that the bandwidth-limited resolution is achieved.

(3) The laser phase noise from intrinsic spontaneous emissions and noise from the external driver will introduce noise in the beat signal, which will degrade the signal-to-noise ratio (SNR) in the beat signal spectrum after the Fourier Transform. This effect is more significant for a long object distance. To detect a long distance object, the laser phase noise needs to be suppressed or compensated for.

Our proposed methods to linearize the laser chirp and compensate for the laser phase noise will be discussed in sections 2.2 and 2.3.

2.1.4 Related technologies: SSOCT and OFDR

The ranging principle of FMCW LiDAR, i.e. converting the roundtrip travel time of an electromagnetic wave to a frequency difference, has an origin in the radar technology, namely FMCW radar. It has been borrowed and implemented in several optical sensing technologies. It is worth noting that besides the FMCW LiDAR, the swept-source optical coherence tomography (SSOCT) and optical frequency domain reflectometry (OFDR) are two common applications. Despite having different terminologies and specifications, these technologies share the same principle and many common methodologies.

Optical coherence tomography (OCT) is the 3D sensing technology to capture 3D images of the optical scattering media such as biological tissues [23]. It is an important medical imaging method for skin, blood vessels, and retina. OCT typically requires micrometer level distance resolution in several centimeters range. Similar to LiDAR, OCT also has many ranging principles, and SSOCT is one of them. A swept laser source with a large tuning range is necessary to achieve the high resolution requirement. The laser tuning and control techniques developed in the field of SSOCT are valuable resources for the FMCW LiDAR.

While LiDAR can also be classified into the general optical reflectometry category, OFDR usually refers to the technology used to analyze the optical path characteristics of optical fibers and components [24]. Light is sent into the fiber or component, and the relation between measured reflections as a function of distance reveals component characteristics such as scattering, back reflection, broken point, strain, and temperature change. Some OFDR systems measure optical fiber of tens of kilometers long, therefore require lasers with ultra-low phase noise or narrow linewidth. The linewidth suppression or phase noise compensation techniques developed for OFDR systems can also be applied for the FMCW LiDAR.

2.2 Laser chirp linearization by iterative learning pre-distortion

Conventionally the laser chirp in an FMCW LiDAR can be linearized by feedback control using an optical phase-locked loop [25], at the cost of the complex design of a high-bandwidth control circuit. The nonlinearity effect can also be partly removed by resampling the beat signal in post-processing [26], but it involves heavy computation and is not compatible with velocity detection.

We proposed a laser chirp linearization method by iterative learning pre-distortion of the laser drive waveform, and the schematic is shown in Figure 2-3. The detailed principle, procedure, and experimental verification have been described in [22] and [27]. As a summary, the procedure starts with a triangular laser drive waveform, and iteratively updates this drive waveform according to the difference between the actual laser chirp measured by a monitor Mach-Zehnder interferometer (MZI) and the desired linear chirp. At the end of this iterative learning procedure, a pre-distorted nonlinear laser drive signal that leads to a linear laser chirp can be obtained and then used for the following FMCW LiDAR measurements.

Compared with other laser chirp linearization methods, the iterative learning pre-distortion method eliminates the complicated feedback control circuit and the heavy post-processing. It provides a laser chirp with good linearity achieving bandwidth-limited distance resolution in FMCW LiDAR. Compared with other digital pre-distortion methods that require a model for the laser, this method does not need a laser dynamics model, thus can be applied to any type of lasers. The setup is simple and the procedure converges quickly within a small number of iterations.

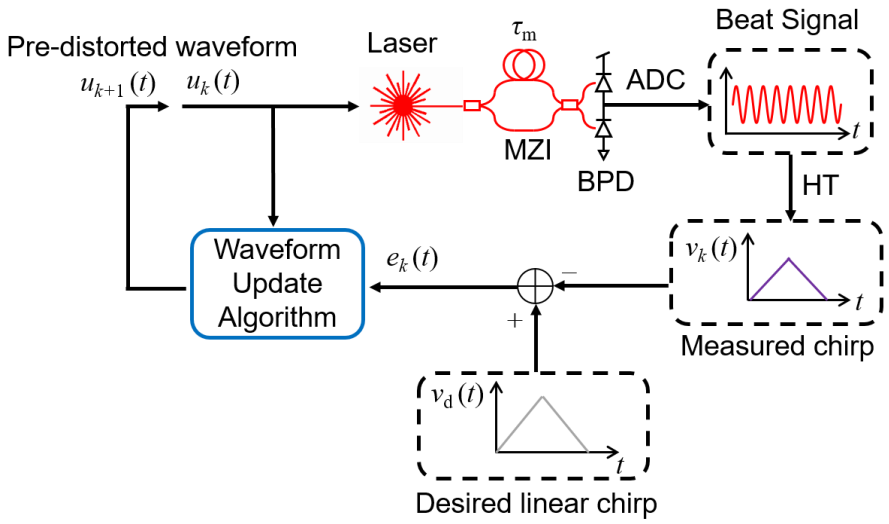

Figure 2-3. Schematic of laser chirp linearization by iterative learning pre-distortion.

MZI: Mach-Zehnder interferometer; BPD: balanced photodetectors; ADC: analog-to-digital converter; HT: Hilbert Transform.

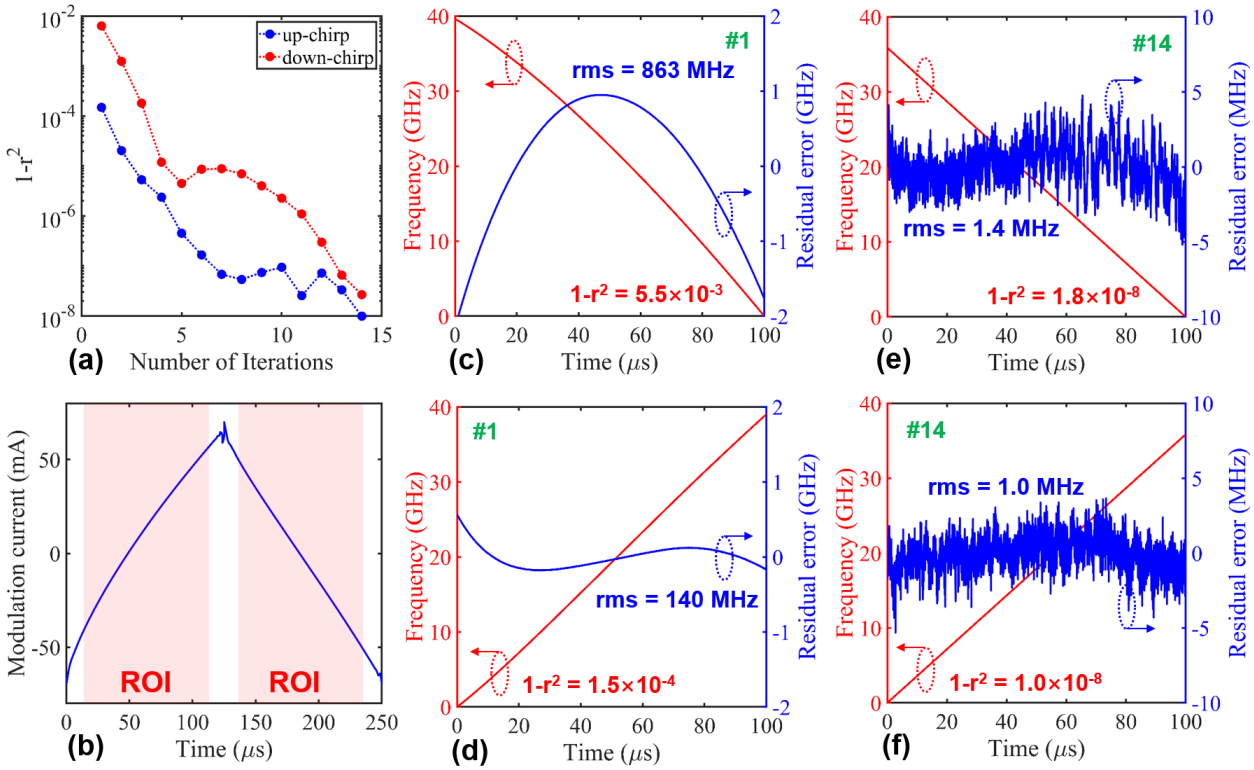

Figure 2-4. Iterative learning pre-distortion linearization of a commercial DFB laser.

(a) Laser chirp nonlinearity versus iterations. (b) Pre-distorted laser drive waveform in the 14th iteration. (c), (d) Laser chirps and residual nonlinearities in the 1st iteration. (e), (f) Laser chirps and residual nonlinearities in the 14th iteration.

The experimental results of a commercial distributed feedback (DFB) laser linearized by the iterative learning pre-distortion method are shown in Figure 2-4. The chirp root-mean-square (RMS) nonlinearity in the region of interest (ROI) (the middle 80% of the laser chirps) is reduced by about 140× in the up-chirp and by about 600× in the down-chirp.

The linearized DFB laser is implemented on a fiber-based monostatic FMCW LiDAR system to image a scene at about 3 m distance away from the LiDAR within a 24°×20° FoV. The camera photo and measured 3D point cloud are shown in Figure 2-5. The objects in the scene are captured with high fidelity in the 3D image. The results show that with the proposed iterative learning pre-distortion method, the laser chirp can be linearized so that high FMCW LiDAR ranging resolution can be achieved.

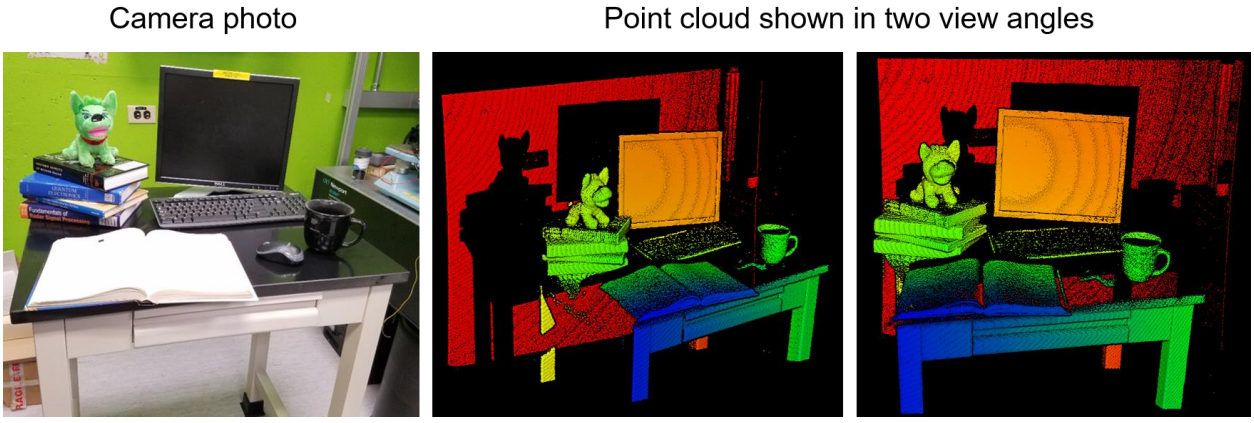

Figure 2-5. 3D imaging by FMCW LiDAR with iterative learning pre-distortion linearization.

2.3 Laser phase noise compensation

Although lasers are known for their high coherence, the spectrum of a laser is never a perfect delta function. The laser spectrum is broadened by phase noises due to intrinsic spontaneous emissions and external driver noises. Laser phase noises degrade the SNR of FMCW LiDAR beat signals, especially at long distances. Therefore, to detect objects far away from the LiDAR system, we need to deal with the phase noise effects.

The direct solution is to use a laser with a narrow linewidth or to suppress the laser linewidth by some feedback control systems, which can be complex and expensive. Alternatively, the laser phase noise can be extracted from a monitor MZI with a known delay and then compensated for in the measured LiDAR beat signal. We proposed a laser phase noise compensation method in post-processing, and a schematic of the setup is shown in Figure 2-6. The detailed principle, procedure, and experimental verification have been described in [27]. As a summary, the laser phase noise information is extracted from the beat signal of the monitor MZI, and the phase noise effects in the LiDAR MZI beat signal can be computed precisely for an object at a roundtrip distance that is an integer multiplication of the monitor MZI delay. For an object not exactly at those distances, the phase noise effects in the LiDAR MZI beat signal can still be largely compensated for using the information for the closest integer multiplication of the monitor MZI delay. The compensation process involves a multiplication of the phase noise effects expressed in the complex exponential form to the original LiDAR beat signal. This process does not affect the Doppler shift in the beat signal and can compensate for the phase

noise due to the target distance regardless of the target velocity, thus is compatible with velocity detection. An example experimental demonstration with the commercial DFB laser and a 150 m optical path composed of several sections of optical fibers and a free-space path is shown in Figure 2-7. Multiple objects along the path are clearly detected in the FMCW LiDAR beat signal spectrum after phase noise compensation, while the spectrum before phase noise compensation does not have enough SNR to capture the objects at long distances.

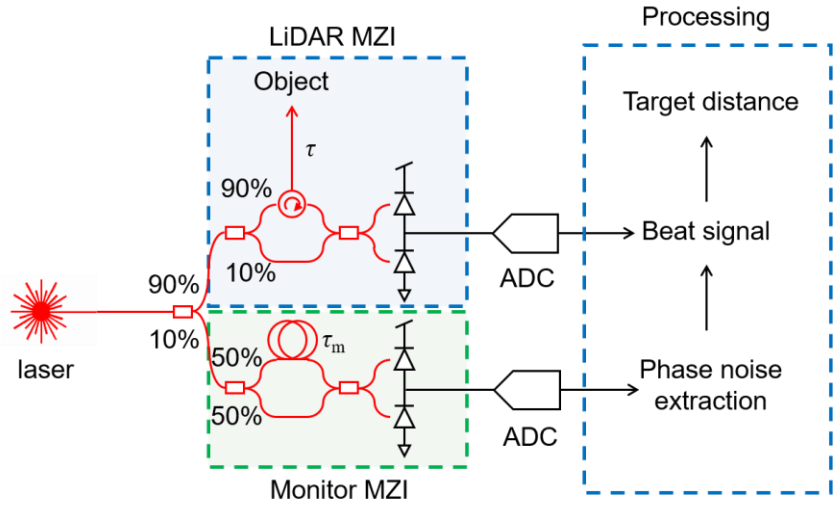

Figure 2-6. Schematic of the laser phase noise compensation method.

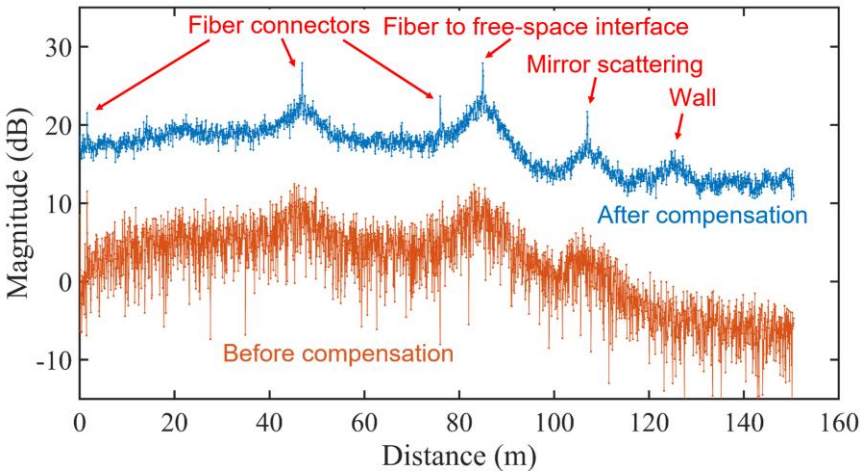

Figure 2-7. Experimental FMCW LiDAR spectrum with laser phase noise compensation.

2.4 FMCW LiDAR signal and noise analyses

2.4.1 Signal and noise components

The link budget is an important factor to be considered when designing a LiDAR system. An SNR at least larger than 1 is necessary to detect an object, and a higher SNR is crucial to ensure the desired probability of detection and false alarm rate. This involves considering the laser

specifications, all sources of optical losses along the path, all sources of noises in detection and processing, and possible interference from ambient light and other light sources.

Assume the laser output power is P_{laser}, and r_{ref} is the power splitting ratio of the reference path as the local oscillator, so the optical power in the reference path is

$$P_{\text{ref}} = r_{\text{ref}} P_{\text{laser}}, \tag{2-9}$$

and the optical power that goes into the probe path is $(1 - r_{\text{ref}})P_{\text{laser}}$. Assume the optical efficiency of the transmitter is η_{tx}, the transmitted optical power, i.e. the output power of the LiDAR, is $P_{\text{tx}} = \eta_{\text{tx}}(1 - r_{\text{ref}})P_{\text{laser}}$.

Assume the object surface is larger than the beam size, the object distance is d, the reflectivity of the object is ρ, the beam incident angle on the object surface is θ, the receiver optical aperture diameter is d_{rx}, and the optical efficiency of the receiver is η_{rx}. For an ideal object with a Lambertian reflectance, ignoring the attenuation of light propagating in the air, the received optical power is [28]

$$\begin{aligned} P_{\text{rx}} &= P_{\text{tx}} \rho \cos(\theta) \frac{d_{\text{rx}}^2}{4d^2} \eta_{\text{rx}} \\ &= (1 - r_{\text{ref}}) \eta_{\text{tx}} \eta_{\text{rx}} \rho \cos(\theta) \frac{d_{\text{rx}}^2}{4d^2} P_{\text{laser}}. \end{aligned} \tag{2-10}$$

According to Equation (2-2), the amplitude of the AC beat signal in the photocurrent is

$$I_{\text{AC}} = R\sqrt{P_{\text{ref}} P_{\text{rx}}}, \tag{2-11}$$

where R is the responsivity of the photodiode, and the DC component of the photocurrent is

$$I_{\text{DC}} = R(P_{\text{ref}} + P_{\text{rx}}). \tag{2-12}$$

Next, we will express all the signal and noise components in terms of their single-sided amplitude spectral density (ASD) in the voltage beat signal recorded by the ADC. The strength of the signal and noise components in the frequency domain is commonly calculated in terms of the power spectral density (PSD) in the unit V^2/Hz. The square root of PSD is ASD in the unit $V/Hz^{-1/2}$, which is linear to the voltage. In an FMCW LiDAR, the data is usually processed by directly performing an FFT on the beat signal in terms of voltage recorded by the ADC. The FFT result of the beat signal is still in unit V, and it is related to the ASD by the following equation [29],

$$\text{ASD} = \sqrt{\text{PSD}} = \sqrt{\frac{2\left|\text{FFT}\{\text{beat signal in V}\}\right|^2}{N f_{\text{s}}}}, \tag{2-13}$$

where N is the total number of samples in the signal, and f_{s} is the ADC sampling frequency. Equation (2-13) shows that the ASD and FFT of the beat signal are proportional by a constant factor, therefore the signal and noise analyses using ASD will match the result of the common FFT processing, i.e. the SNR computed from ASD is the same as the SNR shown in the FFT spectrum of the beat signal. To avoid confusion in the definition of SNR, it is worth noting that the SNR in terms of power is the square of the SNR in terms of amplitude computed from ASD, i.e. they are different by a factor of 2 in the dB scale.

The ASD of the beat signal at the beat frequency f_b, i.e. the spectral peak of the object, is

$$\sigma_{\text{signal}}\left(f_b\right)=G_{\text{TIA}}\sqrt{\frac{I_{\text{AC}}^2}{2}T\exp\left(-\frac{2\tau}{\tau_c}\right)}, \tag{2-14}$$

where G_{TIA} is the trans-impedance amplifier (TIA) gain, T is the laser chirp duration, τ is the roundtrip time delay of the object, and τ_c is the coherence time of the laser [30]. This shows that the signal peak is higher when the target distance is shorter and the laser coherence time is longer.

The signal peak is accompanied by a noise pedestal due to the laser phase noise. Assume $\tau << T$, the ASD of the top of the phase noise pedestal at the beat frequency f_b is [30]

$$\sigma_{\text{pedestal}}\left(f_b\right)=G_{\text{TIA}}\sqrt{\frac{I_{\text{AC}}^2}{2}\tau_c\left[1-\left(1+\frac{2\tau}{\tau_c}\right)\exp\left(-\frac{2\tau}{\tau_c}\right)\right]}. \tag{2-15}$$

The ASDs of the shot noise, laser relative intensity noise (RIN), thermal noise, and ADC digitization noise are

$$\sigma_{\text{shot}}\left(f\right)=G_{\text{TIA}}\sqrt{2eI_{\text{DC}}}, \tag{2-16}$$

$$\sigma_{\text{RIN}}\left(f\right)=G_{\text{TIA}}r_{\text{CMRR}}\sqrt{I_{\text{DC}}^2\cdot RIN}, \tag{2-17}$$

$$\sigma_{\text{thermal}}\left(f\right)=\sqrt{4k_{\text{B}}T_{\text{temp}}G_{\text{TIA}}}, \tag{2-18}$$

$$\sigma_{\text{ADC}}\left(f\right)=\sqrt{\left(\frac{V_{\text{ADC}}}{2^N}\right)^2\Big/B_{\text{ADC}}}, \tag{2-19}$$

where e is the elementary charge, r_{CMRR} is the common-mode rejection ratio (CMRR) of the balanced detectors, k_{B} is the Boltzmann constant, T_{temp} is the temperature, V_{ADC} is the ADC voltage range, N is the ADC bit resolution, and B_{ADC} is the ADC bandwidth.

The ambient light such as the sunlight and lamplight received by the LiDAR receiver will not generate a single-frequency beat signal since it is not coherent with the reference light. However, because the ambient light is typically broadband, the mixing of itself and with the reference light can still generate noises within the ADC detection bandwidth. The ASDs of the ambient-ambient and ambient-reference noises are [31]

$$\sigma_{\text{amb-amb}}=G_{TIA}\sqrt{4R^2\left(S_{\text{amb}}^2B_{\text{optical}}\right)}, \tag{2-20}$$

$$\sigma_{\text{amb-ref}}=G_{TIA}\sqrt{4R^2\left(P_{\text{ref}}S_{\text{amb}}\right)}, \tag{2-21}$$

where S_{amb} is the PSD of the received ambient light in the unit W/Hz, B_{optical} is the optical bandwidth of the receiver.

2.4.2 Signal and noise numerical simulations

To illustrate the variations of the signal and noise components as functions of object distance and laser power, example numerical values are plugged into the equations in the previous section to calculate the ASD of each signal and noise component. The numerical values used in the simulations are summarized in Table 2-2.

Table 2-2. Numerical values for the signal and noise simulations.

Quantity	Symbol	Value	Unit
Laser power	P_{laser}	50	mW
Laser central wavelength	λ	1550	nm
Laser frequency excursion	$\Delta\nu$	10	GHz
Laser chirp time	T	80	μs
Laser coherence time	τ_c	0.64	μs
Laser RIN	RIN	-150	dBc/Hz
Power split ratio to reference path	r_{ref}	0.1	–
Transmitting optical efficiency	η_{tx}	70%	–
Receiving optical efficiency	η_{rx}	50%	–
Receiver aperture diameter	d_{rx}	10	mm
Object distance	d	50	m
Object reflectivity	ρ	10%	–
Beam incident angle on object	θ	0	degree
Photodiode responsivity	R	0.95	A/W
Balanced detection CMRR	r_{CMRR}	-25	dB
TIA gain	G_{TIA}	1.6×10^{4}	V/A
ADC voltage range	V_{ADC}	1	V
ADC bit resolution	N	8	bits
ADC bandwidth	B_{ADC}	500	MHz
Temperature	T_{temp}	300	K
Received ambient light PSD	S_{amb}	1.57×10^{-20}	W/Hz
Receiver optical bandwidth	B_{optical}	1	nm

The signal and noise components are computed as a function of object distance when the laser power is fixed at 50 mW, shown in Figure 2-8. The signal strength and the laser phase noise pedestal are dependent on the object distance, while other noise components are constant as the object distance varies. The dominant noise components are the laser phase noise and shot noise.

At about 220 m object distance, the signal strength becomes lower than the shot noise level and the SNR drops below 1, which sets the detection range of the LiDAR. The signal to phase noise pedestal ratio can be increased with a narrow linewidth laser or the phase noise compensation processing.

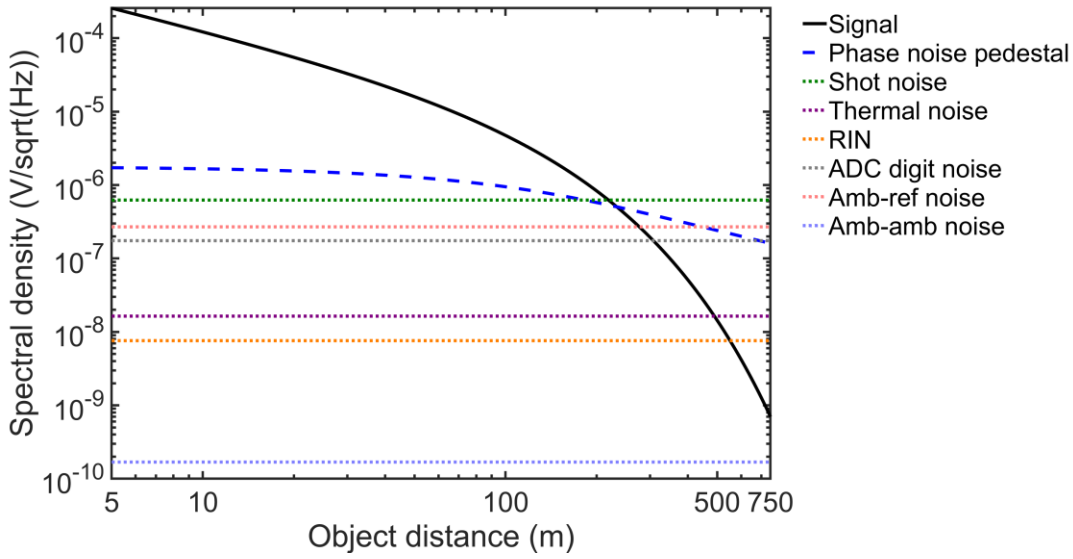

Figure 2-8. Signal and noise simulation results versus object distance.

Figure 2-9 shows the calculated signal and noise components as a function of laser power when the object distance is fixed at 50 m. Different noise components are dominant at different laser power levels. At low laser power, the ADC digitization noise dominates, but it can be simply reduced by using a higher resolution ADC, so effectively the dominant noise component is the shot noise at low laser power. The signal-to-shot noise ratio can be increased by increasing the laser power. At high laser power, the laser phase noise becomes dominant.

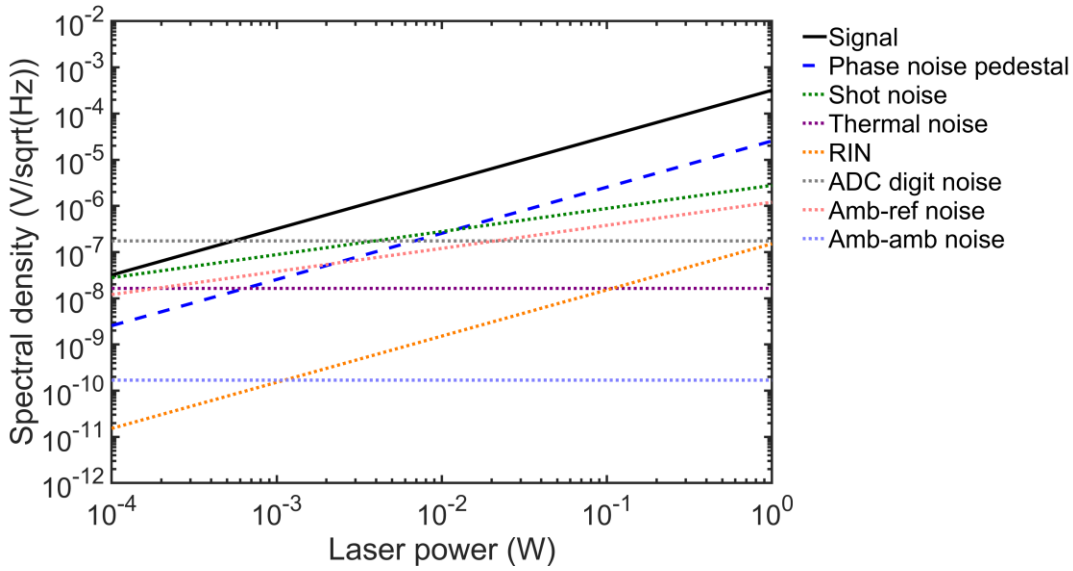

Figure 2-9. Signal and noise simulation results versus laser power.

Besides the object distance and laser power, all the values listed in Table 2-2 will affect the SNR of FMCW LiDAR. For a practical LiDAR sensor, given the requirements on the detection range, resolution, frame rate, and probability of detection, it is important to perform SNR analyses to select proper specifications of key components such as the laser, photodetector, transmitter and receiver optics, and ADC. The procedure outlined in this section can be a reference to compute the strength of signal and noise components.

2.5 Chapter summary

This chapter introduces the principle of FMCW LiDAR ranging and velocimetry, as well as its advantages and requirements on the laser chirp linearity and phase noise. A laser chirp linearization method by iterative learning pre-distortion of the drive waveform and a laser phase noise compensation process are described (more details on these two methods are discussed in [27]). With these two methods, high-performance FMCW LiDAR can be achieved using commercially available semiconductor lasers, a simple optical setup, and fast data processing.

Analyses and numerical simulations of the signal strength and noise components in the spectrum of the FMCW LiDAR beat signal are also covered in this chapter. The SNR consideration is crucial for determining the component specifications in an FMCW LiDAR system, and it provides a guideline for the optical beam scanner design and evaluation in the following chapters.

The work in section 2.3 of this chapter was performed with assistance from Jazz Pouls in signal acquisition and processing [22]. I also would like to thank Margaret Zhang for her assistance in building the LiDAR experimental setup.

3 Grating-based MEMS optical phased array (OPA)

3.1 OPA introduction

3.1.1 OPA principle

OPA is composed of an array of coherent optical antennas with controllable optical amplitudes and phases, shown in Figure 3-1. The principle of OPA can be intuitively understood from the Huygens principle where each antenna acts as a spherical wave source. When all the antennas have an equal optical phase, the spherical waves are synchronized, forming a wave front parallel to the OPA plane. When the antennas have a relative phase difference, the wave front formed by the spherical waves will be tilted. Therefore, by controlling the relative optical phases of the antennas, the output beam can be steered to different directions in the far-field.

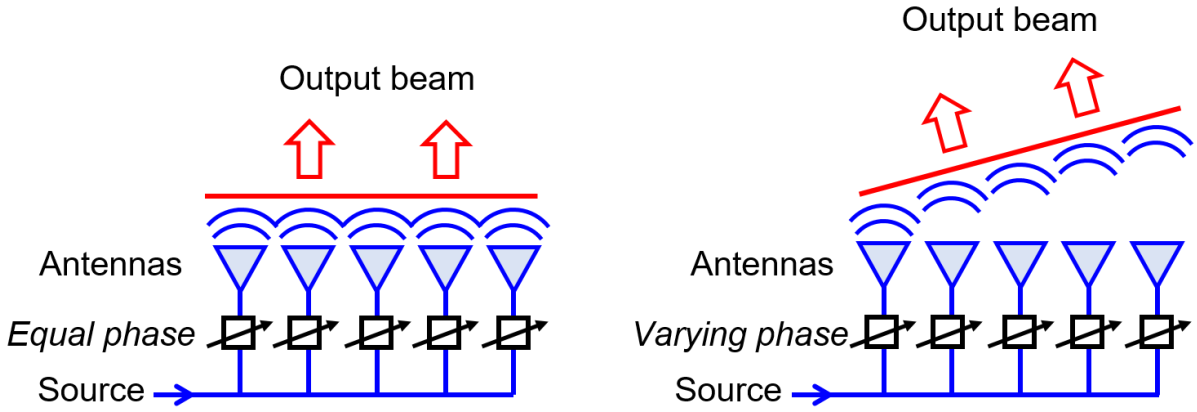

Figure 3-1. Schematic of OPA.

The principle of OPA can be analyzed in a more rigorous way using the scalar diffraction theory, with a setup shown in Figure 3-2. All antennas emitting light together form an optical field distribution $E(x', y', 0)$ on the OPA plane ($z = 0$), where x' and y' are the coordinates on the OPA plane. According to the scalar diffraction theory, the far-field optical field distribution $E(x, y, z)$ on the observation plane at a distance z from the OPA can be described by the Fraunhofer diffraction formula

$$E(x,y,z) = -\frac{ie^{ikz}e^{i\frac{k}{2z}\left(x^2+y^2\right)}}{\lambda z}\iint_L E(x',y',0)e^{-i\frac{k}{z}(xx'+yy')}dx'dy', \tag{3-1}$$

where $k = 2\pi/\lambda$ is the angular wavenumber [32]. The Fraunhofer diffraction is valid for far-field when $z >> L^2/\lambda$ where L is the OPA aperture size.

For convenience in analyzing the OPA beam steering characteristics, Equation (3-1) can be written in terms of the far-field angles

$$E(\theta_x,\theta_y) = -\frac{ie^{ikz}e^{i\frac{kz}{2}\left(\sin(\theta_x)^2+\sin(\theta_y)^2\right)}}{\lambda z}\iint_L E(x',y')e^{-ik\left(x'\sin(\theta_x)+y'\sin(\theta_y)\right)}dx'dy'. \tag{3-2}$$

For optical beam steering applications, the far-field intensity distribution is of interest in the analyses. The coefficient before the integral in Equation (3-2) is a phase term related to θ_x and θ_y but does not affect the amplitude or intensity distribution of $E(\theta_x, \theta_y)$, therefore it can be combined as a constant coefficient C and the equation can be simplified to

$$E\left(\theta_x,\theta_y\right)=C\iint_L E\left(x',y'\right)e^{-i2\pi\left(x'\frac{\sin\left(\theta_x\right)}{\lambda}+y'\frac{\sin\left(\theta_y\right)}{\lambda}\right)}dx'dy'. \tag{3-3}$$

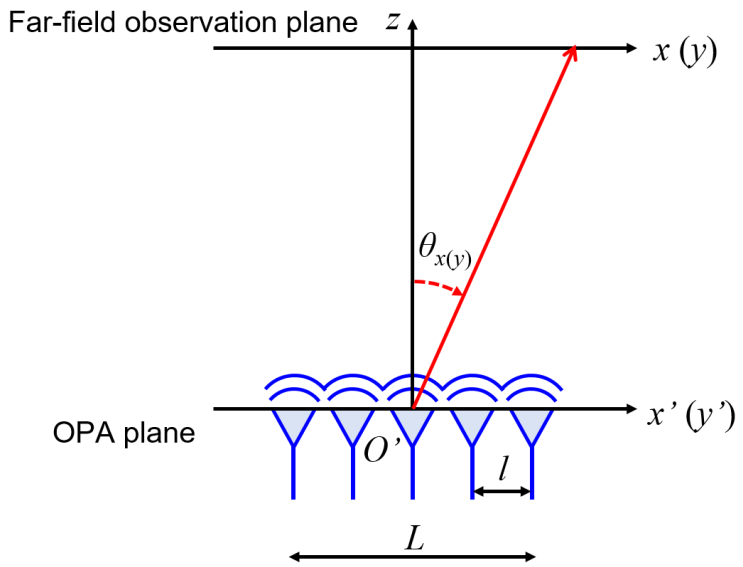

Figure 3-2. OPA analyses by scalar diffraction theory.

The integral in Equation (3-3) is a 2D Fourier Transform integral, and the Fourier Transform pair can be expressed as

$$E_{\text{far-field}}\left(\frac{\sin\left(\theta_x\right)}{\lambda},\frac{\sin\left(\theta_y\right)}{\lambda}\right)\xleftarrow{FT}E_{\text{OPA}}\left(x',y'\right). \tag{3-4}$$

The terms $\sin(\theta_x)/\lambda$ and $\sin(\theta_y)/\lambda$ are often considered as the spatial frequency of the far-field optical field distribution in the x and y directions respectively, so Equation (3-4) represents a Fourier Transform from the spatial coordinate domain to the spatial frequency domain. Therefore, we define the spatial frequencies as the independent variables for the far-field distribution,

$$\xi_x=\frac{\sin\left(\theta_x\right)}{\lambda},\xi_y=\frac{\sin\left(\theta_y\right)}{\lambda}, \tag{3-5}$$

and by the definition $-1/\lambda\le\xi_x,\xi_y\le1/\lambda$.

Considering the independence of Fourier Transform in the x and y directions, without loss of generality we will only look into one dimension of the OPA to simplify the following analyses.

For a 1D OPA with a uniform pitch l in the x direction, the field distribution on the OPA plane can be further split into several components as

$$E_{\text{OPA}}(x') = E_{\text{a}}(x') \otimes \left[\frac{1}{l} \text{comb}\left(\frac{x'}{l} \right) \cdot A(x') e^{i\varphi(x')} \right], \tag{3-6}$$

where $\otimes$ represents the convolution operation. In Equation (3-6), $E_{\text{a}}(x')$ describes the emission optical field of a single antenna. The Dirac comb function term defined as

$$\text{comb}\left(\frac{x'}{l} \right) = l \sum_{n=-\infty}^{\infty} \delta(x' - nl), \tag{3-7}$$

represents an infinite uniformly pitched array with pitch l. $A(x')$ and $\varphi(x')$ are the amplitude and phase distributions throughout the OPA, which are set by controlling the amplitudes and phases of the antennas.

Combining Equations (3-4) and (3-6), the far-field optical field distribution of the 1D uniform-pitch OPA is

$$\begin{aligned} E_{\text{far-field}}(\xi_x) &= C \cdot FT\{E_{\text{a}}(x')\} \cdot \left[FT\left\{ \frac{1}{l} \text{comb}\left(\frac{x'}{l} \right) \right\} \otimes FT\left\{ A(x') e^{i\varphi(x')} \right\} \right] \\ &= C \cdot E_{\text{a,far-field}}(\xi_x) \cdot \left[\text{comb}(l\xi_x) \otimes FT\left\{ A(x') e^{i\varphi(x')} \right\} \right]. \end{aligned} \tag{3-8}$$

To further simplify the expression by examining a common OPA model, assume each antenna is a perfect point source with a uniformly distributed far-field profile, so the $E_{\text{a,far-field}}$ term is a constant. Assume all the antennas have equal and normalized amplitude, so $A(x') = \text{rect}(x'/L)$ is a rectangular window with a width L. To steer the beam to a far-field angle α_x, intuitively we need a phase difference of $2\pi\sin(\alpha_x)/\lambda$ per unit length, i.e. $\varphi(x') = 2\pi\sin(\alpha_x)x'/\lambda$. Plug these terms into Equation (3-8) and drop all constant coefficients, we can get

$$\begin{aligned} E_{\text{far-field}}(\xi_x) &= \text{comb}(l\xi_x) \otimes FT\left\{ \text{rect}\left(\frac{x'}{L} \right) e^{i2\pi \frac{\sin(\alpha_x)}{\lambda} x'} \right\} \\ &= \left[\sum_{n=-\infty}^{\infty} \delta\left(\xi_x - \frac{n}{l} \right) \right] \otimes \text{sinc}(\pi L \xi_x) \otimes \delta\left(\xi_x - \frac{\sin(\alpha_x)}{\lambda} \right) \\ &= \left[\sum_{n=-\infty}^{\infty} \delta\left(\xi_x - \frac{\sin(\alpha_x)}{\lambda} - \frac{n}{l} \right) \right] \otimes \text{sinc}(\pi L \xi_x) \\ &= \sum_{n=-\infty}^{\infty} \text{sinc}\left[\pi L \left(\xi_x - \frac{\sin(\alpha_x)}{\lambda} - \frac{n}{l} \right) \right], \end{aligned} \tag{3-9}$$

where the sinc function is defined as

$$\text{sinc}(x) = \frac{\sin(x)}{x}. \tag{3-10}$$

This analysis is also illustrated in Figure 3-3. The optical field distribution on the OPA plane is composed of (1) a Dirac comb function with a pitch l describing the array of point source antennas with a uniform pitch; (2) a rectangular window with a width L describing the equal amplitude of all the antennas within the array aperture L; (3) a linear optical phase change to steer the beam to a far-field angle α_x.

The resulting far-field amplitude distribution is a convolution of a sinc-shaped beam spot with a shifted Dirac comb function. The sinc function is a result of light diffraction from the rectangular array aperture with uniform antenna amplitudes. The shifted Dirac comb function is a result of the periodic array with a phase slope, and the locations of the comb teeth represent the far-field beam spot angles. According to Equation (3-9), the centers of far-field spots are located at

$$\xi_x = \frac{\sin(\theta_x)}{\lambda} = \frac{\sin(\alpha_x)}{\lambda} - \frac{n}{l}, \quad n = 0, \pm 1, \pm 2, \ldots \tag{3-11}$$

Equation (3-11) is similar to a diffraction grating equation due to the periodic structure of the OPA. When $n = 0$ it gives $\theta_x = \alpha_x$, meaning there is a far-field beam spot at the desired beam steering angle α_x as expected. An aperiodic OPA can help to suppress the aliasing grating lobes by redistributing them more uniformly across different far-field angles.

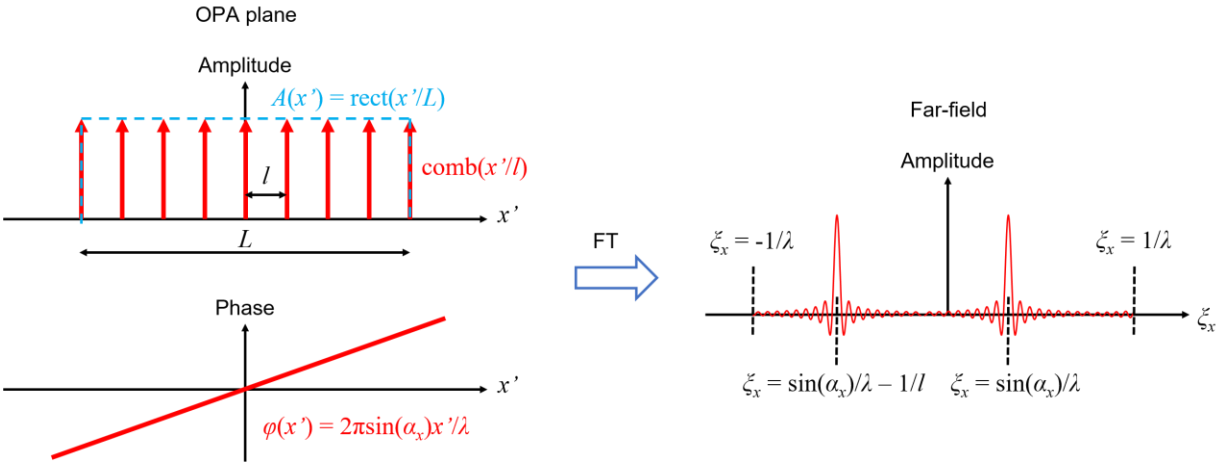

Figure 3-3. Example illustration of the OPA plane and far-field optical field distributions.

3.1.2 OPA parameters

From the analyses in the previous section, we can derive some important parameters for the OPA beam steering.

(1) Beam steering FoV.

From Equation (3-11), a series of beam spots exist in the far-field. The existence of the higher-order spots limits the FoV of beam steering. The largest far-field beam angle without aliasing can be determined by setting the 0^{th} and 1^{st} order spots on the two boundaries of the FoV, i.e.

$$\frac{\sin(-\mathrm{FoV}/2)}{\lambda} = \frac{\sin(\mathrm{FoV}/2)}{\lambda} - \frac{1}{l}, \tag{3-12}$$

therefore the FoV is

$$\text{FoV} = 2\arcsin\left(\frac{\lambda}{2l}\right). \tag{3-13}$$

To achieve a full 180° FoV, we need $l \leq \lambda/2$, i.e. the array pitch needs to be smaller than half the wavelength. On the other hand, when the array pitch is much larger than the wavelength, i.e. when $l >> \lambda$, with the small angle approximation, the FoV can be approximated by λ/l.

(2) Beam spot divergence.

In the case shown in Equation (3-9), the shape of the beam spot is determined by the sinc function $\text{sinc}(\pi L\xi_x)$. The location of the first null point is given by

$$\xi_x = \frac{\sin(\theta_x)}{\lambda} = \frac{1}{L} \quad \Rightarrow \quad \theta_x = \arcsin\left(\frac{\lambda}{L}\right). \tag{3-14}$$

Since the array size L is typically much larger than the wavelength, we can apply the small angle approximation to get

$$\text{Divergence} = \frac{\lambda}{L}, \tag{3-15}$$

which is the diffraction limit of the array aperture.

The above derivation is based on the assumption of a uniform antenna amplitude distribution, and the divergence is characterized as the first null point of the sinc function. Other beam spot shapes and definitions of the divergence (for example full-width half-maximum or half-width half-maximum) may lead to different divergence calculation results, typically involving adding a constant factor in Equation (3-15). Nevertheless, the idea that the far-field beam spot divergence is determined by the diffraction of the OPA aperture is generally valid.

(3) Beam spot profile.

The profile or shape of the far-field beam spot is determined by the Fourier Transform of the antenna amplitude distribution $A(x')$. If all the antennas have an equal emission amplitude, $A(x')$ will be a rectangular function with a width equal to the OPA aperture size. Since the Fourier Transform of a rectangular function is a sinc function, the far-field beam spot will have a sinc amplitude profile or a sinc^2 intensity profile.

For some applications, it may be important to suppress the side lobes of the beam by using a different $A(x')$ such as a Gaussian distribution. Suppressing side lobes is typically accompanied by the tradeoff of increasing the beam divergence of the main lobe.

(4) Beam spot intensity change versus steering angle.

According to Equation (3-8), the far-field profile of a single antenna determines the overall envelope of the far-field optical field profile. For an ideal isotropic antenna like a point source, the far-field profile is uniform, therefore the beam spot intensity does not change as a function of the steering angle α_x.

A practical optical antenna cannot be perfectly isotropic, meaning its far-field profile is not uniform. For example, a silicon photonics grating antenna has approximately a Gaussian profile,

and a MEMS mirror reflecting light has approximately a sinc profile. In these cases, the beam spot intensity is not constant during beam steering.

The analyses above are summarized in Table 3-1.

Table 3-1. Summary of important OPA parameters.

Beam steering parameter	Related OPA parameter	Equation
Beam steering angle α_x	Antenna phase distribution $\varphi(x')$	$\varphi(x') = 2\pi\sin(\alpha_x)x'/\lambda$
Higher-order spots $\theta_x(n)$	Beam steering angle α_x Array pitch l	$\sin\left(\theta_x(n)\right) = \sin\left(\alpha_x\right) - \frac{n\lambda}{l}$ $n = 0, \pm1, \pm2, \ldots$
FoV	Array pitch l	$\mathrm{FoV} = 2\arcsin\left(\frac{\lambda}{2l}\right)$
Divergence	Array size L	$\mathrm{Divergence} = \frac{\lambda}{L}$
Beam spot profile	Antenna amplitude distribution $A(x')$	Beam spot amplitude $\propto$ $\lvert FT\{A(x')\}\rvert$
Beam spot intensity vs α_x	Antenna far-field profile $E_{\text{a,far-field}}\left(\xi_x\right)$	Intensity envelope $\propto$ $\left\lvert E_{\text{a,far-field}}\left(\frac{\sin(\alpha_x)}{\lambda}\right)\right\rvert^2$

3.1.3 Advantages and challenges

OPA generates different far-field patterns by varying the amplitude and phase distributions over the optical antenna array without mechanically rotating a mirror, therefore it is a promising candidate for integrated optical beam scanners with fast speed. While the beam steering can be continuous like that achieved by a rotating mirror, discrete random-access beam angles can also be achieved by controlling the antenna phases, enabling more sophisticated beam steering patterns that enable adaptive LiDAR scanning. Furthermore, besides outputting a collimated single beam, OPA can generate a more complicated far-field beam profile acting as a reconfigurable hologram, which can be used in display applications such as AR/VR.

The OPA architecture also faces some challenges. The simultaneous and precise amplitude and phase control of all the antennas is crucial to generate the correct far-field beam profile. For a 2D OPA, the number of optical antennas can be more than 10^4, which leads to high electrical addressing and control complexity. For integrated OPA, the array needs to be fabricated with high uniformity to ensure all the antennas have the same response to control signals. In addition, as suggested by Equation (3-13), a large beam steering FoV requires the array pitch to be comparable with the optical wavelength that is on the order of μm. The requirements on a small

antenna footprint and a close pack of optical routing and electrical addressing introduce additional challenges for large FoV OPA design and fabrication.

3.1.4 OPA architectures

The OPA principle has been implemented in liquid crystal devices for several decades [33]. By applying an external electrical field, the refractive index of the liquid crystal material can be changed, which can be converted to an optical phase change by passing the light through a liquid crystal with a certain thickness. Liquid crystal OPAs are often called spatial light modulators, which are widely used in holographic data storage or display technologies. Unfortunately, liquid crystal OPA does not have the high response speed required for a LiDAR beam scanner.

Silicon photonics platform offers some high-speed optical phase modulators for light propagating in waveguides, such as thermal-optic or electro-optic phase shifters. With these phase shifters and grating antennas, 1D and 2D OPAs have been achieved on silicon photonics platform [34][35]. However, compact waveguide routing, low crosstalk and optical loss, and low phase shifter power consumption remain challenging for large-scale 2D silicon photonics OPA.

With MEMS structures, the optical phase of the reflected light from a micro-mirror can be shifted by simply moving the micro-mirror in the light direction, and the structure is often called the MEMS piston mirror [36][37]. A piston mirror array actuated by vertical MEMS actuators forms an OPA in the free-space reflection mode. The phase distribution of the reflected beam on the OPA plane can be controlled by the vertical displacements of the micro-mirrors. The piston mirror OPA architecture has high optical efficiency thanks to the free-space mirror reflection. However, half-wavelength mirror displacement typically on the order of μm is required for a full 2π phase shift, which is challenging for vertical MEMS actuators due to the large vertical displacement and the pull-in effect of the electrostatic parallel-plate actuators. Therefore, it is desirable to design an optical phase shifter moving in the plane of the OPA device to achieve a full 2π phase shift with a more practical MEMS actuator design, which will be discussed in the next section.

3.2 Design of grating-based MEMS OPA

3.2.1 Grating phase shifter

Grating is an optical component with a periodic structure that diffracts the transmitting or reflecting light. To analyze the phase shifting of the diffracted beam when moving the grating in-plane, we consider the diffraction grating with a period Λ shown in Figure 3-4. To simplify the derivation, assume a normal incidence, assume the grating to have an infinite length, and ignore the width of grating grooves, therefore the optical field on the grating plane can be modeled as a Dirac comb function

$$E_{\text{grating}}(x) = \sum_{n=-\infty}^{\infty} \delta(x - n\Lambda). \tag{3-16}$$

Similar to the derivations in section 3.1.1, the far-field amplitude profile of the diffracted beams is the Fourier Transform of $E_{\text{grating}}(x)$,

$$E_{\text{far-field}}(\xi) = FT\left\{\sum_{n=-\infty}^{\infty}\delta(x-n\Lambda)\right\} = \sum_{n=-\infty}^{\infty}\delta\left(\xi-\frac{n}{\Lambda}\right), \tag{3-17}$$

where $\xi = \sin(\theta)/\lambda$ is the spatial frequency. The angles of diffraction orders satisfy

$$\xi = \frac{\sin(\theta)}{\lambda} = \frac{n}{\Lambda}, \quad n = 0, \pm 1, \pm 2, ..., \tag{3-18}$$

which is the well-known grating equation.

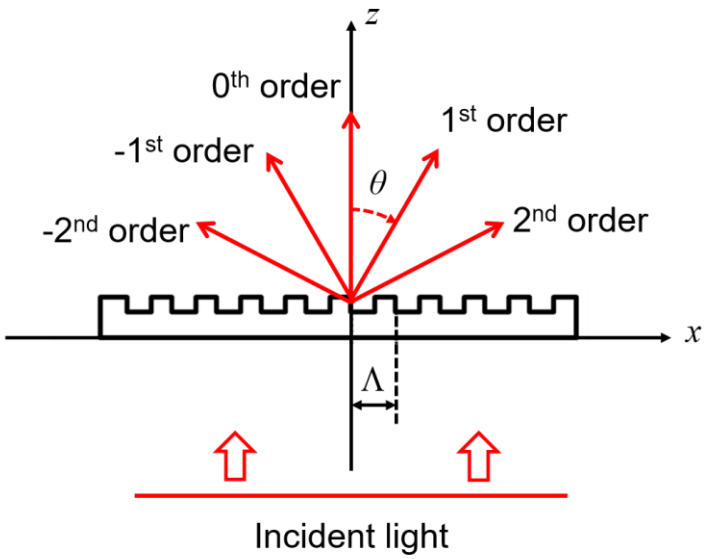

Figure 3-4. Schematic of a diffraction grating.

Now we move the grating to the right side by a displacement Δx. The new optical field on the grating plane is

$$E'_{\text{grating}}(x) = E_{\text{grating}}(x-\Delta x) = \sum_{n=-\infty}^{\infty}\delta(x-\Delta x-n\Lambda). \tag{3-19}$$

According to the Fourier Transform property, a shift in the spatial domain results in an extra phase term in the spatial frequency domain, so the new far-field amplitude profile is

$$\begin{aligned} E'_{\text{far-field}}(\xi) &= e^{-i2\pi\Delta x\xi}E'_{\text{far-field}}(\xi) \\ &= e^{-i2\pi\Delta x\xi}\sum_{n=-\infty}^{\infty}\delta\left(\xi-\frac{n}{\Lambda}\right) \\ &= \sum_{n=-\infty}^{\infty}\delta\left(\xi-\frac{n}{\Lambda}\right)e^{-i2\pi n\frac{\Delta x}{\Lambda}}. \end{aligned} \tag{3-20}$$

Equation (3-20) indicates that a phase shift of $-2\pi n\Delta x/\Lambda$ is imposed on the n-th order diffraction beam. A more detailed derivation can be found in [38].

From the above derivation, we conclude that by moving the grating in the grating plane in a direction perpendicular to the grating grooves, the diffraction beams except the 0th order will have a phase shift that is proportional to the grating displacement and the diffraction order number. For the ±1st order beam, a displacement equal to the grating period Λ is required to achieve a full 2π phase shift.

Practical grating phase shifters do not have an infinite size, therefore the far-field profile is not a perfect comb function. For a grating with a width W under a uniform incident light, the far-field amplitude profile will be a convolution of a sinc function and the comb function, and Equation (3-20) and be rewritten as

$$E'_{\text{far-field}}(\xi) = \sum_{n=-\infty}^{\infty} \text{sinc}\left[\pi W\left(\xi - \frac{n}{\Lambda}\right)\right] e^{-i2\pi n\frac{\Delta x}{\Lambda}}. \tag{3-21}$$

3.2.2 Grating-based OPA with MEMS actuators

By arranging the grating phase shifters discussed in the previous section into a 2D array, a 2D OPA can be realized, and an example of a 4×4-element array is shown in Figure 3-5. Each grating acts as an optical antenna diffracting the incident light. When the gratings are at their original positions, the grating grooves are aligned forming a larger grating, and the directions of the 0th and -1st order diffraction beams can be calculated by Equation (3-18). When some of the gratings are shifted, the optical phase distribution on the OPA plane will be changed. If a linear phase distribution is generated by controlling the displacements of gratings in the array, the direction of the -1st order diffraction beam can be steered.

Note that the direction of the 0th order diffraction beam will not change since there is no phase shift in the 0th order, however by designing the grating period and the incidence angle, the 0th order diffraction can be suppressed, so most of the incident power is directed into the -1st order beam which is steered by the OPA.

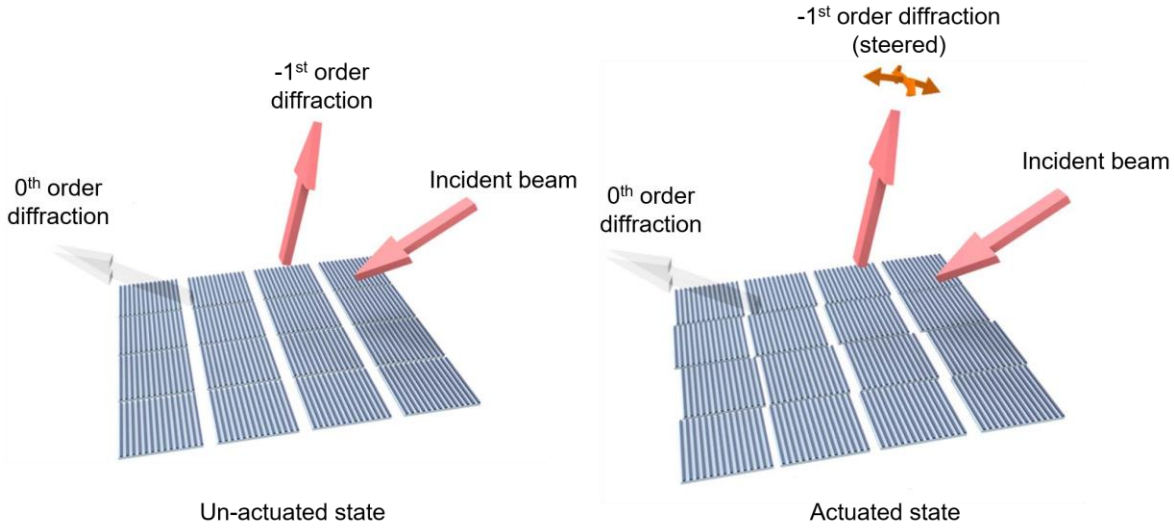

Figure 3-5. Schematic of grating-based 2D passive OPA.

To shift the gratings in an active OPA, electrostatic comb-drive actuators are attached underneath each grating element, so the grating can be moved perpendicular to the grating grooves in both positive and negative directions, shown in Figure 3-6. The structure of a MEMS comb-drive actuator is shown in Figure 3-7. When a voltage V is applied across the two sets of combs, the electrostatic force produced is

$$F = \frac{\varepsilon N t V^2}{2g}, \tag{3-22}$$

where ε is the permittivity, g is the gap between adjacent comb fingers, N is the total number of gaps, t is the thickness of the structure in the direction perpendicular to the plane. If the actuating structure is attached to a spring (typically a folded-beam flexure) with a spring constant k_s, the displacement is

$$\Delta x = \frac{F}{k_s} = \frac{\varepsilon N t}{2 g k_s} V^2. \tag{3-23}$$

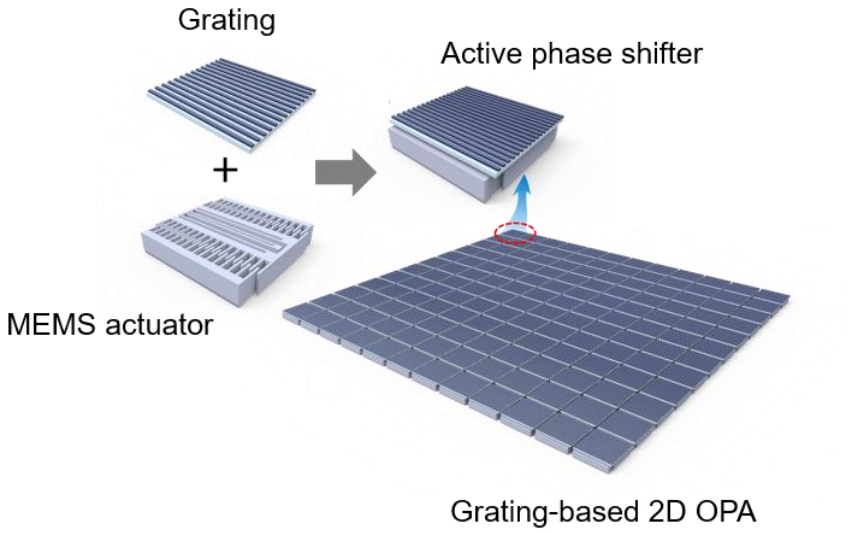

Figure 3-6. Schematic of grating-based 2D active OPA.

Equation (3-23) indicates that the displacement of the comb-drive actuator can be controlled by the voltage applied across the actuator, and it is proportional to the square of the applied voltage.

In our OPA design, each comb drive actuator has 32 gaps with a 300 nm spacing between comb fingers. A 0.21 μN force can be generated at a 10.5 V voltage. For a 2π phase shift, the grating needs to be moved by $\Lambda/2$ = 477.5 nm in both directions, which can be achieved with the 10.5 V voltage.

The grating period chosen for our design is Λ = 955 nm, and the incident angle of the 1550 nm wavelength light is 65°, resulting in a -1st order diffraction at 45° angle. This design ensures that the -1st order is the only diffraction order with high efficiency. The pitch of the grating elements is l_x = 19.1 μm in the direction perpendicular to the grating grooves (defined as the x direction), and l_y = 20 μm in the direction parallel to the grating grooves (defined as the y

direction). Due to the 45° diffraction angle in the x direction, the effective pitch is l_x = 13.5 μm and l_y = 20 μm. According to Equation (3-13), the beam steering FoV is

$$\mathrm{FoV}_x = 2\arcsin\left(\frac{\lambda}{2l_x}\right) = 6.6^\circ, \quad \mathrm{FoV}_y = 2\arcsin\left(\frac{\lambda}{2l_y}\right) = 4.4^\circ. \tag{3-24}$$

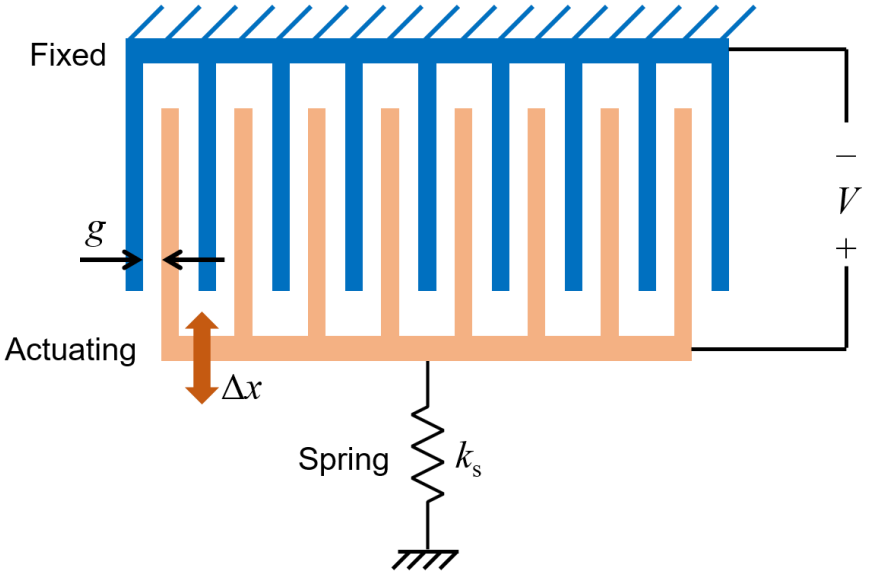

Figure 3-7. MEMS electrostatic comb-drive actuator.

We designed and fabricated an active OPA with 160×160 grating elements, forming an optical aperture of L_x = 3.1 mm and L_y = 3.2 mm. Due to the 45° diffraction angle in the x direction, the effective aperture size is L_x = 2.2 mm and L_y = 3.2 mm. According to Equation (3-15), the far-field beam divergence is

$$\mathrm{Divergence}_x = \frac{\lambda}{L_x} = 0.040^\circ, \quad \mathrm{Divergence}_y = \frac{\lambda}{L_y} = 0.027^\circ. \tag{3-25}$$

The device fabrication flow is summarized in Figure 3-8. (1) The OPA is fabricated on a silicon wafer. (2) A 1 μm thick low-stress silicon nitride (SiN) layer is deposited for electrical insulation, and trenches with 0.5 μm etching depth and 2 μm width are patterned for interconnect lines. (3) The SiN trenches are filled with doped polysilicon followed by chemical mechanical polishing to create electrical interconnects. (4) A second layer of low-stress SiN is deposited, and via trenches are patterned. (5) The via trenches are filled with doped polysilicon followed by chemical mechanical polishing. Then another 500 nm thick doped polysilicon layer is deposited and patterned to create a grounded shield to prevent electrical interferences between interconnect wires and comb-drive actuators on top. (6) A 500 nm thick sacrificial silicon dioxide layer is deposited, chemical mechanical polished, and patterned to create anchor holes for MEMS comb-drive actuators. (7) A 2 μm thick doped polysilicon layer is deposited and chemical mechanical polished. (8) The comb-drive actuator and spring beam structures are defined by a silicon deep reactive ion etching process with a 300 nm critical dimension. (9) A 2 μm thick oxide layer is

deposited to encapsulate the MEMS comb-drive actuators, followed by chemical mechanical polishing planarization. Then the top sacrificial oxide layer was patterned to create 500 nm deep top grating layer anchor. (10) The top grating structure is defined with a thickness of 500 nm, a grating depth of 380 nm, and a metal coating of 50 nm. (11) The MEMS structures are released.

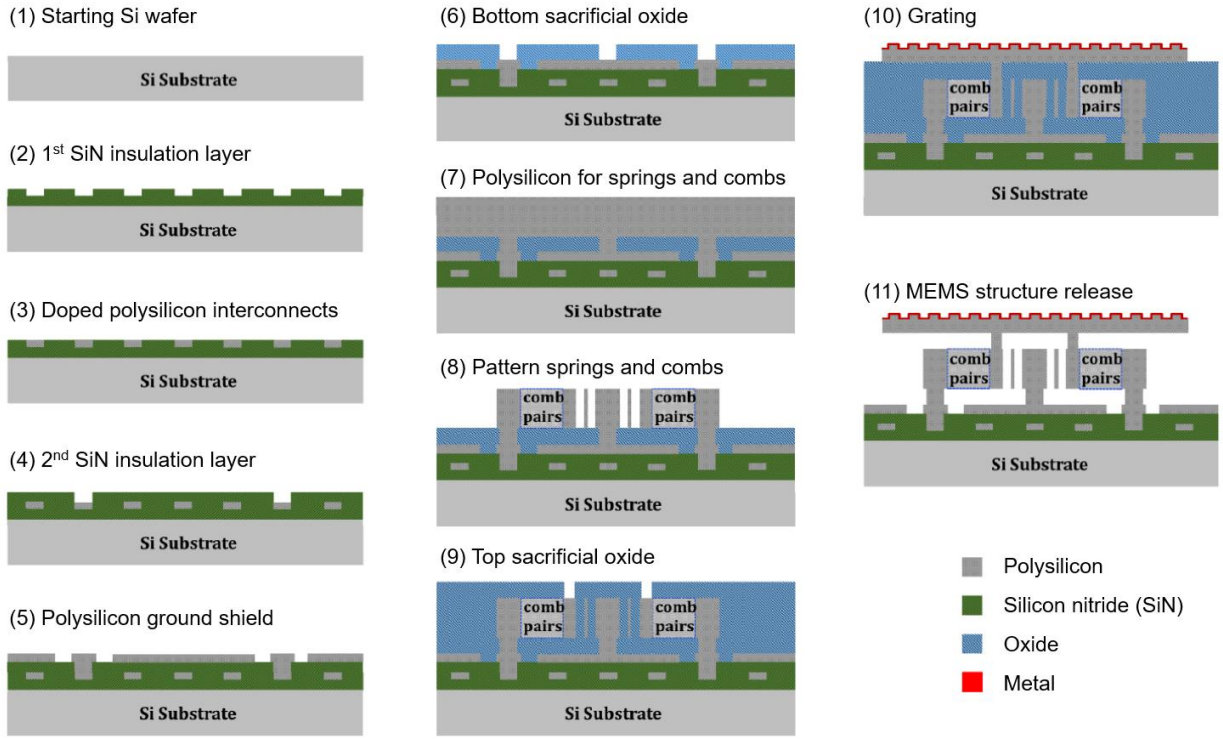

Figure 3-8. Grating-based OPA fabrication process flow.

3.3 Device characterization

3.3.1 Microscopic images

Some photos and microscopic images of the fabricated grating-based 2D MEMS OPA are shown in Figure 3-9. The OPA chip has a 10×10 mm^2 size, and the active OPA aperture is 3.1×3.2 mm^2. Figure 3-9(a) shows a comparison of the OPA chip with a US quarter dollar coin. Figure 3-9(b) shows an optical microscope image of the OPA chip. The dashed box in the center indicates the active OPA aperture composed of grating phase shifters and MEMS comb-drive actuators. Wire bonding pads are located on the four edges of the chip, connecting to the phase shifters via doped polysilicon electrical interconnects. Due to the limited number of wire bonding pads, the 160×160 grating phase shifters are grouped into 8×16 subarrays addressed by 256 electrical signals. Figure 3-9(c) shows a scanning electron microscope (SEM) image of one grating phase shifter. The holes on the grating are for MEMS structure release in the fabrication process. Figure 3-9(d) shows an SEM image of the OPA.

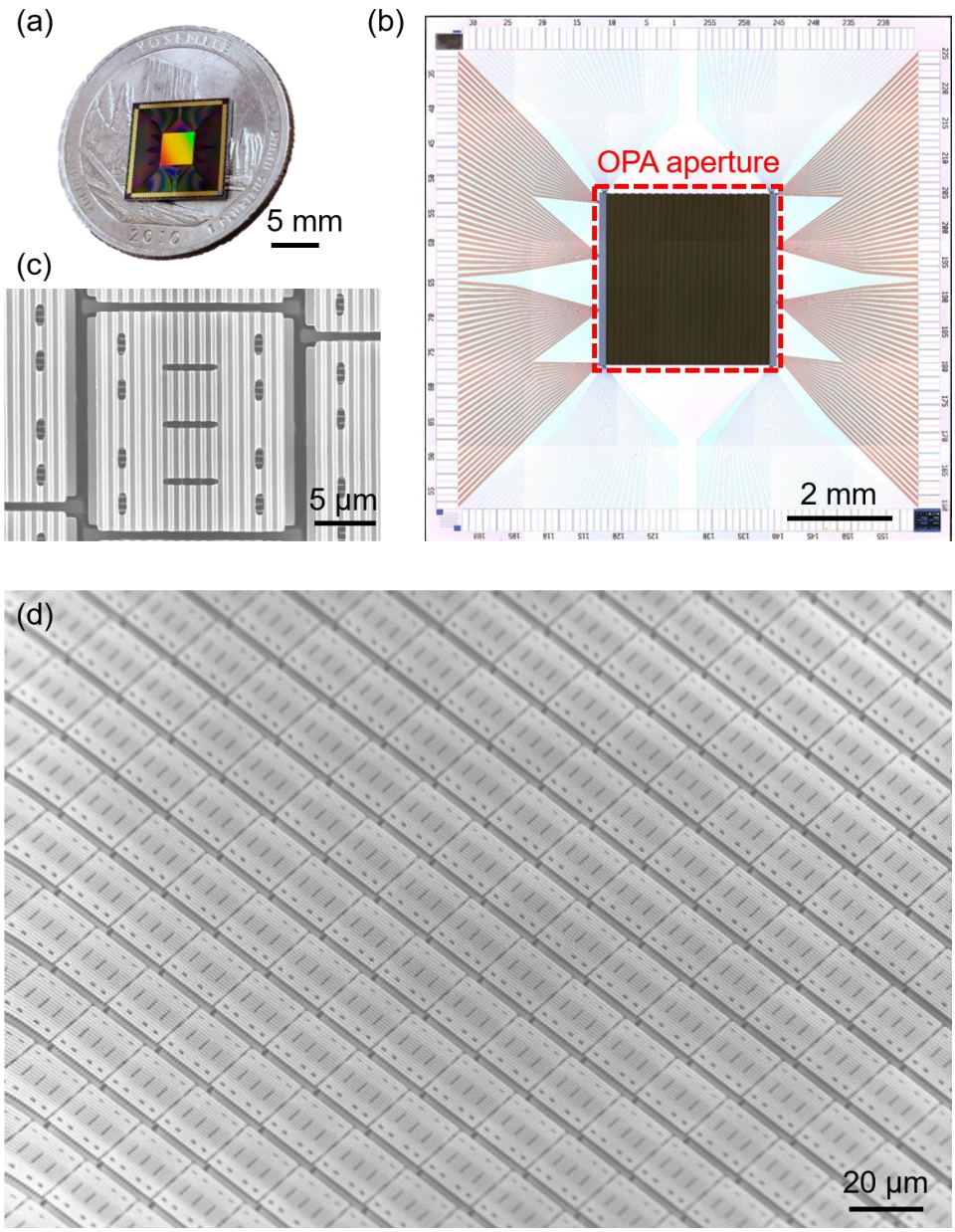

Figure 3-9. Photos and microscopic images of the grating-based MEMS OPA.

(a) Photo of the OPA chip on a US quarter dollar coin. (b) Microscopic image of the OPA. (c) and (d) SEM images of one grating phase shifter and the OPA.

3.3.2 Electrical characteristics

To characterize the MEMS comb driver actuators, the displacement of the grating phase shifters as a function of the applied voltage is measured for 12 grating elements at different locations on the OPA. The measurement results are shown in Figure 3-10 with quadratic fittings. The data shows that the grating displacement is proportional to the square of the applied voltage, agreeing

with the theoretical analysis in Equation (3-23). A 477.5 nm displacement in both directions is required for a full 2π phase shift, which can be achieved with a 10.5 V voltage on average.

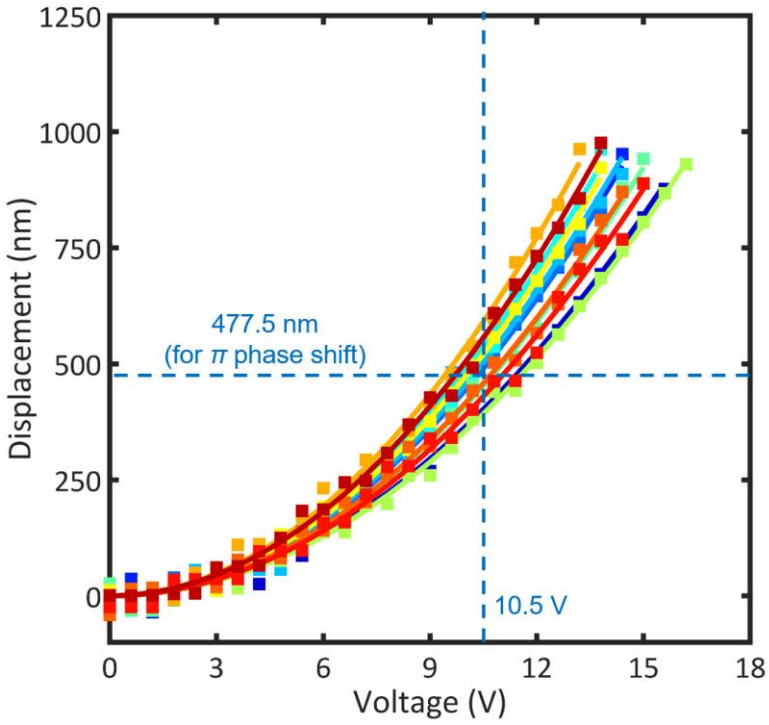

Figure 3-10. Measured transfer curves of 12 grating phase shifters.

The measurements also indicate that the grating phase shifter actuation is not uniform throughout the OPA due to the fabrication imperfections. This introduces phase control errors when the OPA is operated in an open loop. To address this issue, each grating phase shifter needs to be individually characterized and calibrated, which requires a large number of experimental measurements. Alternatively, an optimization algorithm can be used to compensate for the non-uniformity by optimizing the applied voltages to all the phase shifters together according to the far-field beam quality. Details of the optimization procedure are discussed in [38].

The actuation speed of the grating phase shifter is characterized by measuring its frequency response, shown in Figure 3-11. The measurement shows a second-order system behavior as expected, with a resonant frequency at 55 kHz indicating the grating phase shifter can reach the desired displacement in tens of microseconds. The grating phase shifter displacement response under a step voltage actuation is shown in Figure 3-12 left. The measurement results show a damped oscillation behavior with ±10% settling time at 92.5 μs. To further reduce the actuation time, a shaped actuation waveform with three steps can be used to suppress the oscillation, shown in Figure 3-12 right. With the shaped actuation waveform, the actuation time is significantly reduced to only 5.7 μs, enabling fast phase shifting and agile beam steering.

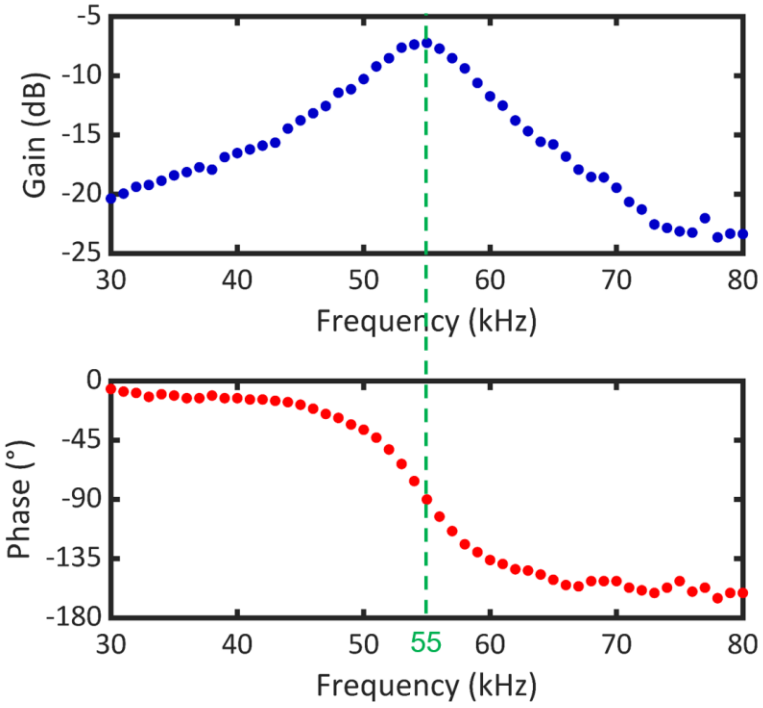

Figure 3-11. Measured frequency response curve of the grating phase shifter.

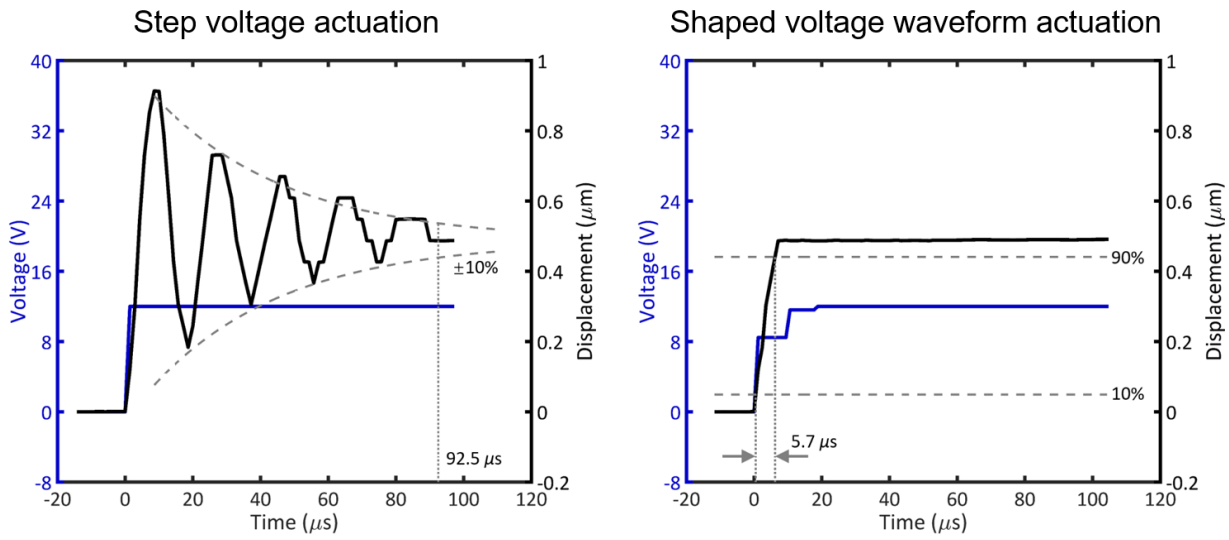

Figure 3-12. Grating phase shifter responses under step and shaped voltage waveforms.

3.3.3 Beam steering

The OPA is electrically controlled to steer the -1st order diffraction beam to 17×9 distinct angles within the 6.6°×4.4° FoV. The far-field beam spots are captured by an infrared (IR) camera placed at the back focal plane of a Fourier lens as shown in Figure 3-13. The overlapped beam

steering spot pattern is shown in Figure 3-14(a). The results show that the OPA steers the beam to distinct far-field angles with a clean background as expected.

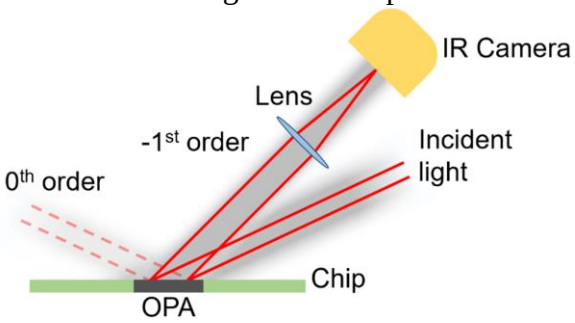

Figure 3-13. OPA optical characterization setup.

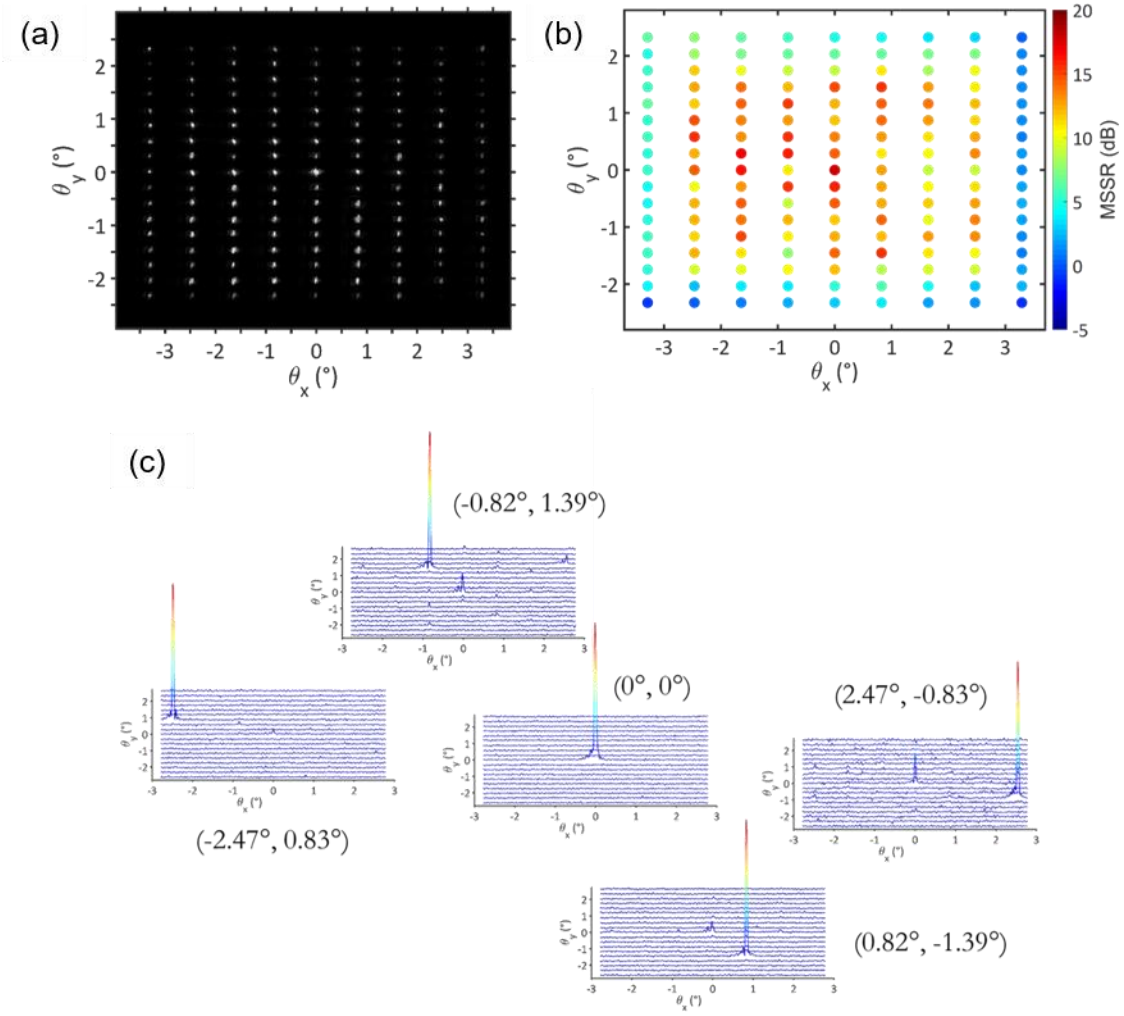

Figure 3-14. Beam steering characteristics of the OPA.

(a) Overlapped far-field beam steering pattern. (b) Main-to-side lobe suppression ratio of the beam spots at different steering angles. (c) Intensity distribution in the FoV at five beam steering angles.

To further show the contrast of the beam spot with the background, the main-to-side lobe suppression ratio (MSSR) of the steered beam spots are measured and shown in Figure 3-14(b). The MSSR is defined as the ratio of the maximum intensity of the beam spot at the desired steering angle (the main lobe) and the maximum intensity outside of the main lobe. The results show that the central FoV has an MSSR higher than 10 dB. The edge of the FoV has a lower MSSR due to the sinc^2 shape of the far-field profile of the individual grating phase shifter and the appearance of another grating lobe.

The details of the intensity distributions in the FoV when the beam is steered to five different angles are shown in Figure 3-14(c). Besides the beam spot at desired steering angle, a lower intensity spot may also appear at the center of the FoV, which is due to the phase control error discussed in the previous section.

The above beam steering measurement results verify that the fabricated OPA device is able to steer the -1st order diffraction beam to distinct far-field angles as designed. If each of the 160×160 grating phase shifters could be individually addressed, the achievable beam steering angles in the FoV would be significantly increased.

3.3.4 Beam profile

The far-field beam divergence of the steered beam is measured by the same setup shown in Figure 3-13 with a longer focal length Fourier lens. The measurement results and a comparison with the theoretical 0.040°×0.027° divergence of the sinc^2 profile are shown in Figure 3-15. The measured beam divergence is 0.042°×0.031°. The slightly larger measurement results than the theoretical diffraction limit values may be due to the array non-uniformity.

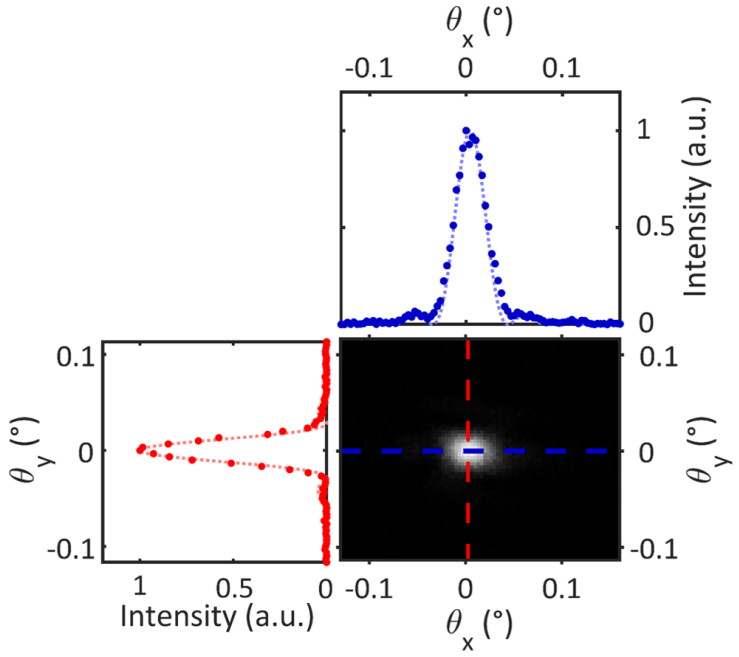

Figure 3-15. Far-field beam divergence measurement results.

In addition to capturing the far-field intensity distribution on the focal plane of a Fourier lens, the OPA output beam profile is also directly measured by the IR camera sensor after a 5 m

free-space propagation, shown in Figure 3-16. A simulated theoretical beam profile using the Fresnel diffraction integral is also shown in the figure for comparison. The cross-sections of the intensity profiles along the *x* and *y* axes show that the measured beam profile generally agrees with the simulation. By calibrating the transfer curves of the grating phase shifters and improving the array fabrication uniformity, the far-field beam profile can be improved even closer to the theoretical diffraction limit.

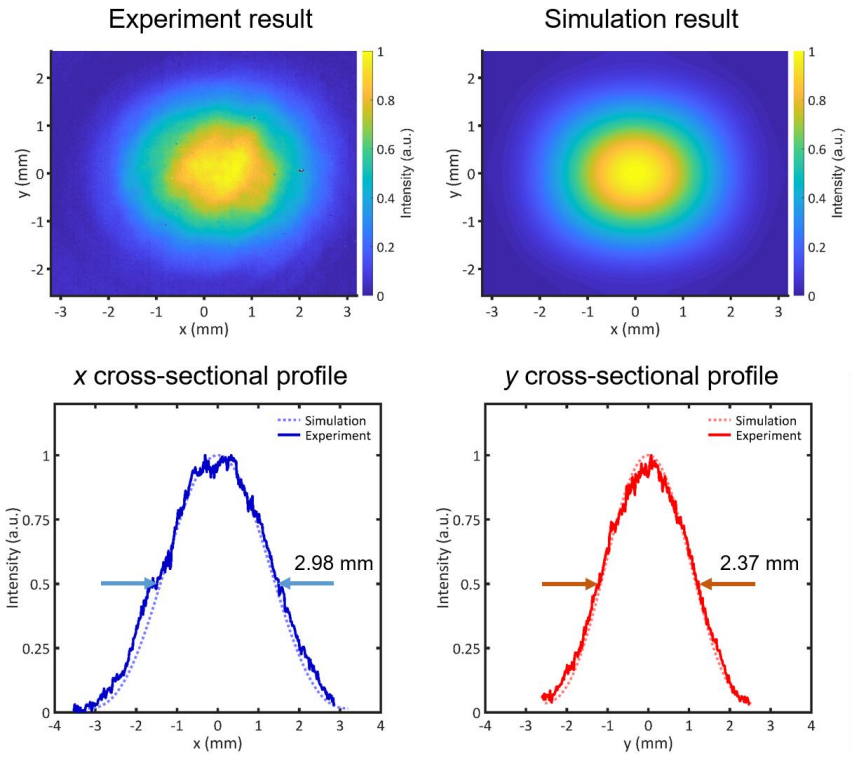

Figure 3-16. Beam profile after 5 m free-space propagation.

3.3.5 Optical efficiency

One of the advantages of the grating-based OPA working with free-space light is the high optical efficiency. By selecting the grating period and incident angle, most of the incident light power can be diffracted to the desired -1st order diffraction beam. Coating the polysilicon grating with metal like gold or aluminum can further increase the efficiency to near unity.

The simulated and measured optical efficiency of the -1st order diffraction of the OPA grating (Λ = 955 nm, thickness = 500 nm) with different materials (silicon, gold, and aluminum) as a function of operating wavelength (905 nm, O-band, and C-band, at a fixed 300 nm etching depth) and grating etching depth (at a fixed 1550 nm wavelength) are shown in Figure 3-17. The simulation is performed using the rigorous coupled-wave analysis (RCWA) algorithm. While the efficiency of the silicon grating is lower than 20%, with gold or aluminum coating the efficiency can be enhanced to about 90% in a broad band of wavelength according to the simulation. The measurement data for the silicon grating generally agrees with the simulation results, while the

measurements of the gold and aluminum-coated grating deviate from the simulation. We believe this is due to the poor step coverage of the metal coated by evaporation.

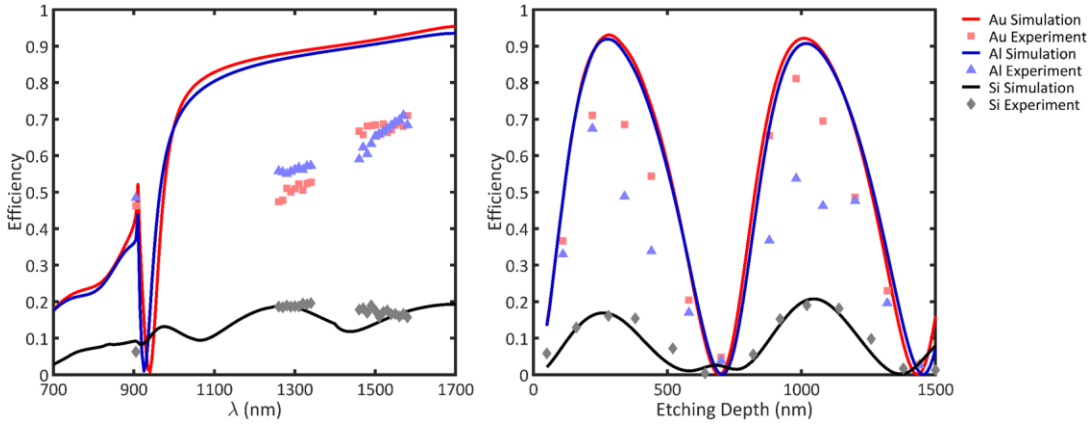

Figure 3-17. OPA grating diffraction efficiency versus wavelength and etching depth.

3.3.6 Hologram generation

As discussed in section 3.1.3, OPA has applications beyond beam steering. The full control of phase and amplitude on the OPA plane enables the capability of generating complicated holographic patterns in the far-field. To demonstrate this, passive grating-based OPAs (without the MEMS actuators) are fabricated in which the phase distributions for several complex holographic patterns are encoded. Figure 3-18 shows an example SEM of a passive grating-based OPA with a 10 μm pitch. The captured "Cal" logo and Golden Gate Bridge holographic patterns generated at the -1st order of two passive OPAs at 1550 nm wavelength are also shown in the figure. The experimental results show that high-resolution holographic patterns can be generated by the grating-based OPA. We believe reconfigurable holograms can be achieved by the active OPA with MEMS actuators and full electrical addressing.

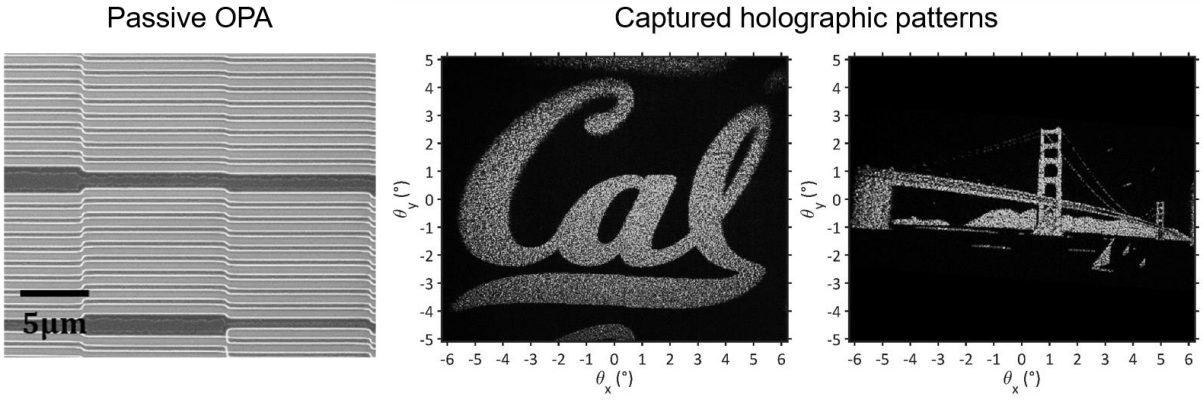

Figure 3-18. Passive OPA and holographic patterns.

3.4 Chapter summary

In this chapter, we introduced the principle, parameters, common architectures, advantages, and challenges of OPA as an optical beam scanner. We then demonstrated a 160×160-element grating-based MEMS OPA for optical beam steering. The key specifications of the demonstrated OPA device are summarized in Table 3-2.

Table 3-2. Specifications of the grating-based MEMS OPA.

Mechanical and electrical specifications		Optical specifications	
Element number	160×160	Grating period	955 nm
Array pitch	19.1 μm × 20 μm	Incident/output beam angles	65°/45°
Aperture size	3.1 mm × 3.2 mm	FoV	6.6°×4.4°
Resonant frequency	55 kHz	Divergence	0.040°×0.027°
2π actuation voltage	10.5 V	Operating wavelength	1200 – 1700 nm
Response time	5.7 μs	Efficiency (Au coated)	> 85%

The grating phase shifter and MEMS actuator architecture offer some unique advantages compared with OPAs in other architectures. The MEMS actuators have a fast response speed. The gratings have high optical efficiency in a broad wavelength band covering most of the optical communication and LiDAR wavelengths. The free-space operation also simplifies the optical alignment procedure. A large 2D array can be achieved without complicated on-chip waveguide routing that is challenging in the silicon photonics OPAs.

There are still challenges in scaling up the OPA architecture, especially in terms of maintaining high fabrication and control uniformity, electrically addressing a large number of phase shifters, and achieving a wavelength-scale array pitch for a large FoV. Many recent research works have reported on advanced technologies to address these issues, such as CMOS integration with MEMS and silicon photonics [35], compact phase shifter designs [39], reducing the electrical signal numbers [40], aperiodic OPA for side lobe suppression [41], increasing phase error tolerance by inverse design algorithms [42], and small pitch low crosstalk waveguides [43]. With the development of silicon photonics and MEMS technologies, we believe large-scale 2D OPA with large FoV and fast response can be realized that meets the requirement of many applications including and beyond chip-scale integrated LiDAR sensors.

The work in sections 3.2 and 3.3 of this chapter was performed with advising from Dr. Youmin Wang. I would like to thank Dr. Guangya Zhou for his contributions in the grating phase shifter theory, and Dr. Kyungmok Kwon, Dr. Pierre-A Blanche, Nicholas Triesault, and Dr. Kyoung-sik Yu for their collaborations in device design and fabrication [38].

4 Silicon photonics focal plane switch array (FPSA)

4.1 FPSA beam scanner introduction

4.1.1 FPSA beam scanner principle

FPSA beam scanner employs the imaging-based beam steering principle and works like an inverse camera, as shown in Figure 4-1. An array of optical antennas is located at the back focal plane of a convex lens (called the device lens) with a focal length *f*. The array has a pitch of *l* and a total size of *L*. The size of each antenna is *W*. To clarify the nomenclatures, hereafter we will refer to the optical antenna and switch array as the FPSA, and refer to the system composed of the FPSA and the device lens as the FPSA beam scanner.

Each optical antenna in the FPSA is connected to the input port via an optical switch. When one of the switches is turned on, the input light will be routed to the corresponding antenna and emitted to the free space. To derive the beam steering equation, we assume the antenna is much smaller than the lens aperture, therefore can be considered as a point source. According to the geometric optics rules, light emitted from a point source on the focal plane of a convex lens will become a parallel beam after the lens. The angle between the optical beam and the optical axis is

$$\theta = -\arctan\left(\frac{x}{f}\right), \tag{4-1}$$

where *x* is the coordinate of the emitting antenna with respect to the optical axis. The minus sign in the equation indicates the antenna and the output beam direction are on opposite sides of the optical axis.

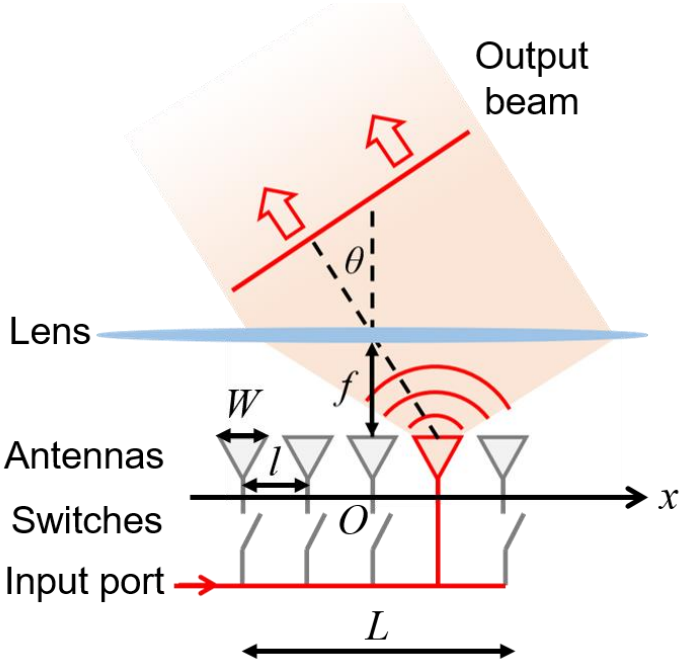

Figure 4-1. Schematic of FPSA beam scanner.

The above derivation is according to the property of an ideal thin lens where all the optical aberration effects are ignored. The selection of lens and aberration effects will be discussed in detail later in this chapter. In addition, some special lens designs may have a mapping function, i.e. the angle θ versus position x relation, in a form other than the arctan function. For example, an equidistance fisheye lens has a linear relation $\theta = -r/f$, and an orthographic fisheye lens has an arcsin relation $\theta = -\arcsin(r/f)$, etc [44]. However, as long as the lens creates a distinct mapping from the location on the focal plane to the output collimated beam angle, the principle of the FPSA beam scanner discussed above will be valid.

Although here we show an FPSA beam scanner transmitting collimated beam to the far-field, the FPSA beam scanner can also be used as a receiver where optical beams coming from different angles are received by the corresponding antennas and coupled back to the input port via the optical switches.

4.1.2 FPSA beam scanner parameters

From the analyses in the previous section, we can derive some important parameters for the FPSA beam scanner.

(1) Beam steering FoV.

From Equation (4-1), the largest beam steering angle θ is achieved at the farthest optical antenna location $x = \pm L/2$. Therefore the FoV is

$$\mathrm{FoV} = 2\arctan\left(\frac{L}{2f}\right). \tag{4-2}$$

The equation suggests that a large FoV can be achieved by a large array size L or a small focal length f. Unlike the FoV dependence on the array pitch in an OPA, the FoV does not depend on the array pitch in an FPSA beam scanner, thus a wavelength-scale pitch is not required to achieve a large FoV.

Although Equation (4-2) shows a FoV smaller than 180°, a full 180° or even larger FoV can be realized by special wide-angle lens designs such as a fisheye lens.

(2) Beam steering resolution.

Since the FPSA beam scanner steers the beam based on a location-angle mapping, the beam steering angles are discrete. The angle between adjacent steering angles is defined as the beam steering resolution,

$$\mathrm{Resolution} = \left|\frac{d\theta(x)}{dx}\right| l = \frac{f}{f^2 + x^2} l. \tag{4-3}$$

The resolution depends on the location of the antenna due to the nonlinear arctan mapping. The angular separation between adjacent beams becomes smaller at the edge of the array. The lowest resolution occurs at the center of the array, i.e. $x = 0$, so we can approximate the FPSA beam steering resolution by

$$\mathrm{Resolution} = \frac{f}{f^2 + 0} l = \frac{l}{f}. \tag{4-4}$$

A higher resolution can be achieved by a smaller array pitch l or a longer lens focal length f.

Assume there are N antennas in the array (or in one direction of a 2D array), the array size and pitch have the relation

$$l = \frac{L}{N-1}, \tag{4-5}$$

therefore the FoV and resolution are approximated related with each other by

$$\text{Resolution} \approx \frac{\text{FoV}}{N-1}. \tag{4-6}$$

To achieve a large FoV and a high resolution at the same time, a large-scale FPSA with a large antenna count N is desired.

(3) Beam spot divergence.

The far-field beam divergence of the FPSA beam scanner can be derived from two perspectives. From a geometric optics point of view, the beam divergence is because that the actual antenna is not an ideal point source but has a size of W. Therefore, the beam steering angle corresponds to a range of locations on the focal plane shown in Figure 4-2, i.e. the beam divergence is

$$\text{Divergence} = \frac{W}{f}. \tag{4-7}$$

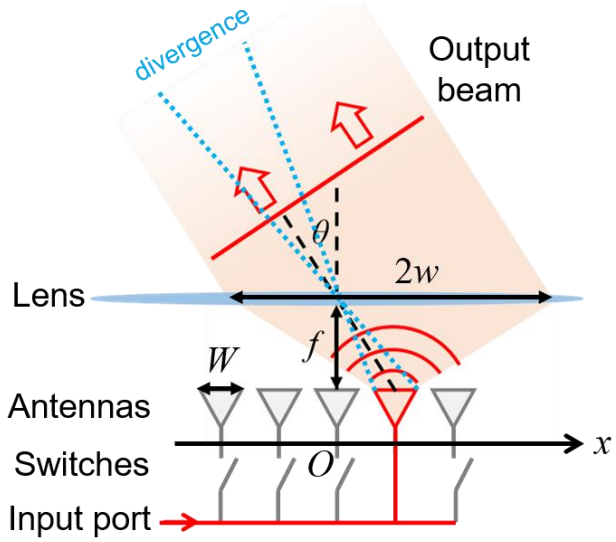

Figure 4-2. Schematic for FPSA beam scanner divergence angle derivations.

The divergence angle can also be derived from a wave optics point of view by the diffraction theory. The emitted light from the antenna with a size W has a diffraction limit λ/W, therefore on the lens the beam diameter size is approximately

$$2w = \frac{\lambda}{W} f, \tag{4-8}$$

where w is the beam radius and λ is the optical wavelength. The divergence of the far-field beam is due to the diffraction from this beam size on the lens if the lens aperture is larger than $2w$, therefore the diffraction limit divergence angle is

$$\text{Divergence} = \frac{\lambda}{2w} = \frac{\lambda}{\frac{\lambda}{W} f} = \frac{W}{f}. \tag{4-9}$$

Note that the geometric optics and wave optics derivations result in the same estimation of the far-field beam divergence.

(4) Beam spot profile.

Although the beam divergence can be estimated by Equation (4-7) or (4-9), the detailed far-field intensity profile of the steered beam depends on multiple factors including the emission profile of the optical antenna, the phase delay through the lens, and the aperture of the lens. A two-step diffraction integral analysis is necessary to obtain the precise beam profile, first from the antenna propagating to the lens, and second from the lens propagating to the far-field.

However, since the emission profile of many optical antennas can be approximated by a Gaussian beam profile, we can derive the far-field beam properties using the Gaussian beam model. The parameters of a Gaussian beam can be described using the complex beam parameter q defined as

$$\frac{1}{q(z)} = \frac{1}{R(z)} - i\frac{\lambda}{\pi w^2(z)}, \tag{4-10}$$

where z is the beam propagation distance from the beam waist location, R is the radius of curvature of the phase front, and w is the beam radius. We assume the antenna location $z = 0$ is the beam waist location where the phase front is flat with $R = \infty$, and the beam waist radius is approximately half the antenna size, i.e. $w(0) = W/2$. Therefore the q parameter of the Gaussian beam at the antenna is

$$\begin{aligned} &\frac{1}{q(0)} = \frac{1}{R(0)} - i\frac{\lambda}{\pi w^2(0)} = -i\frac{4\lambda}{\pi W^2}, \\ &q(0) = i\frac{\pi W^2}{4\lambda}. \end{aligned} \tag{4-11}$$

According to the ABCD matrix analysis method, after a propagation distance f, at the device lens the Gaussian beam parameter is

$$q(f) = q(0) + f = f + i\frac{\pi W^2}{4\lambda}. \tag{4-12}$$

After transformed by the ideal device lens with an ABCD matrix $\begin{bmatrix} 1 & 0 \\ -\frac{1}{f} & 1 \end{bmatrix}$, the Gaussian beam parameter is

$$q'(f) = \frac{fq(f)}{f - q(f)} = \frac{f\left(f + i\frac{\pi W^2}{4\lambda}\right)}{-i\frac{\pi W^2}{4\lambda}} = -f + i\frac{4\lambda f^2}{\pi W^2}. \tag{4-13}$$

This indicates that the beam waist of the Gaussian beam output from the device lens is located at $z = 2f$, i.e. at the front focal plane of the lens. At the beam waist, the q parameter is

$$q'(2f) = q'(f) + f = i\frac{4\lambda f^2}{\pi W^2}, \tag{4-14}$$

i.e.

$$\frac{1}{q'(2f)} = -i\frac{\pi W^2}{4\lambda f^2} = -i\frac{\lambda}{\pi\left(\frac{\lambda f}{\pi W}\right)^2}. \tag{4-15}$$

Therefore, the beam waist radius of the Gaussian beam output from the device lens is $\frac{\lambda f}{\pi W}$, and the full-width half-maximum (FWHM) divergence angle is

$$\frac{\sqrt{2\ln 2}\lambda}{\pi\left(\frac{\lambda f}{\pi W}\right)} = \sqrt{2\ln 2}\frac{W}{f} \approx 1.18\frac{W}{f}. \tag{4-16}$$

This result is similar to the estimation by Equation (4-7) or (4-9) only with a constant factor of 1.18. In conclusion, if the antenna emits a Gaussian beam, the output beam from the device lens is still a Gaussian beam with waist radius $\frac{\lambda f}{\pi W}$ and FWHM divergence angle of $1.18\frac{W}{f}$.

(5) Lens aberrations.

Aberrations of the lens such as spherical aberration, coma, and distortion will affect the far-field beam profile, especially for off-axis antennas. Details of the aberration effects can be analyzed by ray-tracing simulations of the lens.

The demand for a low-aberration convex lens for the FPSA beam scanner is nothing different from the demand for a low-aberration camera lens. The camera lens is a mature industry with highly optimized lens designs meeting different demands such as large aperture, extremely short or long focal length, large FoV, long working distance, and small footprint. Therefore, the

FPSA beam scanner can benefit from the camera lens industry and utilize the well-optimized camera lenses to achieve the lowest aberration and highest beam quality.

The analyses above are summarized in Table 4-1.

Table 4-1. Summary of important FPSA beam scanner parameters.

Beam steering parameter	Related FPSA parameter	Equation
Beam steering angle θ	Antenna location x Device lens focal length f	$\theta = -\arctan\left(\frac{x}{f}\right)$
FoV	Array size L	$2\arctan\left(\frac{L}{2f}\right)$
Resolution	Array pitch l	$\frac{l}{f}$
Divergence	Antenna size W	$\frac{W}{f}$
Beam spot profile	Antenna emission profile Device lens properties	–

4.1.3 Advantages and challenges

The most significant advantage of the FPSA beam scanner compared with the OPA is its digital switching control of one antenna at a time. Compared with the analog phase and amplitude control of all antennas at the same time in an OPA, the control scheme of the FPSA has much lower complexity, thus is more robust and tolerant to device fabrication non-uniformity.

Only one antenna needs to be turned on at a certain time during the beam steering, so for a 2D FPSA the row-column electrical addressing scheme can be employed so an $N \times N$ array can be fully addressed with only $2N$ electrical signals.

From the previous section, the FoV of the FPSA beam scanner can be increased by increasing the array size or decreasing the device lens focal length, eliminating the need to shrink the array pitch to the wavelength scale for a large FoV. All these advantages suggest that the FPSA is highly scalable and is a promising approach for a large-scale integrated beam scanner with fast speed and random access.

To achieve a practical FPSA for applications like LiDAR, a high-performance optical switch with fast response and low loss is desired. The MEMS optical switch architecture is a good candidate to address this challenge, and the details will be introduced in section 4.2.2.

The off-chip device lens poses another challenge to fully integrate the FPSA beam scanner. Fortunately, recent development of compact lenses for consumer electronics such as cellphones offers many optimized compact lens designs that can be utilized by integrated FPSA beam scanners. The considerations on lens selection will also be discussed in this chapter.

4.1.4 FPSA architectures and related work

Recently several integrated 1D and 2D FPSA devices have been reported, and they can be roughly classified by the optical switch architectures. One common optical switch architecture on the silicon photonics platform is the Mach-Zehnder modulator (MZM) switch, where the input light can be routed to one of the output ports depending on the relative phase delay of the two arms that is typically controlled by a thermal-optic phase shifter. Switching to more than two output ports usually requires a cascaded switch tree, which has a large footprint and high power consumption.

MEMS-based optical switches have also been applied in FPSA beam scanners. MEMS optical switches offer high speed and low loss optical switching with a small footprint, thus have enabled the large-scale FPSAs introduced in this chapter.

A comparison of the specifications of several recently reported integrated FPSAs is shown in Table 4-2 and Figure 4-3.

Table 4-2. Comparison of the specifications of reported integrated FPSAs.

Year	1D/2D	Element number	FoV	Optical switch	Antenna	Reference
2018	1D	4	5°	MZM	Slow-light waveguide grating	[45]
2019	1D	16	38.8°	MZM	Si grating	[46]
2019	1D	19	4.6°	MZM	Si grating	[47]
2020	1D	16	4.4°	MZM	Slow-light waveguide grating	[48]
2019	2D	16 (4×4)	12.4°×26.8°	MZM & micro-ring	Si micro-ring	[49]
2019	2D	16 (4×4)	2.07°×4.12°	MZM	SiN grating	[50]
2020	2D	16 (4×4)	1.05°×1.05°	MZM	Optical fiber	[51]
2021	2D	16 (8×2)	1.5°×0.9°	MZM	Si grating	[52]
2021	2D	512 (32×16)	1.5°×0.9°	MZM	Si grating	[52]
2020	2D	100 (10×10)	1°×1°	MEMS	Si grating	[53]
2020	2D	400 (20×20)	32°×32°	MEMS	Si grating	This work, [54]
2021	2D	16,384 (128×128)	70°×70°	MEMS	Si grating	This work, [55]

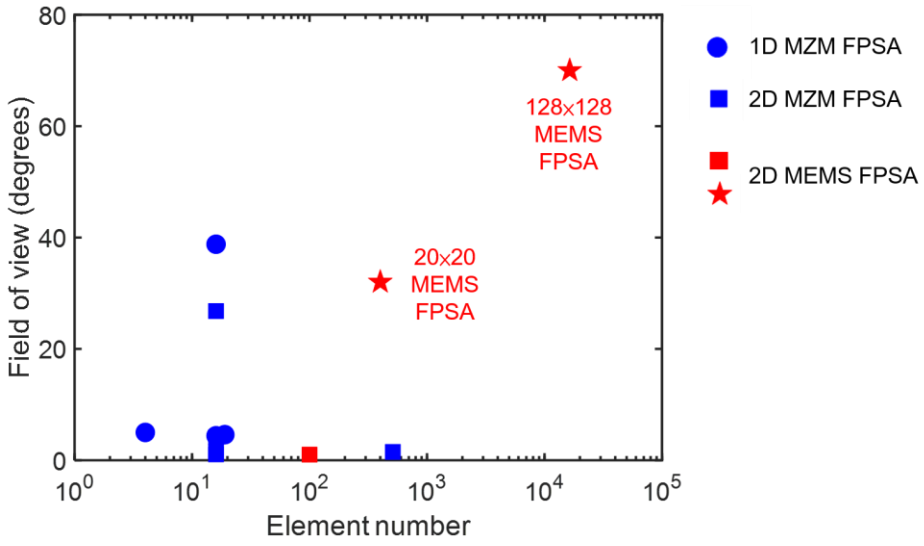

Figure 4-3. Comparison of reported integrated FPSAs.

4.1.5 Approaches for continuous beam steering

One limitation of the FPSA beam scanner is that its beam steering angles are discrete due to the discrete antenna array. This is usually not an issue for 3D imaging applications as long as the beam steering resolution meets the application requirements. However, in some applications a continuous beam steering is required, such as beam tracking in free-space optical communication between moving stations.

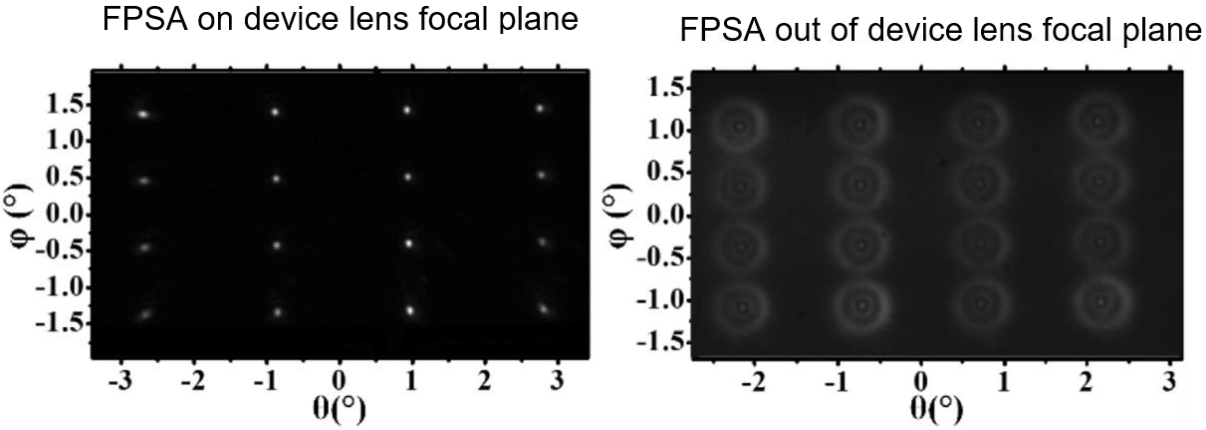

Figure 4-4. Beam steering pattern when FPSA defocused from the lens focal plane.

Reproduced from [50].

There are some approaches to fill in the blind zones between discrete beam steering angles and realize continuous beam steering with the FPSA beam scanner. One common and simple approach is to intentionally increase the beam divergence by defocusing the FPSA, i.e. moving the FPSA slightly out of the device lens focal plane. An experimental demonstration is shown in

Figure 4-4 [50]. Each beam spot covers a larger range of far-field angles, therefore the blind zones between the discrete beam steering angles are partly eliminated. However, this approach does not increase the number of resolvable spots, and it lowers the optical power per unit area in the beam spots.

The second approach is to steer the beam between two adjacent discrete angles by some mechanical actuation. A straightforward method is to move the lens or the FPSA by a motorized stage. A displacement equal to the array pitch l is required to fully eliminate the blind zones. However, moving the FPSA chip may be complicated due to the attached electrical addressing wires and optical input/output devices, and moving the lens may be slow due to the weight of the lens. A better way is to utilize a micro-lens array to create a virtual FPSA via imaging the real FPSA, and then continuous beam steering can be achieved by moving the micro-lens array within half the FPSA pitch, shown in Figure 4-5. The micro-lens array is light-weighted thus can be actuated faster. The drawback of this approach is the aberrations of the micro-lens array. Some research works also reported on implementing a MEMS scanning mirror to assist the continuous beam steering [56].

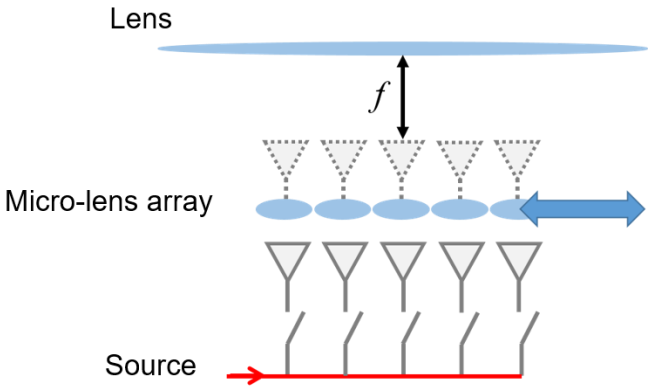

Figure 4-5. FPSA continuous beam steering by moving a micro-lens array.

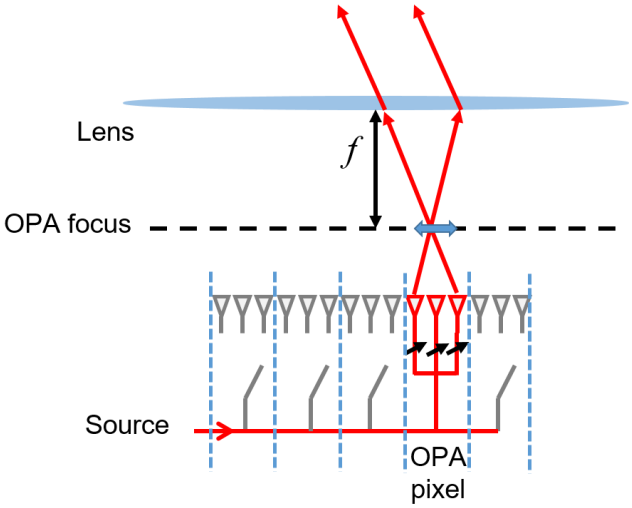

Figure 4-6. FPSA continuous beam steering by implementing OPA pixels.

A more sophisticated approach is to use a focusing OPA for each pixel of the FPSA, shown in Figure 4-6. When the corresponding pixel is turned on by the optical switch, the OPA will create a focused beam spot on the focal plane of the lens, acting as a virtual antenna. By controlling the phase in the OPA, this virtual antenna can be moved on the focal plane, thus achieving a continuous scan. This approach eliminates any moving parts, but introduces the extra complexity for OPA control, and has a design tradeoff between the divergence angle and the OPA pixel size.

For fully continuous beam steering in the entire FoV, all of the approaches above face the issue of the abrupt transition from one FPSA antenna to another when the beam is continuously steered passing the boundary between the area covered by adjacent FPSA antennas. Nevertheless, these methods provide some possible directions to achieve continuous beam steering and open up more applications for the FPSA beam scanners.

4.2 Design and characterization of a 20×20 FPSA

4.2.1 Design overview

In this section, we will introduce the design of the 20×20-element silicon photonics FPSA with MEMS optical switches. The top-view and perspective schematics of the 20×20 FPSA are shown in Figure 4-7, using a 4×4 array as an example. A 2D array of grating antennas is placed on the device layer of the silicon-on-insulator (SOI) platform. Each grating antenna is connected to a row waveguide via a column selection switch, and each row waveguide is connected to the input waveguide via a row selection switch.

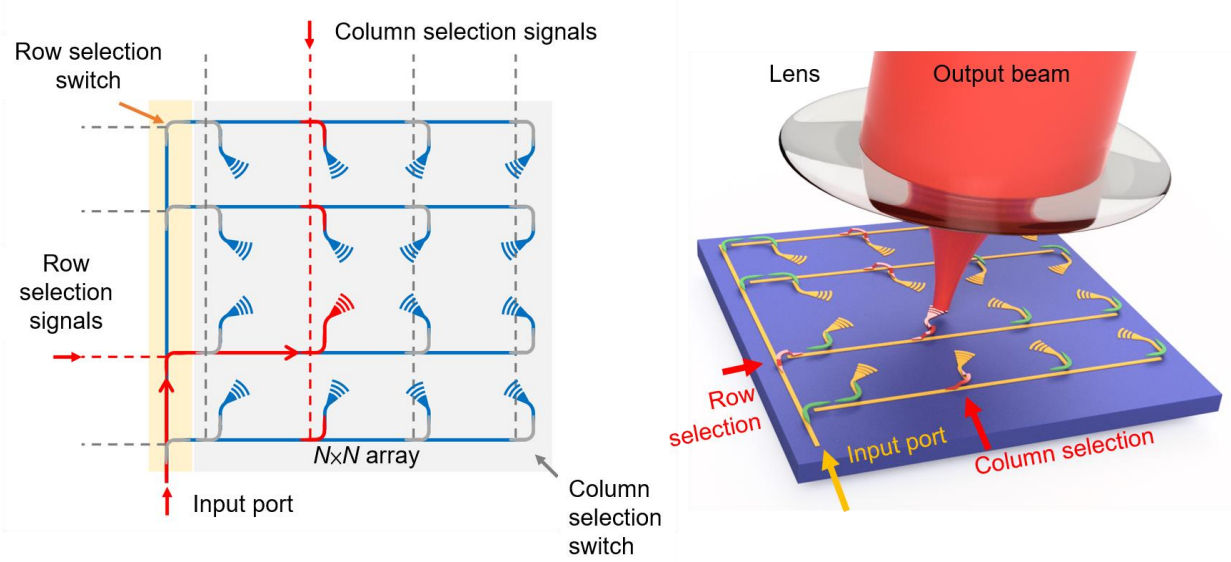

Figure 4-7. Schematics of the 20×20 FPSA beam scanner.

The optical switches are electrically addressed in a row-column addressing scheme. Each column of optical switches is electrically connected together, resulting in 4 column selection signals. Each row selection switch is individually addressed by a row selection signal. Therefore for an $N \times N$ array, there are only $2N$ electrical signals. By turning on a row selection switch and a column of column selection switches, light from the input port will be routed to the

corresponding grating antenna and emitted to free-space. Note that although the entire column of optical switches is turned on, light only propagates to one grating antenna due to the row selection switch. The FPSA is placed on the back focal plane of the device lens, so the emitted light will be collimated by the device lens, and the output angle is determined by the antenna location on the array. The device can also work inversely as a receiver.

The orientations and emission angles of the grating antennas are customized according to the location on the array so each antenna emits light towards the center of the device lens to increase the lens collection efficiency and reduce the aberration effects. The details of the optical switches and the grating antennas will be introduced in the following sections.

The designed 20×20 FPSA has a pitch l = 135 μm in both directions, and the overall array size is L = 2.57 mm in both directions. A singlet lens with a focal length f = 4.51 mm is selected for the FPSA beam scanner. The grating antenna has a focusing-curved shape with a size of 15 μm × 6.2 μm, and the size of the emission region (W) is about 5 μm. According to Table 4-1, the beam steering FoV, resolution, and divergence are

$$\text{FoV} = 2\arctan\left(\frac{L}{2f}\right) = 2\arctan\left(\frac{2.57}{2\times 4.51}\right) = 32^\circ, \tag{4-17}$$

$$\text{Resolution} = \frac{l}{f} = \frac{0.135}{4.51} = 1.7^\circ, \tag{4-18}$$

$$\text{Divergence} = \frac{W}{f} = \frac{0.005}{4.51} = 0.064^\circ. \tag{4-19}$$

4.2.2 MEMS optical switch

The MEMS optical switches in the 20×20 FPSA has a design similar to that report in [57], [58], and [59]. Schematics of the optical switch architecture are shown in Figure 4-8. The optical switch is composed of two waveguides on the SOI device layer and a polysilicon coupler. The two tips of the polysilicon coupler can be actuated by electrostatic parallel-plate MEMS actuators in the vertical direction.

In the OFF state, the MEMS actuators are in the up position, and the polysilicon coupler is far above the SOI waveguide. Light propagates from the input port to the through port without any disturbance. In the ON state, voltage is applied across the two plates of the MEMS actuators, and the two tips of the polysilicon coupler will be pulled down towards the SOI waveguide due to the pull-in effect of the parallel-plate actuator. The coupler is now in close proximity of the SOI waveguide, therefore couples light into the couplers and then down to the other SOI waveguide to the drop port. In the 20×20 FPSA design, the drop ports of the row selection switches are connected to the corresponding row waveguides, and the drop ports of the column selection switches are connected to the grating antennas.

This MEMS optical switch design has many advantages. It has zero optical loss in the OFF state, and zero electrical power consumption in steady states, and a fast actuation speed on the order of microsecond. In the ON state, the optical loss is lower than 1 dB. The footprint is small and several high-density integrations of large-scale 2D optical switch arrays have been reported

recently, shown in Figure 4-9. For example, in [59] a 240×240 optical switch array in a 4×4 cm^2 area with an optical loss as low as 0.04 dB/port is reported.

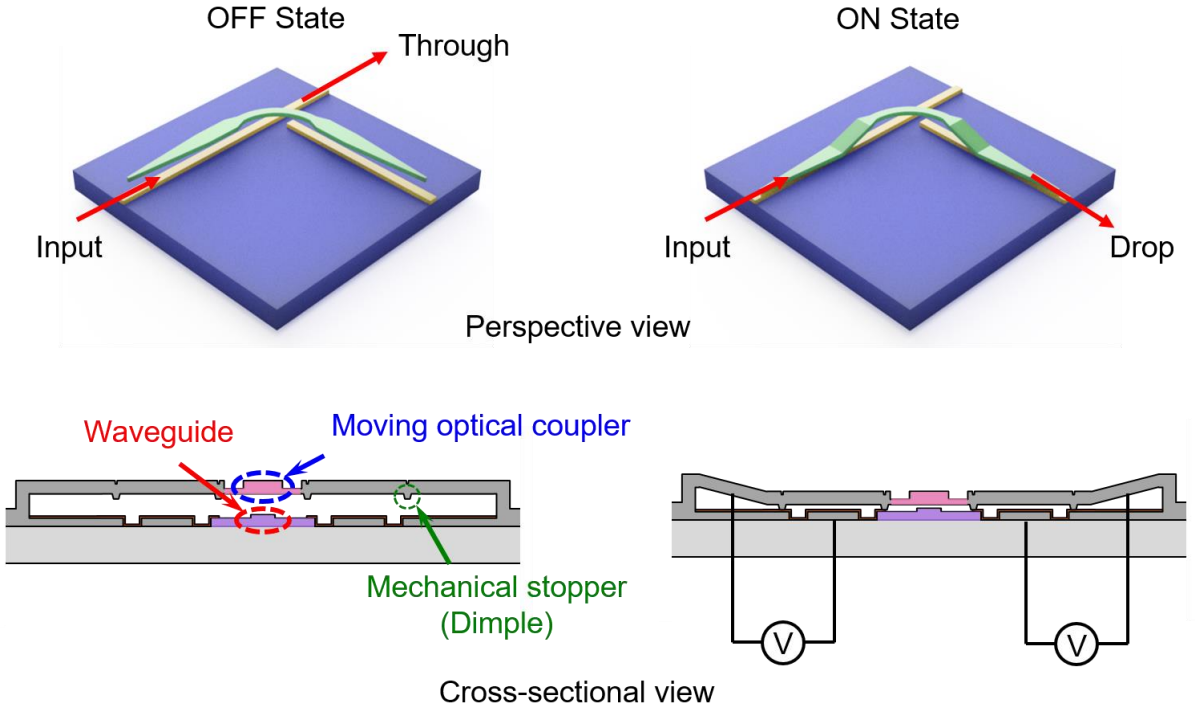

Figure 4-8. MEMS optical switch architecture.

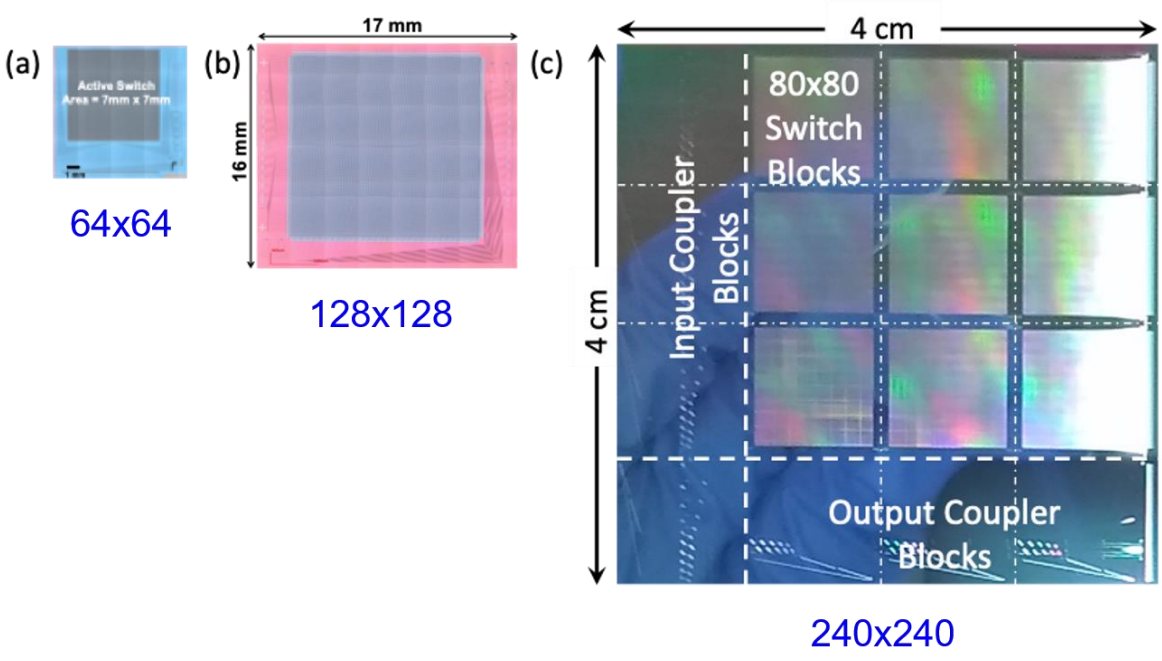

Figure 4-9. Chip photos of reported MEMS optical switch arrays in literature. Reproduced from (a) [57], (b) [58], and (c) [59].

The MEMS optical switch design has also been demonstrated to be highly reliable. It showed no performance degradation after 10 billion cycles of actuation, and no sign of stiction after being kept in the ON state for 48 hours [57]. This MEMS optical switch architecture is very suitable for large-scale FPSA beam scanners.

4.2.3 Grating antenna design

The grating antennas in the 20×20 FPSA are defined on the device layer of the SOI wafer by a partial etch, and the top of the gratings is air-clad. They have a focusing-curved shape with a size of 15 μm × 6.2 μm, and the size of the emission region (*W*) is about 5 μm, shown in Figure 4-10 top. The grating groove duty cycle is 50%.

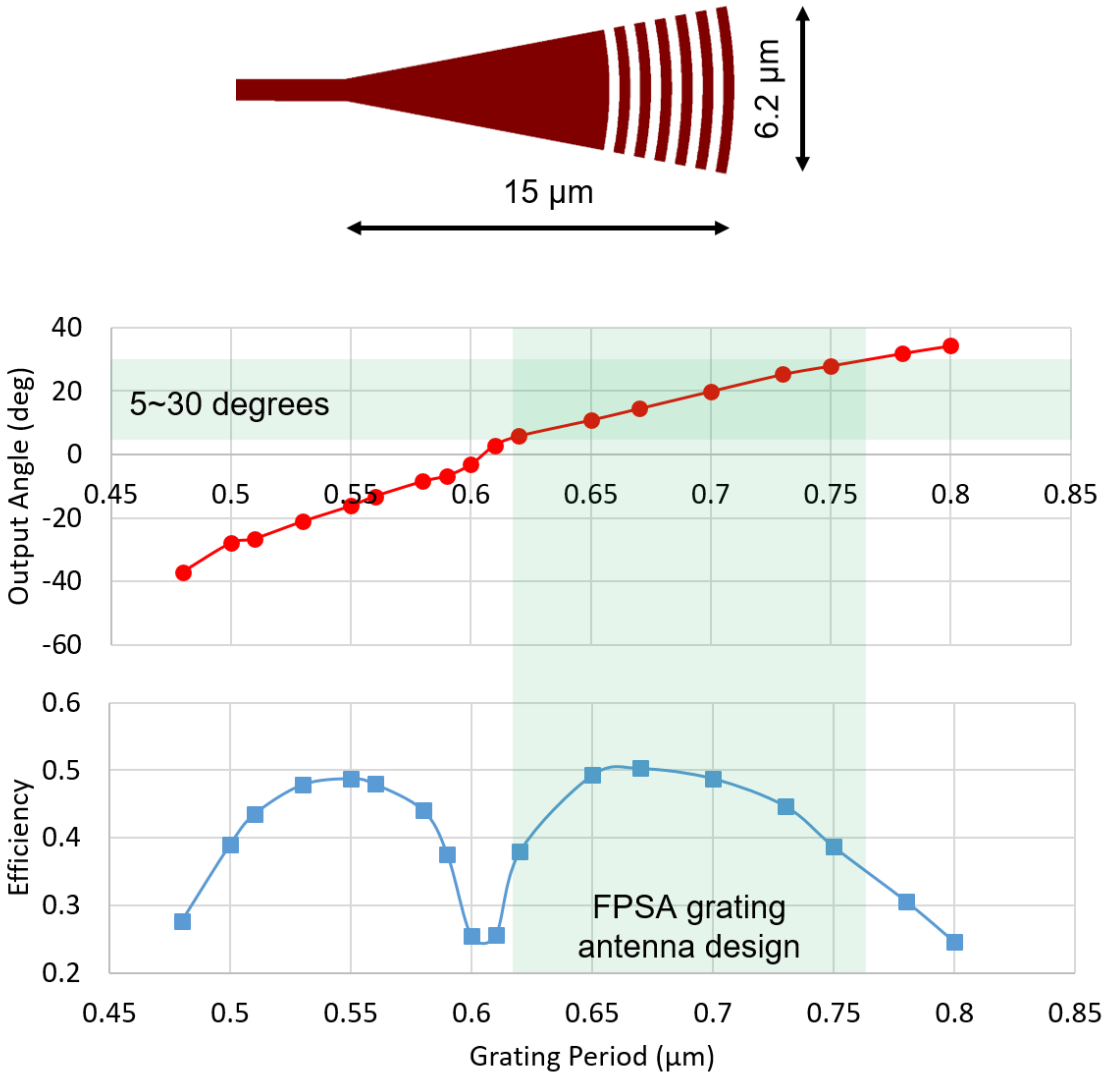

Figure 4-10. 20×20 FPSA grating antenna design and simulation results.

The grating periods are designed based on the grating antenna locations on the FPSA such that the center of the emitted light is directed towards the center of the device lens. The grating

antenna central emission angle and efficiency as a function of the grating period are simulated using the finite-difference time-domain (FDTD) method, and the simulation results are plotted in Figure 4-10 bottom. The efficiency curve has a significant dip as the output angle approaches 0, (the vertical direction) as expected. To ensure an output efficiency higher than 40% throughout the FPSA, we select the grating periods corresponding to a 5° to 30° output angle. For the grating antennas in the central area of the FPSA, if the calculated emission angle towards the lens center is smaller than 5°, a 5° design will be used. Similarly for the grating antennas on the edge of the FPSA, if the calculated emission angle towards the lens center is larger than 30°, a 30° design will be used. The grating antenna efficiency can be further increased by optimizing the geometry using methods such as inverse design [60][61].

4.2.4 Fabrication process and packaging

The 20×20 FPSA device is fabricated on a 220 nm SOI wafer with a standard silicon photonics process and an additional silicon nitride layer for edge coupling and a polysilicon layer for coupler waveguides and MEMS actuators. The fabrication process flow is shown in Figure 4-11. (1) The single-crystalline Si layer is patterned for input and row waveguides and grating antennas. A SiN layer is deposited and patterned for the edge coupler waveguides. Then the Si layer is doped by ion implantation for electrodes and electrical interconnects. (2) Sacrificial oxide is deposited and patterned for polysilicon anchors and dimples. Then the polysilicon layer is deposited. (3) The polysilicon layer is doped by ion implantation for electrodes and patterned to define the coupler waveguide and MEMS structures. (4) The edge coupler facet is etched, and a silicon carbide passivation layer is deposited and patterned to protect the oxide in the edge coupler region from being released. Metal is deposited and patterned by liftoff for wire bonding pads. Finally, the chip is diced from the backside and the MEMS structure is released.

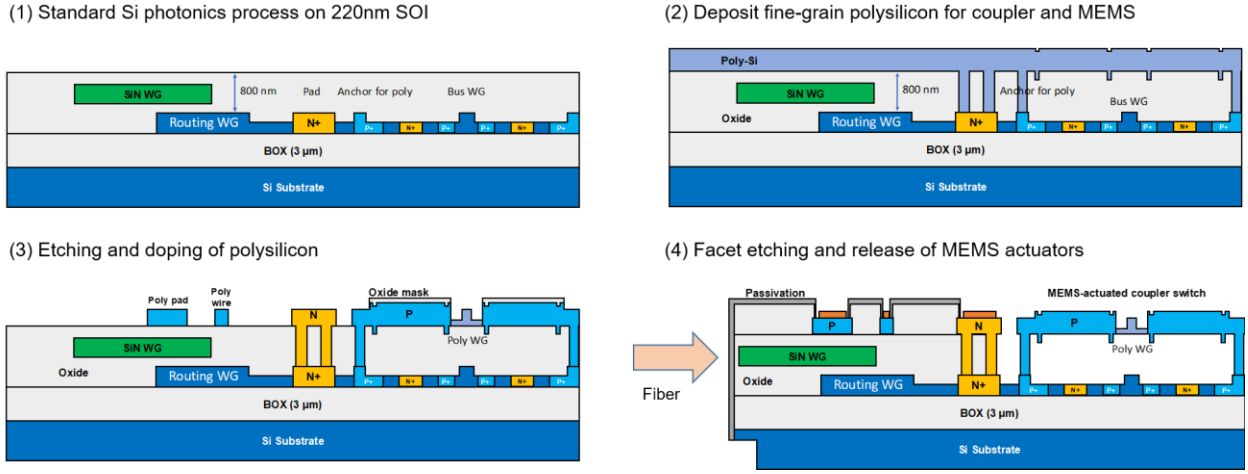

Figure 4-11. 20×20 FPSA fabrication process flow.

The fabricated FPSA chip is attached and wire-bonded to a customized carrier printed circuit board (PCB) to connect the 40 electrical addressing signals and the ground connection from external power supplies via a fan-out PCB. The electrical control can also be automated, which will be described later in this chapter for the larger FPSA in section 4.3.3. Light from the external optical setup is coupled into the FPSA from an optical fiber or a fiber array to the edge

coupler arrays on the chip. The optical coupling alignment is performed by tuning the optical fiber or fiber array by a stage while monitoring the signal from the alignment loop waveguide or monitor grating antennas on the FPSA chip. A photo of the packaging is shown in Figure 4-12.

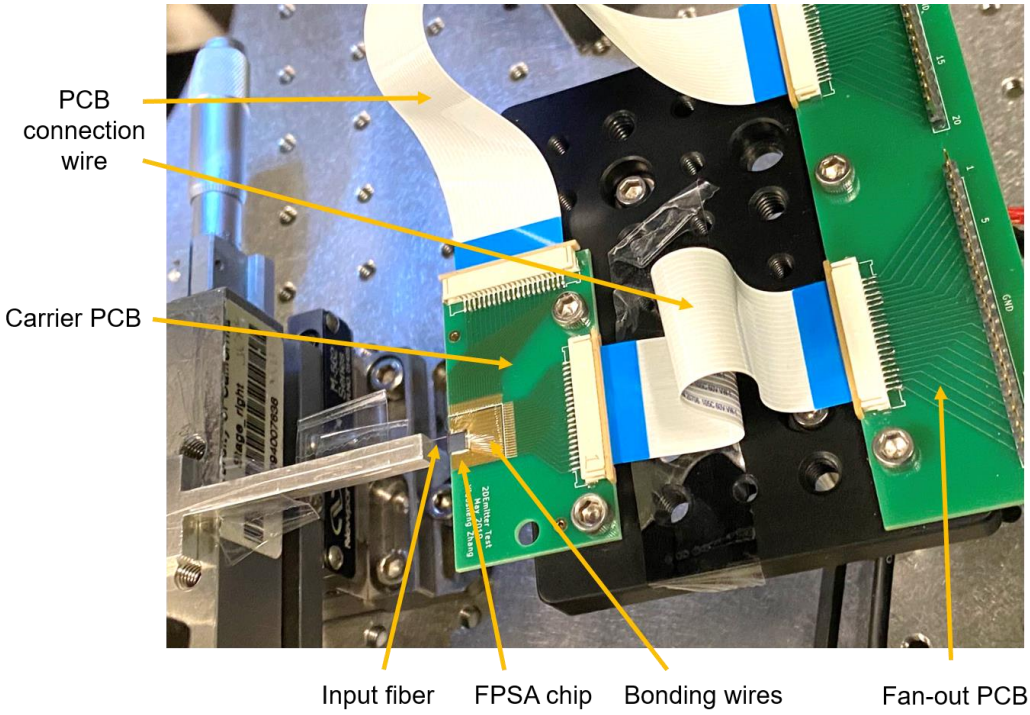

Figure 4-12. Photo of 20×20 FPSA electrical packaging and optical coupling.

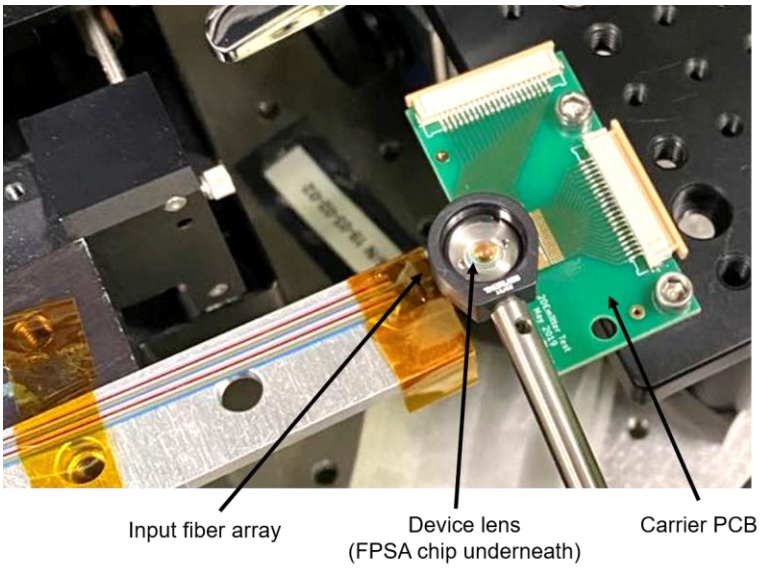

Figure 4-13. Photo of 20×20 FPSA with the device lens.

The f = 4.51 mm device lens is mounted on a lens holder and positioned by a translational stage on top of the FPSA array, shown in Figure 4-13. This setup can be easily tuned and reconfigured during experiments but may have a low alignment precision. A permanent packaging with high alignment precision can be achieved by attaching the coupling fiber to the FPSA chip and designing a customized mechanical mount holding the FPSA chip and the device lens.

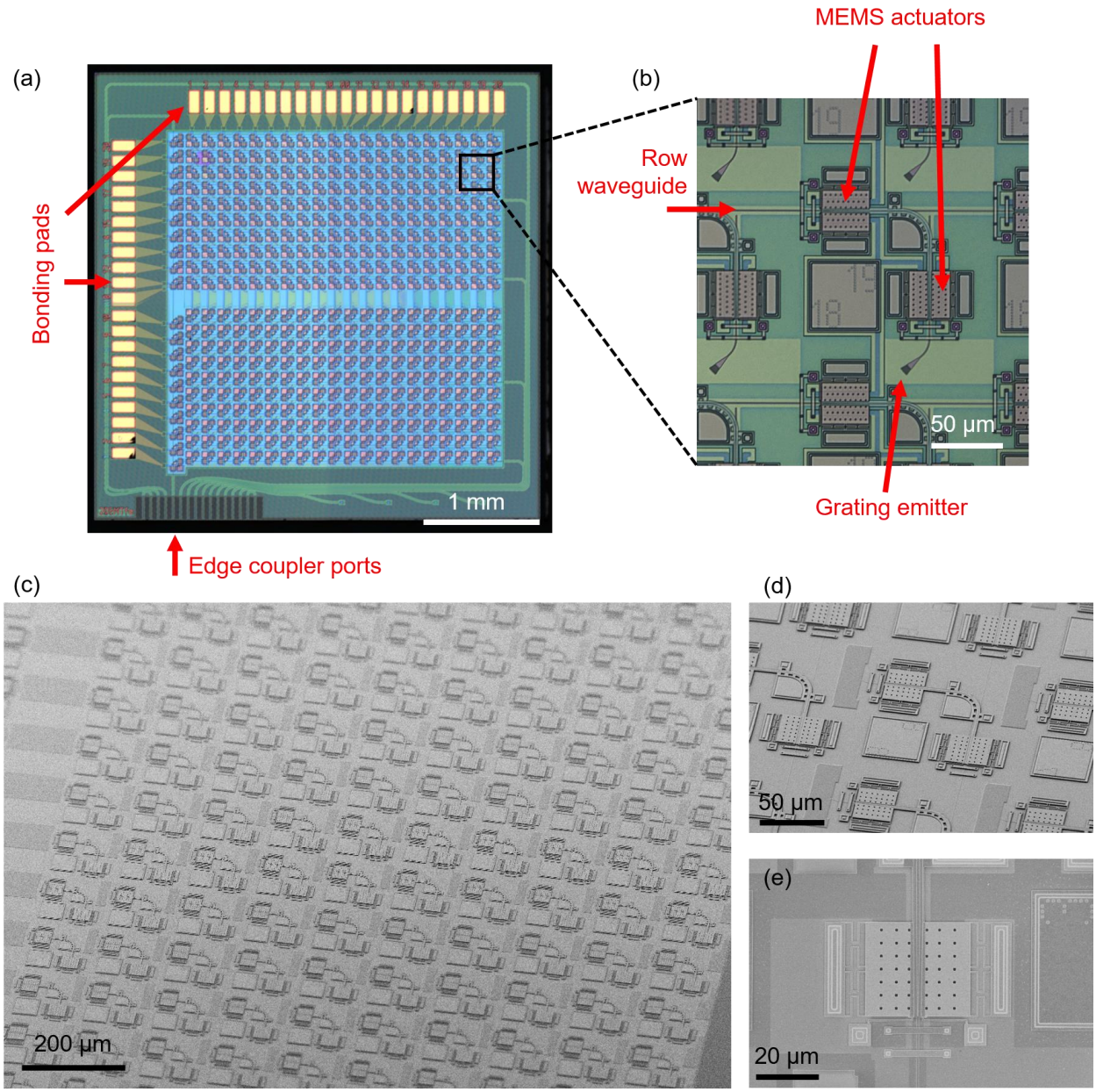

Figure 4-14. Microscopic images of the 20×20 FPSA.

(a) and (b) Microscopic images of the FPSA chip and one unit cell of a grating antenna with MEMS optical switch. (c), (d), and (e) SEM images of the FPSA chip, one unit cell, and MEMS actuator.

4.2.5 Microscopic images

Some optical microscope and SEM images of the fabricated 20×20 FPSA chip are shown in Figure 4-14. Figure 4-14(a) and (b) show optical microscopic images of the entire FPSA chip as well as a zoom-in view of a unit cell of a grating antenna with a MEMS optical switch. The FPSA chip has a 3.8×3.8 mm^2 size, and the active grating antenna aperture is 2.57×2.57 mm^2 with an array pitch of 135 μm in both directions. Wire-bonding pads, input edge couplers, and some test structures are located on the edges of the chip. Figure 4-14(c), (d), and (e) show SEM images of the FPSA chip, one unit cell of a grating antenna with MEMS optical switch, and a MEMS actuator, respectively.

4.2.6 Electrical characteristics

The transfer curve and response time measurement results of the MEMS optical switches in the 20×20 FPSA are shown in Figure 4-15(a) and (b) respectively. The transfer curve measures the optical power at the drop port of the MEMS switch as a function of the applied actuation voltage. The results show that the switch turns on at 32 V and turns off at 29 V. The hysteresis behavior is due to the pull-in effect of the electrostatic parallel-plate MEMS actuator. The response time curve measures the optical power at the drop port (blue curve) as a function of time when a square wave voltage waveform (black curve) is applied to the switch. The measurements show that the optical signal turns on or off within 1 μs of the electrical signal, therefore the FPSA device can work at a speed higher than 1 MHz for optical beam steering, which is suitable for LiDAR applications.

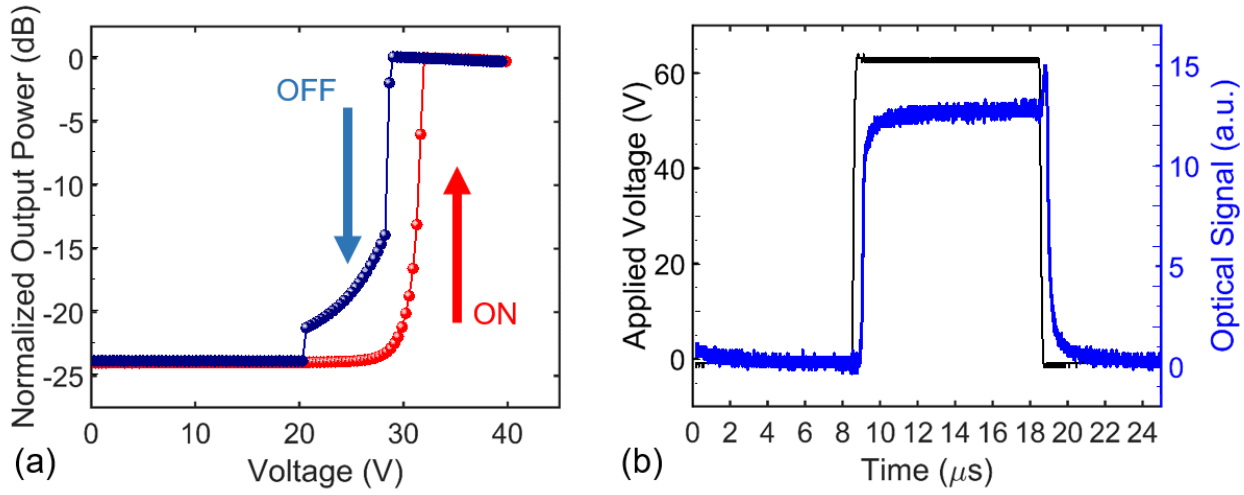

Figure 4-15. Electrical characteristics of the 20×20 FPSA.

(a) Transfer curve and (b) response time measurement results of the MEMS optical switch.

4.2.7 Optical characteristics

The far-field beam steering characteristics of the 20×20 FPSA beam scanner are measured by the optical setup shown in Figure 4-16(a). The output beam from the device lens is captured by a Fourier lens with a 30 mm focal length. An IR camera sensor (Xenics Bobcat-320) is placed

at the focal plane of the Fourier lens capturing the far-field intensity distribution of the FPSA beam scanner. The inset in the figure shows an image captured by the IR camera showing a beam spot. Due to the limited sensor size, the IR camera is put on a translational stage to capture the entire FoV.

The 400 grating antennas in the FPSA are turned on in sequence, and the captured far-field images are overlapped to demonstrate the beam steering pattern, shown in Figure 4-16(b). The image shows that the output beam is steered to distinct angles as expected. One row of beam spots is missing due to a broken bonding wire. The asymmetric distortion is due to a misalignment of the device lens and the FPSA chip. A mechanical package holding both the FPSA chip and the lens can provide better optical alignment and reduce this distortion.

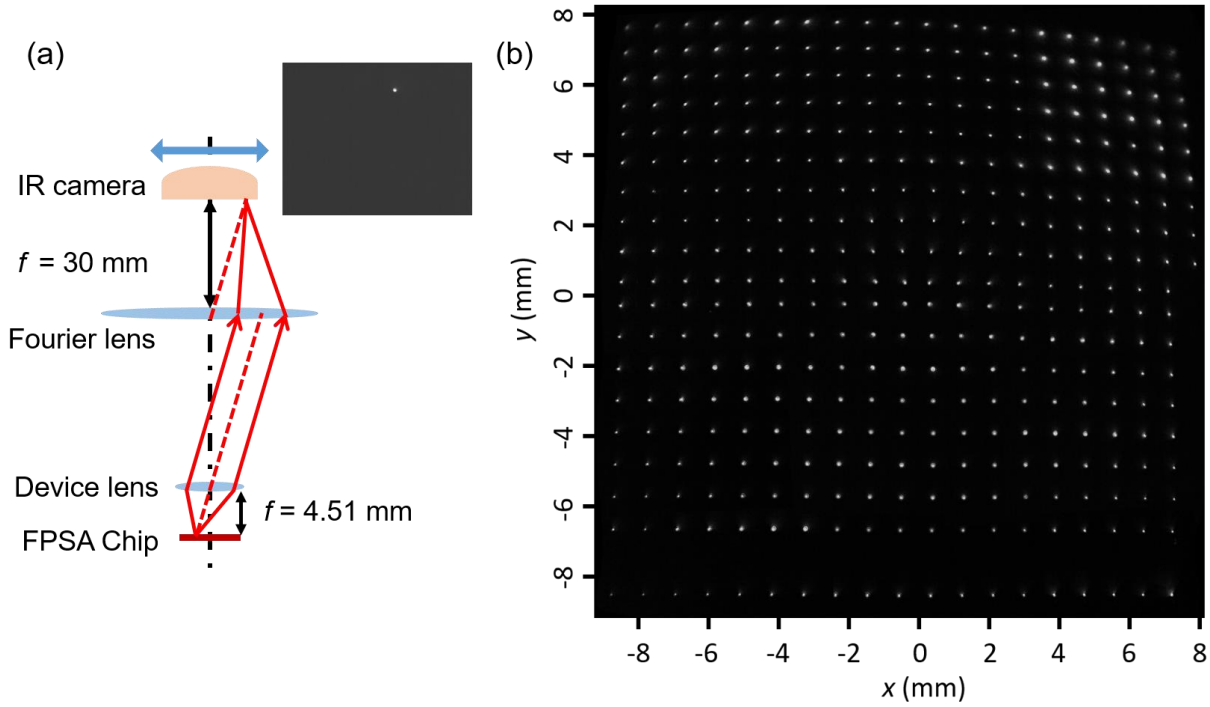

Figure 4-16. Far-field beam steering pattern of the 20×20 FPSA.

(a) Optical characterization setup. Inset shows an example of the far-field image captured by the IR camera. (b) Overlapped far-field beam steering pattern.

Figure 4-17(a) shows the divergence angle measurement results of four beam spots at different steering angles. The angles are measured at the FWHM of the intensity profile along the *x* and *y* directions. The theoretical divergence angle is 0.064° according to Equation (4-19). The measurement results roughly match the theoretical prediction, where the slightly larger results are due to the limited IR camera resolution and lens aberrations.

The output beam profile is also directly measured after a free-space propagation of 1.25 m distance from the device lens, without using the Fourier lens, shown in Figure 4-17(b). The measurement results show a symmetrical circular profile, and the main lobe of the beam has a half-maximum diameter of about 1.32 mm, which also matches the theoretical estimation.

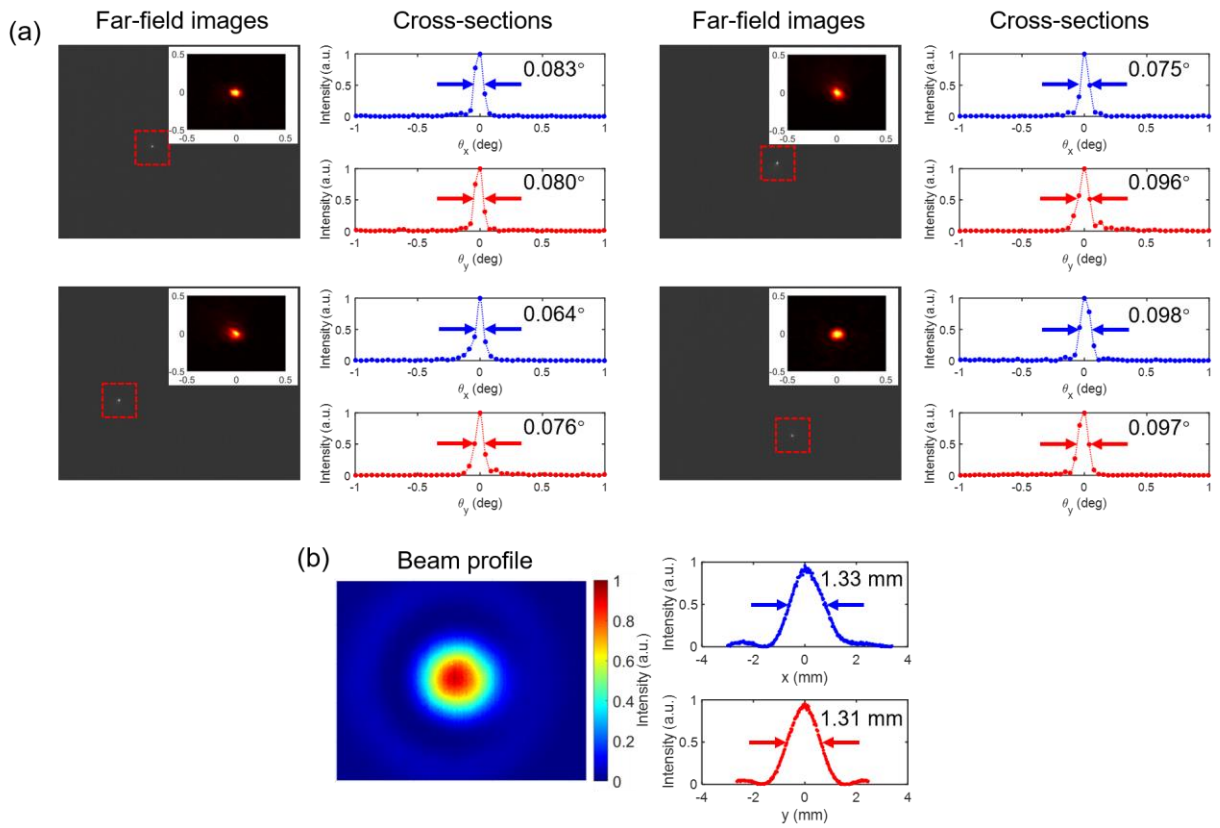

Figure 4-17. Divergence angle and beam profile measurement results of the 20×20 FPSA.

(a) Beam divergence angle measurements from the far-field images of four steering angles. The insets show zoomed-in profiles of the spots. (b) Output beam profile after 1.25 m free-space propagation. The Fourier lens is not used in this measurement.

4.2.8 Summary of device specifications

The specifications of the 20×20 FPSA beam scanner are summarized in Table 4-3.

Table 4-3. Specifications of the 20×20 FPSA beam scanner.

Mechanical and electrical specifications		Optical specifications	
Element number	400 (20×20)	Device lens focal length	4.51 mm
Array pitch	135 μm	FoV	32°×32°
Aperture size	2.57 × 2.57 mm^2	Resolution	1.7°×1.7°
Actuation voltage	30 V	Divergence	0.064°×0.064°
Response time	< 1 μs	Operating wavelength	1550 nm
Packaging	Wire-bond to PCB	Grating antenna efficiency	> 40%
		Input/output coupling	Edge coupler

4.3 Design and characterization of a 128×128 FPSA

4.3.1 Design overview

In this section, we will introduce the design of the large-scale 128×128-element silicon photonics FPSA with MEMS optical switches. The top-view and perspective schematics of the 128×128 FPSA beam scanner are shown in Figure 4-18, using a 4×4 array as an example. The design and operating principle are similar to the 20×20 FPSA reported in the section 4.2.1. Here we only summarize the important design improvements in scaling up the FPSA.

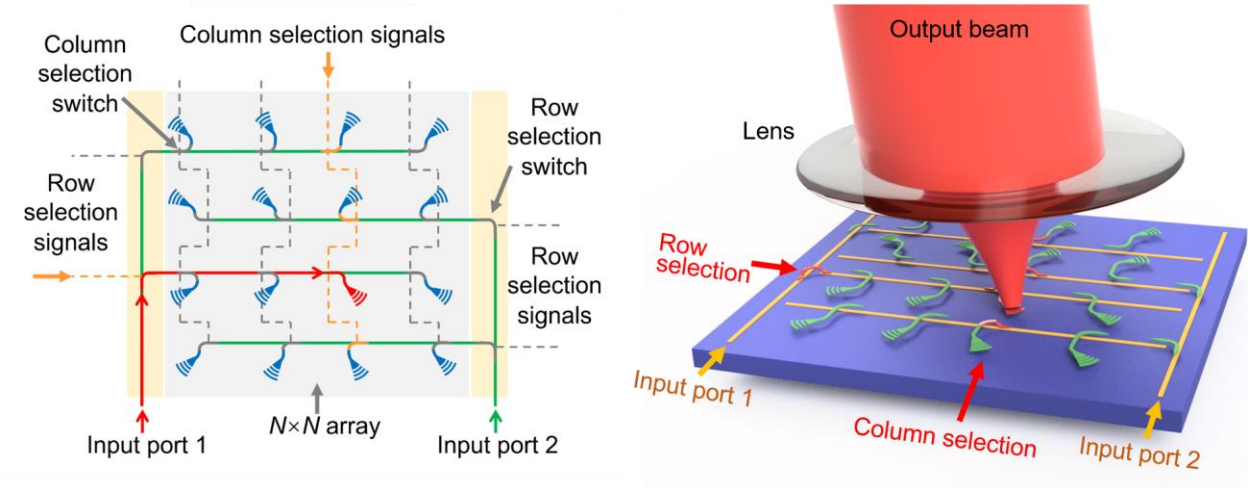

Figure 4-18. Schematics of the 128×128 FPSA beam scanner.

The grating antennas are placed on the polysilicon layer, therefore only one MEMS actuator is needed to couple light from the row waveguides to the grating antenna, significantly reducing the footprint of each unit cell of grating antenna and MEMS optical switch thus reducing the array pitch to l = 55 μm. The overall array size is L = 7 mm in both directions. Each row selection switch still has two MEMS actuators. Due to the footprint difference between the row and column selection switches, two input waveguides are designed on two sides of the array that alternatively connects to the row waveguides via row selection switches. Grating couplers are used for optical input/output coupling from external sources for a simpler fabrication and alignment process.

A compound lens with a focal length f = 5 mm is selected for the FPSA beam scanner for lower aberrations and higher beam quality. The grating antenna has a focusing-curved shape with a smaller size of 10 μm × 5.2 μm, and the size of the emission region (W) is about 4.4 μm. According to Table 4-1, the beam steering FoV, resolution, and divergence are

$$\mathrm{FoV} = 2\arctan\left(\frac{L}{2f}\right) = 2\arctan\left(\frac{7}{2\times 5}\right) = 70^{\circ}, \tag{4-20}$$

$$\mathrm{Resolution} = \frac{l}{f} = \frac{0.055}{5} = 0.6^{\circ}, \tag{4-21}$$

$$\text{Divergence} = \frac{W}{f} = \frac{4.4\times10^{-3}}{5} = 0.05^{\circ}. \tag{4-22}$$

4.3.2 Grating antenna design

The grating antennas in the 128×128 FPSA are defined on the polysilicon layer by a partial etch, and both the top and the bottom sides of the gratings are air-clad. The gratings have a focusing-curved shape with a size of 10 μm × 5.2 μm, and the size of the emission region (*W*) is about 4.4 μm, shown in Figure 4-19 top. The grating groove width is designed to be a constant 290 nm regardless of the grating period for a better etching uniformity throughout the array.

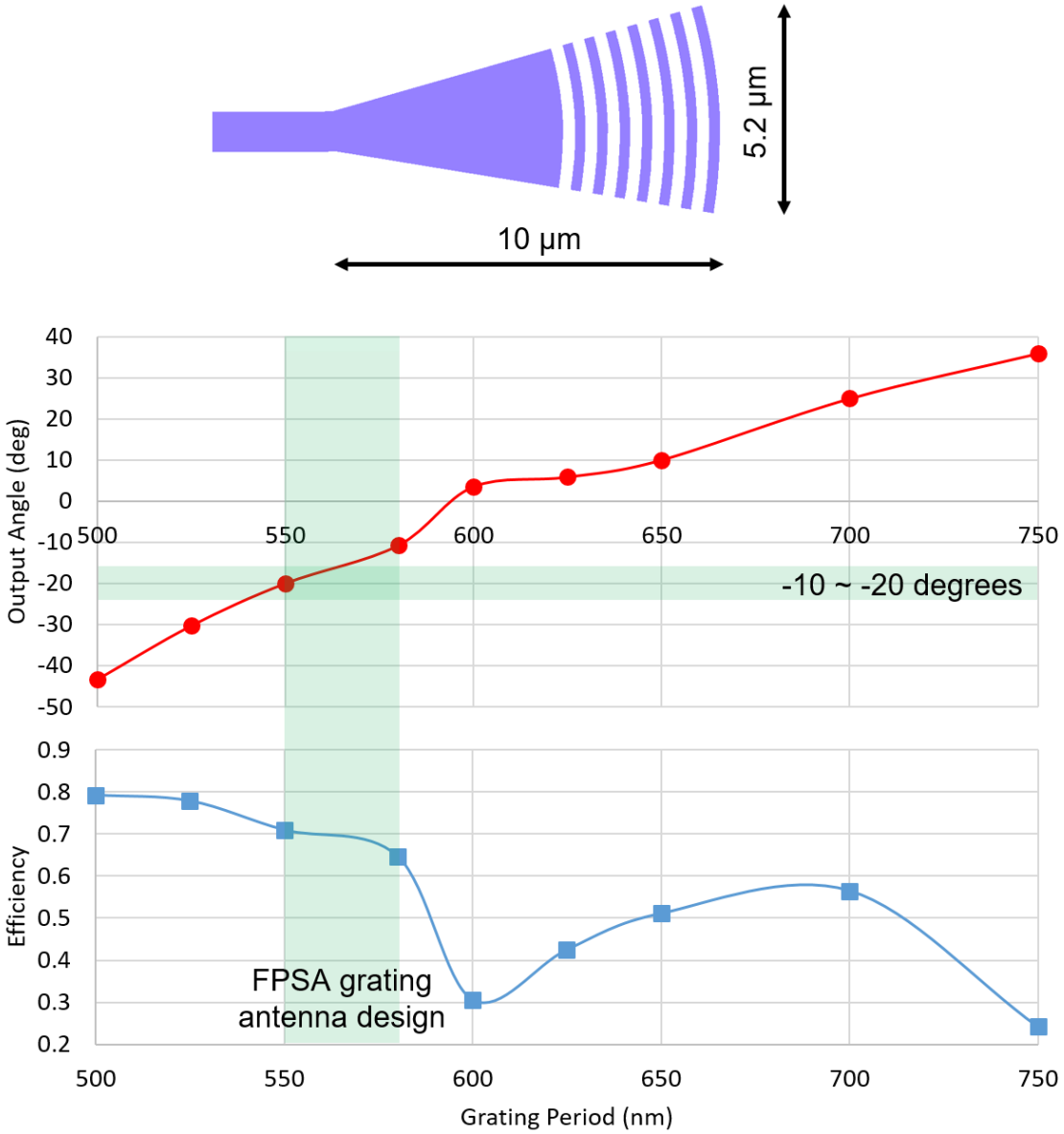

Figure 4-19. 128×128 FPSA grating antenna design and simulation results.

Similar to the 20×20 FPSA, the grating periods are designed based on the grating antenna locations such that the center of the emitted light is directed towards the center of the device lens. The grating antenna central emission angle and efficiency as a function of the grating period are simulated using the FDTD method shown in Figure 4-19 bottom. The negative emission angles are selected for a higher optical efficiency. The output angles are set to be limited in the region of -10° to -20° to ensure an optical efficiency higher than 65%.

4.3.3 Fabrication, packaging, and control

The 128×128 FPSA device is fabricated on a 220 nm SOI wafer with a standard silicon photonics process and an additional polysilicon layer for grating antennas, coupler waveguides, and MEMS actuators. The fabrication process flow is shown in Figure 4-20. (1) The fabrication process flow starts with an SOI wafer. (2) The device layer of the SOI wafer is patterned for waveguides and input/output grating couplers. Electrical interconnects are doped by ion implantation. (3) Trenches for electrical isolation between interconnects are etched and filled with aluminum oxide. (4) Sacrificial oxide is deposited. (5) The oxide layer is etched for polysilicon anchors and dimples. The polysilicon layer is deposited and patterned to define the grating antennas, coupler waveguides, and MEMS actuators. (6) The MEMS structures are released.

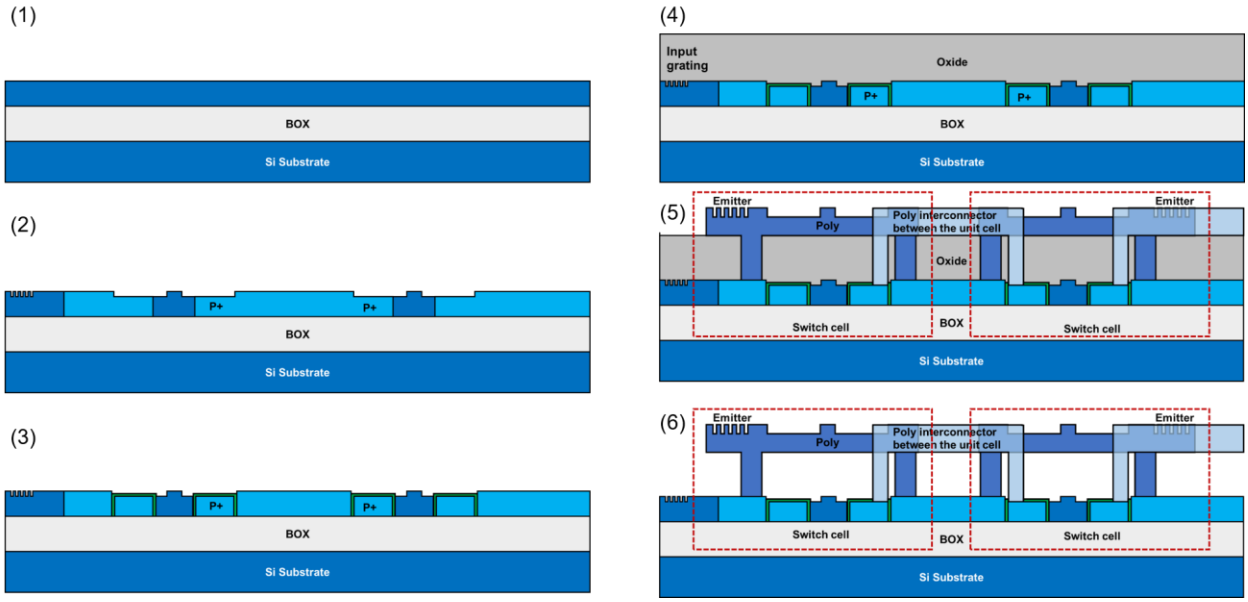

Figure 4-20. 128×128 FPSA fabrication process flow.

The fabricated FPSA chip is attached and wire bonded to a 256-pin ceramic pin grid array (PGA). Due to the limited available space and pin count of the PGA, only three quarters of the rows selection signals are wire bonded, with one signal in every four rows skipped. All column selection signals are wire bonded to the PGA. Therefore, 128×96 elements in the array are electrically addressed.

The PGA is connected to a carrier PCB, which is then connected to a high voltage controller PCB. The high voltage controller PCB has a DC voltage converter to convert the 5 V power

supply to the high drive voltage for the MEMS actuators, routed to 256 PGA pins by two 128-channel low-voltage serial to high-voltage parallel converters (HV583). Each HV583 converter is composed of four 32-bit shift registers to convert serial input data into parallel digital output voltages. The HV583 converter has a maximum clock rate of 40 MHz, so the 32-bit shift registers can be fully refreshed at a rate up to 1.25 MHz.

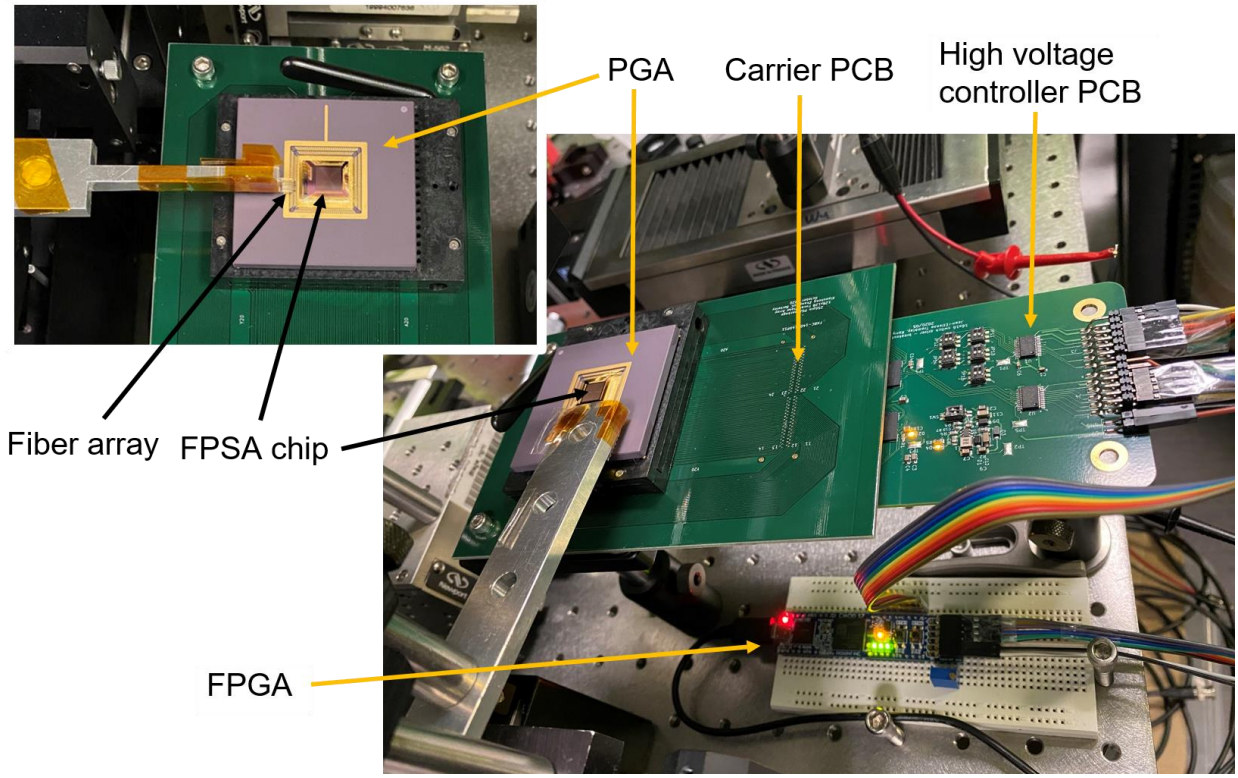

Figure 4-21. Photos of 128×128 FPSA electrical packaging and optical coupling.

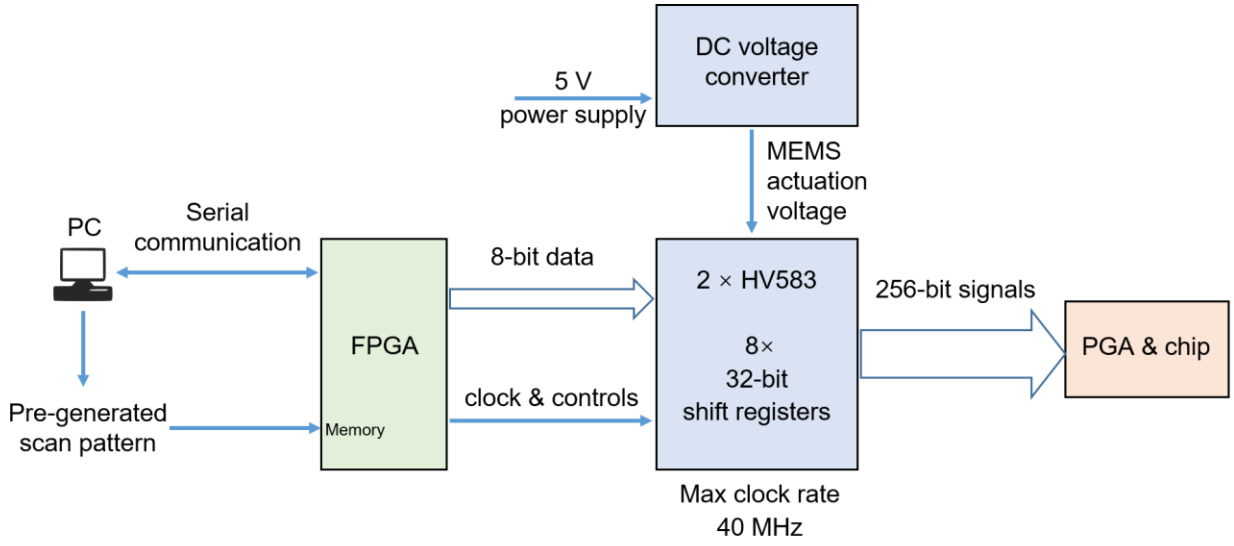

Figure 4-22. Block diagram of 128×128 FPSA beam scanner control.

The high voltage controller PCB is connected to a field-programmable gate array (FPGA) board (Digilent cmod-S7) to control the beam steering of the FPSA beam scanner. The scan pattern can be written to the FPGA from a personal computer (PC) via serial communications, or it can be pre-generated and stored in the read-only memory on the FPGA to avoid the relatively slow serial communication. Optical signals are coupled on/off the FPSA chip via an off-chip fiber array and on-chip grating couplers. Photos of the FPSA chip packaging and a control diagram are shown in Figure 4-21 and Figure 4-22.

4.3.4 Compound lens analyses

The device lens is an important component in the FPSA beam scanner. A device lens that can collect all the emitted light from the antennas with high transmittance and low aberrations is desired.

For a single piece of convex lens with a proper anti-reflection coating, the transmittance can be higher than 90%. A singlet lens also has a small size and a well-defined aperture stop, therefore the antennas should be designed to emit towards the physical lens center. However, a singlet lens typically has large aberrations, especially for the ones with a small focal length. A singlet lens design with an aspherical surface shape can help reduce aberrations like the spherical aberration for on-axis spots, but the off-axis spots can still have large aberrations.

Compound lenses with multiple pieces of glass can be optimized to have low aberrations for both on-axis and off-axis spots, thus are widely used in practical optical systems such as cameras, telescopes, and microscope objectives. Since the FPSA beam scanner works like an inverse camera, compound lenses designed for cameras are also compatible with FPSA beam scanners, which ensure high output beam quality. The large library of camera lens including compact cellphone camera lens designs makes the FPSA beam scanner design highly flexible to meet the various requirements on FoV, resolution, and beam divergence for different applications.

The compound lens specifications that are typically provided by the manufacturer include the focal length, F-number, sensor format, FoV, and lens mount. The definitions of these values may not be as straightforward as for a singlet lens. Figure 4-23 shows an example layout of a compound lens with the principal planes and pupils. Note that for an ideal singlet lens the front and back principal planes are both at the same plane as the lens, and the entrance pupil, exit pupil, and aperture stop are all the same as the physical lens aperture. The back focal length f is the distance between the back principal plane and the back focal plane. The FPSA chip should be placed on the back focal plane of the lens, however, the back principal plane is a virtual reference plane that is typically not located at the last piece of lens in the compound lens set. Therefore, the distance between the lens and the FPSA chip for optical alignments should not be simply determined by the focal length.

The sensor format and FoV of a lens describe the maximum sensor size it supports and the corresponding imaging FoV, which provides information related to the size of the field stop. The FPSA chip should not be larger than the designed sensor format of the lens, otherwise the edge antenna emission may not be well captured by the lens.

The F-number of a lens is defined as the ratio between the focal length and the entrance pupil diameter, and it is an important parameter to measure the aperture size of the lens. The physical diaphragm inside the lens is the aperture stop. The image of the aperture stop through

the set of lenses before the aperture stop is the entrance pupil, and the image of the aperture stop through the set of lenses after the aperture stop is the exit pupil. From Figure 4-23 it can be seen that the aperture stop, entrance pupil, and exit pupil of a compound lens are usually not at the same location and do not have an equal size. Note that here the entrance and exit directions are defined by the regular direction of use for a camera lens. In an FPSA beam scanner, the light emitted from the antennas is first captured by the exit pupil of the lens, therefore the antennas should be designed to emit towards the center of the exit pupil, instead of the center of the last piece of lens or the center of the physical aperture stop. However, the location and size of the exit pupil are usually not provided in the lens specifications. In addition, for a compound lens with aspherical pieces, the effective exit pupil for off-axis spots can be significantly different from the exit pupil defined for the on-axis spots. Therefore, ray-tracing simulation or experiments should be performed to determine the exit pupil parameters to assist the antenna design.

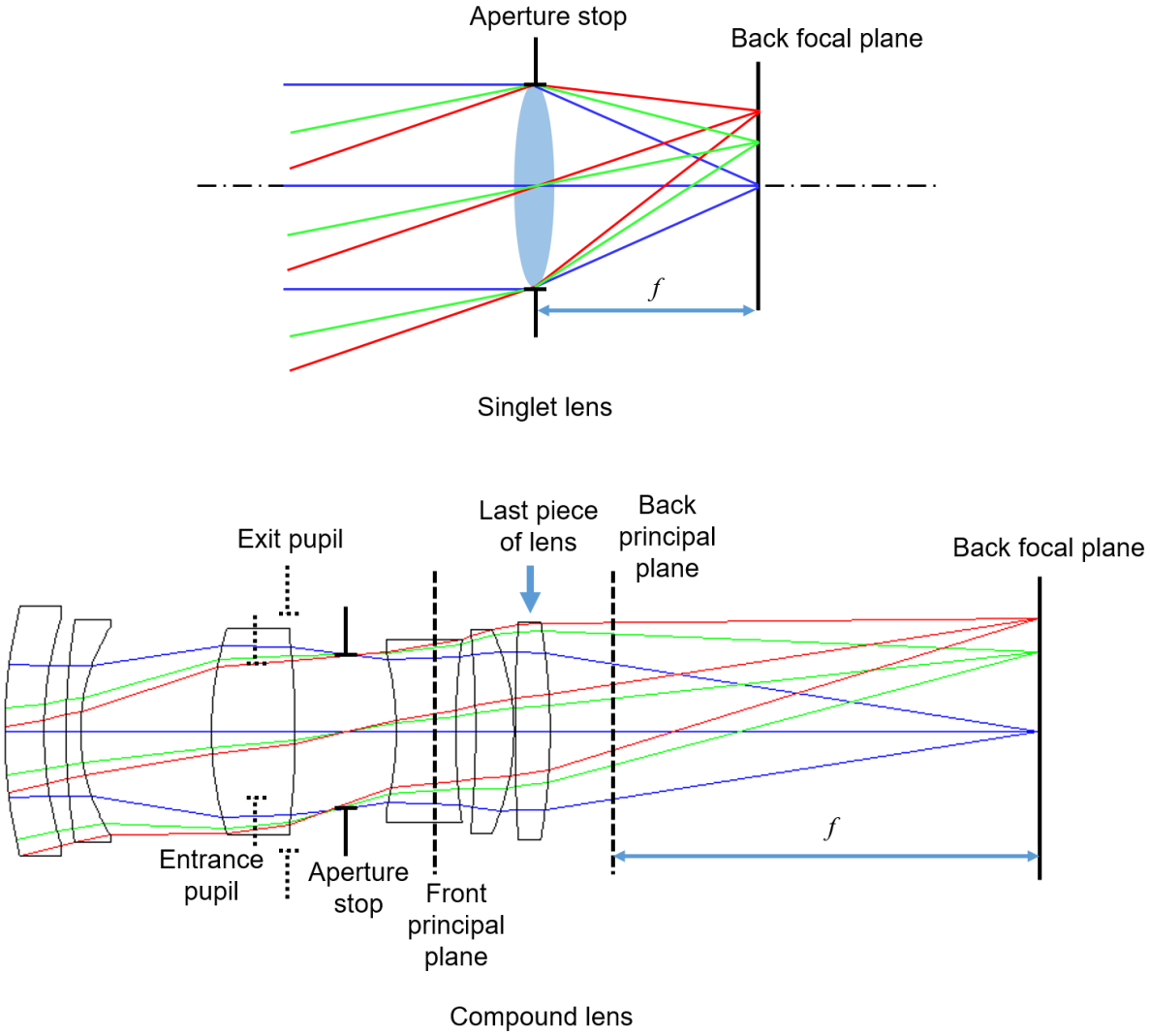

Figure 4-23. Layouts of a singlet lens and a compound lens.

4.3.5 Microscopic images

Some optical microscope and SEM images of the fabricated 128×128 FPSA chip are shown in Figure 4-24. Figure 4-24(a) shows an optical microscopic image of the entire FPSA chip. The dashed box indicates the active grating antenna array. Figure 4-24(b) and (c) show optical microscopic images of zoom-in views of grating antennas, column selection switch with one MEMS actuator, and row selection switch with two MEMS actuators. The FPSA chip has an 11×10 mm^2 size, and the active grating antenna aperture is 7×7 mm^2 with an array pitch of 55 μm in both directions. Wire-bonding pads and input/output grating couplers are located on the edges of the chip. Figure 4-24(c), (d), and (e) show SEM images of the FPSA chip, one unit cell of a grating antenna with the column selection switch, and a grating antenna, respectively.

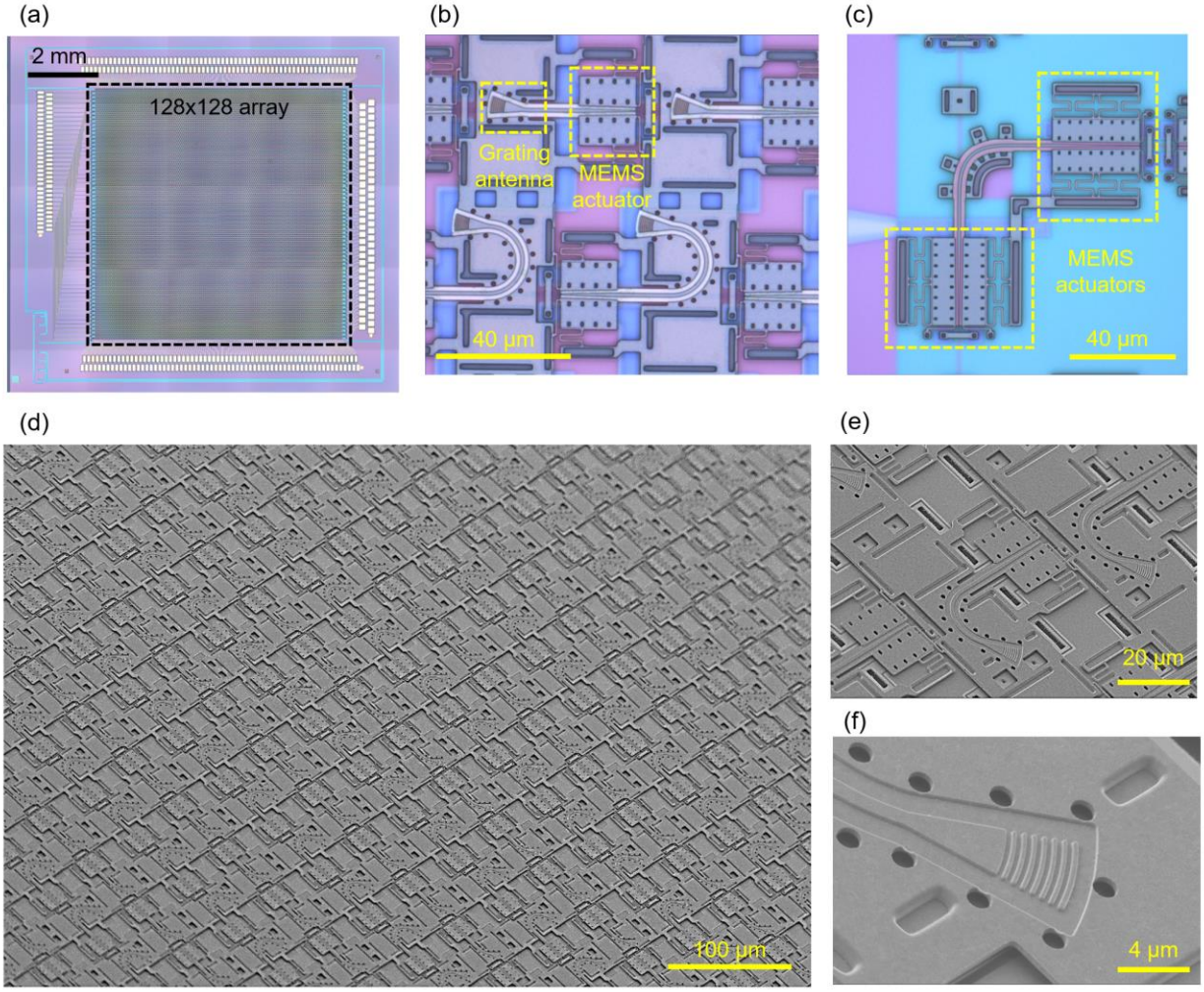

Figure 4-24. Microscopic images of the 128×128 FPSA.

(a), (b), and (c) Microscopic images of the FPSA chip, a zoom-in view of grating antennas with column selection switches, and a zoom-in view of a row selection switch. (d), (e), and (f) SEM images of the FPSA chip, one unit cell, and the grating antenna.

4.3.6 Electrical characteristics

The switch responses under a square wave voltage waveform actuation are characterized by measuring the optical power as a function of time, shown in Figure 4-25. The optical power is measured at the through port of the row selection switches (average of 22 measurements) and the drop port of the column selection switches (average of 32 measurements). The measured response time of the row selection switch is about 1 μs, similar to the results of the 20×20 FPSA. The measured ON and OFF response times of the column selection switch are 2.7 μs and 2.0 μs respectively, which are slightly slower than the row selection switches due to the more compact MEMS actuator design. This fast response enables optical beam steering at sub-MHz speed.

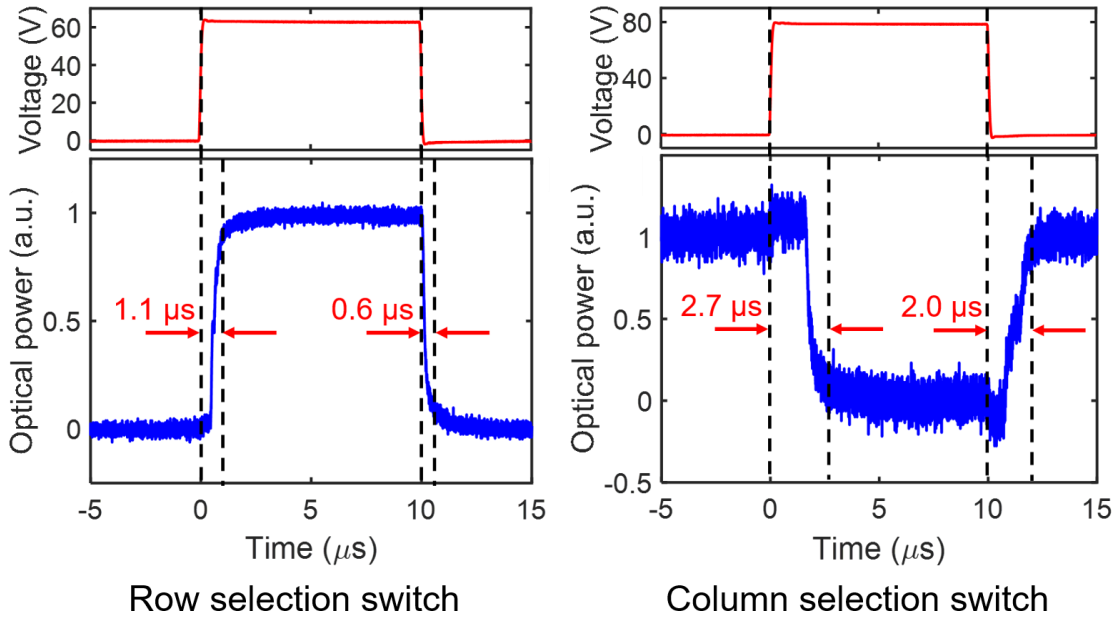

Figure 4-25. Response time measurement results of the row and column selection switches.

4.3.7 Optical characteristics

The far-field beam steering pattern of the 128×128 FPSA beam scanner is measured by the optical setup shown in Figure 4-26(a). The output beam from the device lens is projected onto a paper as a diffusion screen. An IR camera with a 3.5 mm wide-angle lens is placed on the back side of the paper screen to image the beam steering pattern. The 128×96 electrically addressed grating antennas in the FPSA are turned on in sequence, and the captured far-field images are overlapped to demonstrate the beam steering pattern, shown in Figure 4-26(b). The image shows that the output beam is steered to distinct angles as expected despite some minor defects in the fabricated device. The FoV distortion is due to the wide-angle lens used for the IR camera. To demonstrate the random access capability of the beam steering, the FPSA beam scanner is controlled to steer the beam in a “Cal” logo pattern, and the overlapped far-field image is shown in Figure 4-26(c).

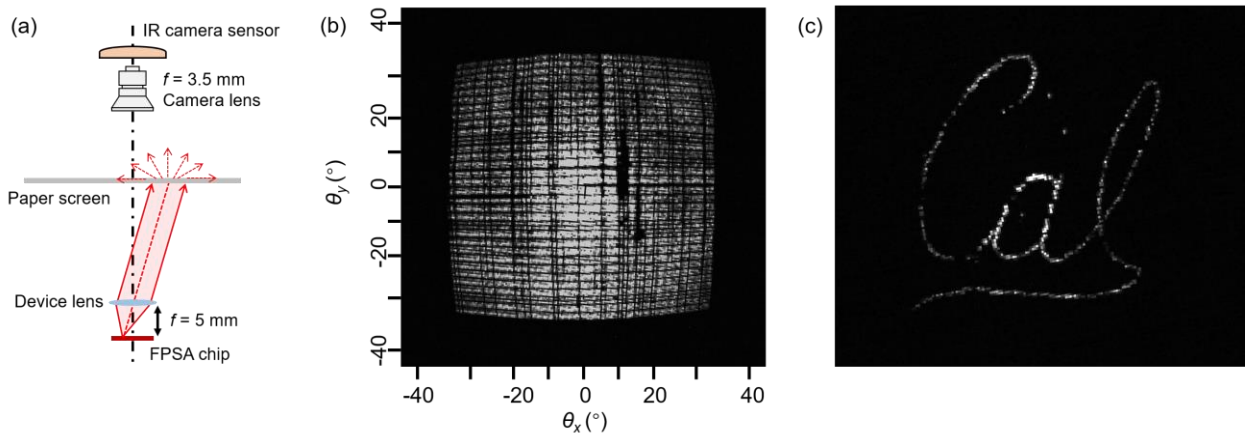

Figure 4-26. Far-field beam steering pattern of the 128×128 FPSA.

(a) Optical measurement setup. (b) Overlapped far-field beam steering pattern. (c) A "Cal" logo pattern generated by the FPSA beam scanner.

Detailed beam steering pattern in a part of the FoV is captured by a Fourier lens with a 30 mm focal length placed after the device lens. The IR camera sensor with a 33 fps frame rate is placed at the focal plane of the Fourier lens capturing the far-field intensity distribution of the FPSA beam scanner, shown in Figure 4-27(a). The output beam is scanned at a 100 kHz rate, and one frame of the IR camera image is shown in Figure 4-27(b). The non-uniform distribution of beam spots is due to the skipped rows in wire bonding and the intentionally rotated grating antenna orientations.

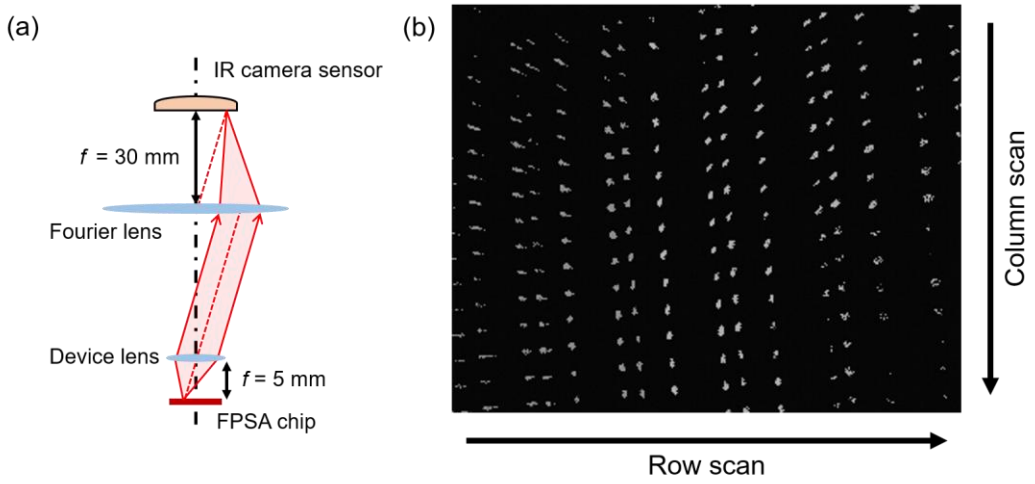

Figure 4-27. Far-field beam steering pattern of the 128×128 FPSA captured by a Fourier lens.

(a) Optical measurement setup. (b) Beam steering pattern in part of the FoV captured at the focal plane of a Fourier lens.

The beam divergence is measured by the IR camera sensor placed 0.71 m away from the FPSA beam scanner, shown in Figure 4-28(a). The measured beam intensity profile and the cross-sectional profiles along the *x* and *y* directions are shown in Figure 4-28(b) and (c)

respectively. The measured FWHM beam divergence is 0.050°×0.049°, which agrees with the theoretical value in Equation (4-22).

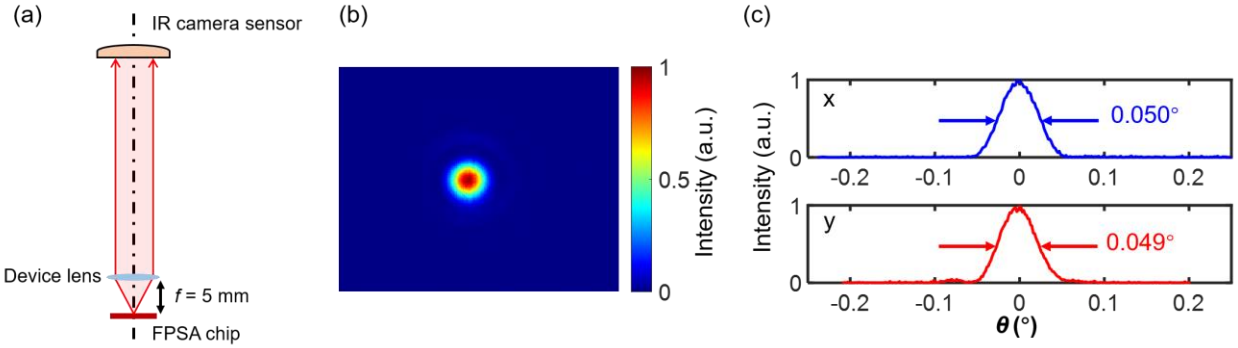

Figure 4-28. Beam profile and divergence measurement results of the 128×128 FPSA.

(a) Optical measurement setup. (b) and (c) Beam intensity profile and cross-sections captured after 0.71 m free-space propagation.

4.3.8 Optical efficiency

The optical losses in the FPSA beam scanner can be classified into coupling losses and on-chip losses. The coupling losses include the fiber array to chip coupling loss, the chip to free-space coupling loss from the grating antenna, and the antenna emission to far-field coupling loss from the device lens.

(1) The fiber array to on-chip grating coupler coupling loss of our device is measured to be 5 dB, which agrees with the FDTD simulation results. In practice, this loss can be reduced by applying index matching gel between the fiber array and the grating couplers. Other coupling mechanisms such as the evanescent wave coupling can help further reduce the fiber to chip coupling loss [62].

(2) The grating antenna efficiency varies depending on the antenna location on the array, as shown in Figure 4-19. The minimum grating antenna efficiency is 65%, therefore we use 65% = -1.9 dB antenna loss in the beam scanner optical efficiency estimation. The grating antenna efficiency can be improved by optimizing the geometry of the grating design.

(3) The efficiency of the device lens includes the collection efficiency of the emitted light from the antenna and the transmittance of the lens. The overall lens efficiency is about 50% for our device according to measurement results and optical simulations. The lens transmittance can be increased by anti-reflection coatings on the glass surfaces. Matching the lens exit pupil with the antenna emission profile will also improve the overall lens efficiency.

The on-chip losses are composed of the waveguide propagation loss and the optical switch losses.

(1) The silicon waveguide propagation loss on the chip under test is measured to be 3.8 dB/cm. This high propagation loss is due to some residues left on the waveguide during the fabrication process. We estimate the propagation loss can be reduced to lower than 1 dB/cm with an improved fabrication process, and have verified this low propagation loss on a testing chip. The waveguide length from the input couplers to the antenna varies depending on the antenna

location. For a grating in the central area of the FPSA, the waveguide length is about 2 cm from the farther input port. We use this length in the beam scanner optical efficiency estimation.

(2) The losses of the row selection switch and column selection switch on the chip under test are measured to be 2 dB and 2.5 dB respectively. With an improved fabrication process on a testing chip, we have verified that 1 dB switch loss can be achieved for both types of optical switches.

The optical losses from all the components mentioned above on the FPSA chip under test, as well as on a testing chip with an improved fabrication process, are summarized in Table 4-4. The total optical losses for the chip under test is 22 dB, and with an improved fabrication process the loss can be immediately reduced to 13.9 dB. With an optimized coupling mechanism, grating antenna efficiency, and device lens efficiency, we believe the optical efficiency of the FPSA beam scanner can be further improved.

Table 4-4. Summary of optical losses in the 128×128 FPSA beam scanner.

Loss component	Optical loss on the FPSA chip under test	Optical loss with improved fabrication
Fiber array coupling	5 dB	5 dB
Waveguide propagation	3.8 dB/cm * 2.0 cm = 7.6 dB	1 dB/cm * 2.0 cm = 2 dB
Row selection switch	2 dB	1 dB
Column selection switch	2.5 dB	1 dB
Antenna loss (efficiency)	1.9 dB (65%)	1.9 dB (65%)
Device lens loss (efficiency)	3 dB (50%)	3 dB (50%)
Total	22 dB	13.9 dB

4.3.9 Summary of device specifications

The specifications of the 128×128 FPSA beam scanner and their comparison with the 20×20 FPSA beam scanner are summarized in Table 4-5.

Compared with the 20×20 FPSA, the large-scale 128×128 FPSA employs a more compact grating antenna and MEMS optical switch design, reducing the array pitch from 135 μm to 55 μm. The overall array size is increased from 2.57 mm to 7 mm. These improved parameters lead to a larger FoV, a higher resolution, and a lower beam divergence for optical beam steering. In addition, the efficiency of the grating antennas is improved, and the aberration effects are reduced thanks to the implementation of a compound camera lens.

The actuation speed of the column selection switch is slightly slower in the 128×128 FPSA due to the more compact MEMS actuator design. With an improvement on the MEMS actuator mechanical performance, we believe higher than MHz actuation speed can also be achieved in large-scale FPSAs.

Table 4-5. 128×128 FPSA beam scanner specifications and comparison with the 20×20 FPSA.

	128×128 FPSA	20×20 FPSA
Mechanical and electrical specifications		
Element number	16,384 (128×128)	400 (20×20)
Array pitch	55 μm	135 μm
Aperture size	7 × 7 mm^2	2.57 × 2.57 mm^2
Actuation voltage	50 V	30 V
Response time	2.7 μs	< 1 μs
Packaging	Wire-bond to PGA	Wire-bond to PCB
Optical specifications		
Device lens focal length	5 mm	4.51 mm
FoV	70°×70°	32°×32°
Resolution	0.6°×0.6°	1.7°×1.7°
Divergence	0.050°×0.050°	0.064°×0.064°
Operating wavelength	1550 nm	1550 nm
Grating antenna efficiency	> 65%	> 40%
Input/output coupling	Grating coupler	Edge coupler

4.4 FPSA beam scanner implementation on FMCW LiDAR

4.4.1 Experimental setup

In this section, we will combine the research works on the FMCW LiDAR and the FPSA beam scanner, and introduce the implementation of the 128×128 FPSA beam scanner on a monostatic FMCW LiDAR system for 3D imaging.

The experimental setup is shown in Figure 4-29. The commercial DFB laser (Optilab DFB-1550) is frequency modulated and the laser chirp is linearized by the iterative learning pre-distortion method described in Chapter 2. A small portion of the light after passing the isolator is tapped to the laser chirp linearization setup (the chirp linearization process is performed before the LiDAR measurements), while the major part is sent to an erbium-doped fiber amplifier (EDFA) where the optical power is amplified to compensate for the optical losses in the setup. After passing the fiber circulator, the light is split by a 50/50 splitter into two channels of the fiber array for the two input ports of the 128×128 FPSA chip. Light is then coupled into the FPSA chip and emitted to the object through the device lens. The optical beam steering is controlled by a PC and FPGA. The fiber array facet and on-chip grating coupler together have a reflection of about -34 dB. This reflected light is used as the reference light (local oscillator) for the FMCW LiDAR.

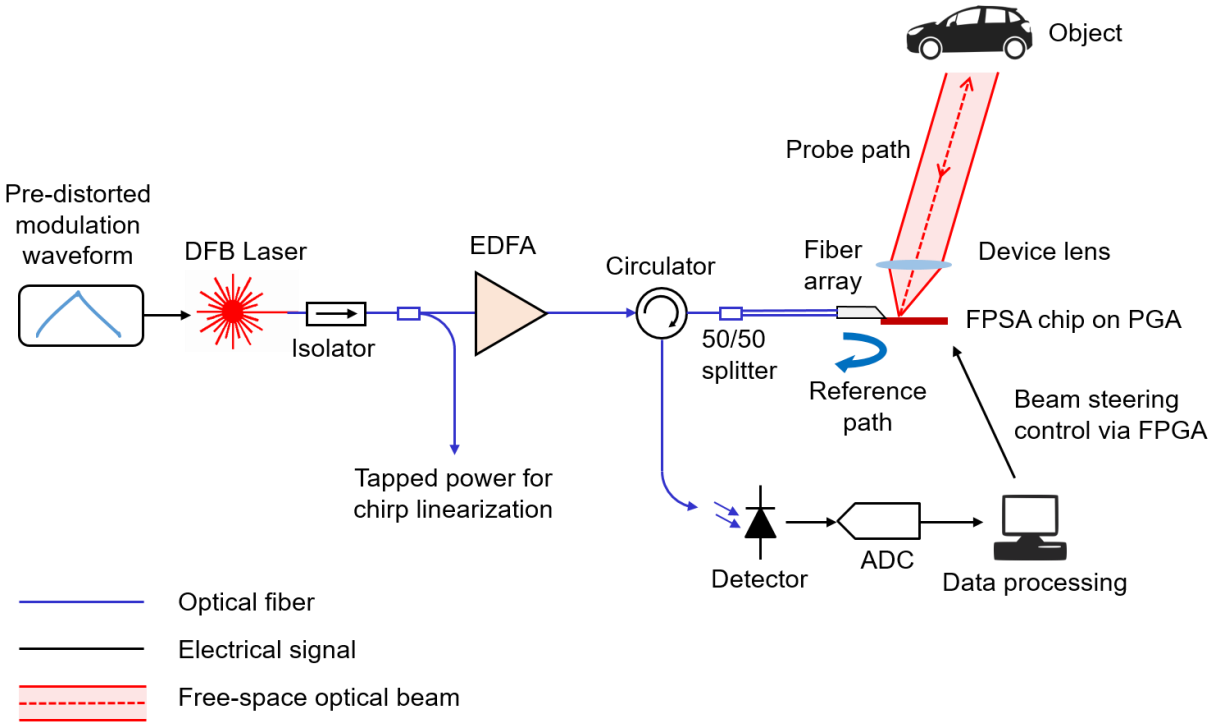

Figure 4-29. Setup of FPSA beam scanner implementation on FMCW LiDAR.

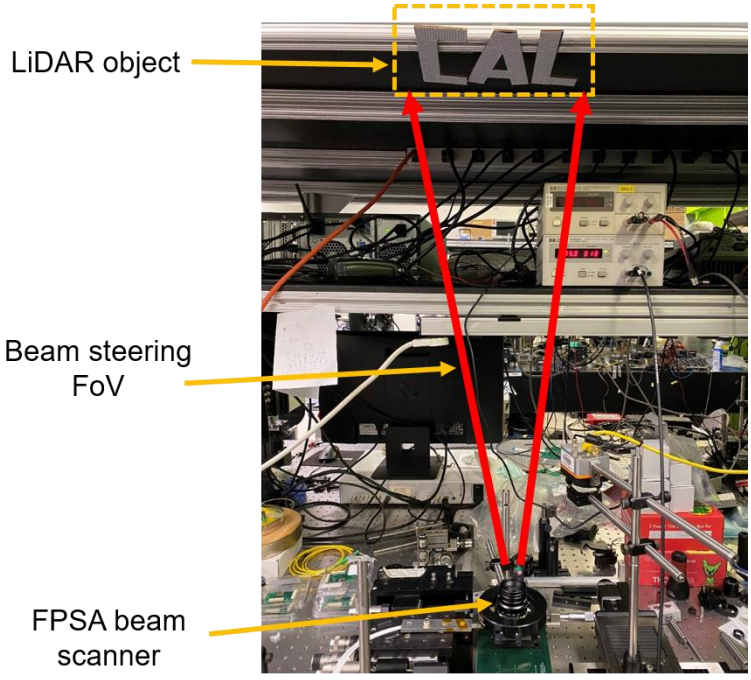

Figure 4-30. Photo of the FPSA beam scanner and the LiDAR object.

The returned probe path light from the object is received by the same FPSA beam scanner via the same grating antenna and is then coupled back to the fiber system through the fiber array.

The probe path and reference path light are sent to the photodetector through the fiber circulator. The beat signal is sampled by the ADC and sent to the PC for data processing.

The laser modulation by the pre-distorted waveform generated by an arbitrary waveform generator, the beat signal acquisition by the ADC, and the optical beam steering by the FPSA beam scanner are synchronized under the control of the PC.

The device lens on the FPSA beam scanner for the LiDAR experiments is a 25 mm focal length F/1.4 compound camera lens, which results in a beam steering FoV of 16°×16° and a resolution of 0.13°×0.13°. The optical power output from the FPSA beam scanner is approximately 1 mW. The laser frequency excursion is 8.6 GHz within an 80 μs chirp period, resulting in an FMCW LiDAR distance resolution of 1.7 cm. The object for the 3D imaging demonstration is composed of three letters "CAL" made of cardboard and coated with a reflective sheet that is typically used for traffic signs to increase the object reflectivity. The object is placed approximately 0.8 m away from the FPSA beam scanner. The setup photo is shown in Figure 4-30.

4.4.2 Reference path considerations

In an FMCW LiDAR, the reference path is an optical path with a fixed length acting as the local oscillator for coherent detection. A common architecture of FMCW LiDAR is an MZI in which one fixed interferometer arm is the reference path, as shown in Figure 4-31(a). Advantages of this architecture include that a pair of balanced photodetectors can be implemented to cancel out the DC component of the photocurrent to suppress the laser RIN, and the optical power and polarization state in the reference path can be independently controlled without affecting the probe path.

The interfaces between fiber and free space or silicon waveguide and free space can back reflect part of the transmitting light, especially when not anti-reflection coated or polished at an angle. For example, an FC/PC fiber connecter typically has a -30 dB ~ -40 dB back reflection. This reflection in the probe path will generate a false object peak in the FMCW LiDAR beat signal spectrum. Considering that the return from a real object in a LiDAR system may have a loss higher than -90 dB, the back reflection in the probe path may be significantly stronger than the real object signal. This strong false signal may cover up the real object signal, or even saturate the photodetector.

To mitigate the interface back reflection issue in a practical system, a strong back reflection in the probe path can be utilized as the reference path, as shown in Figure 4-31(b). We use this architecture in the LiDAR experiments reported in this chapter with the -34 dB reflection from the fiber array facet and the on-chip grating coupler surfaces. Next, we will analyze the impact on the FMCW LiDAR SNR when using this architecture.

According to section 2.4.1, the ASDs of the signal peak and the shot noise are

$$\sigma_{\text{signal}}\left(f_{\text{b}}\right)=G_{\text{TIA}}\sqrt{\frac{I_{\text{AC}}^{2}}{2}T\exp\left(-\frac{2\tau}{\tau_{\text{c}}}\right)}=G_{\text{TIA}}\sqrt{\frac{R^{2}P_{\text{ref}}P_{\text{rx}}}{2}T\exp\left(-\frac{2\tau}{\tau_{\text{c}}}\right)}, \tag{4-23}$$

$$\sigma_{\text{shot}}\left(f\right)=G_{\text{TIA}}\sqrt{2eI_{\text{DC}}}=G_{\text{TIA}}\sqrt{2eR\left(P_{\text{ref}}+P_{\text{rx}}\right)}. \tag{4-24}$$

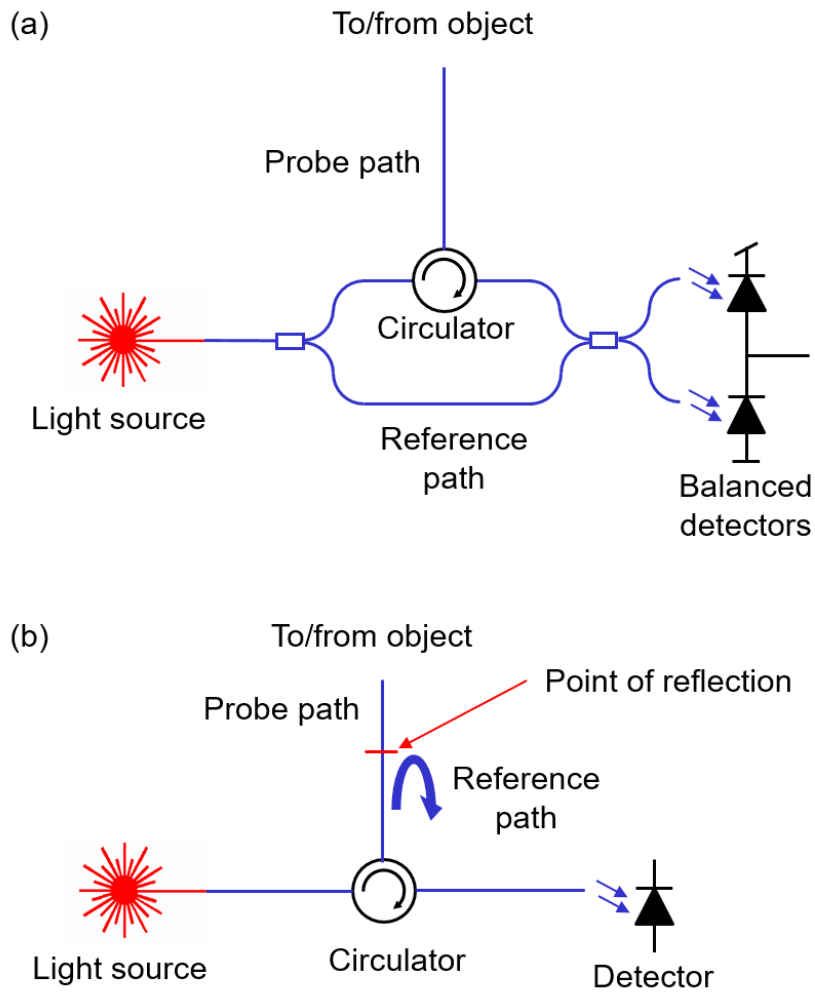

Figure 4-31. Reference path configurations of FMCW LiDAR.

(a) Separate reference and probe paths by an MZI architecture. (b) Reference path by a reflection along the probe path.

Typically the optical power in the reference path is much higher than in the probe path, i.e. $P_{\mathrm{ref}} >> P_{\mathrm{rx}}$. Under this assumption, the shot noise ASD can be approximated as

$$\sigma_{\mathrm{shot}}(f) = G_{\mathrm{TIA}}\sqrt{2eRP_{\mathrm{ref}}}\,. \tag{4-25}$$

Therefore the shot-noise limited SNR is

$$SNR_{\mathrm{shot}} = \frac{\sigma_{\mathrm{signal}}}{\sigma_{\mathrm{shot}}} = \sqrt{\frac{RP_{\mathrm{rx}}}{4e}T\exp\left(-\frac{2\tau}{\tau_{\mathrm{c}}}\right)}, \tag{4-26}$$

which is independent of the referent path optical power. This result indicates that as long as the detection is shot noise limited, the SNR will not be affected by the optical power in the reference path.

To make sure the detection is shot noise limited i.e. the shot noise is the dominant noise component, we now inspect the other two fundamental noise components, i.e. the thermal noise and laser RIN. According to section 2.4.1, the thermal noise ASD is

$$\sigma_{\text{thermal}}(f) = \sqrt{4k_{\text{B}}T_{\text{temp}}G_{\text{TIA}}}. \tag{4-27}$$

Compare it with the shot noise, when the shot noise is dominant, we have

$$\begin{aligned} \sigma_{\text{shot}}(f) &> \sigma_{\text{thermal}}(f), \\ G_{\text{TIA}}\sqrt{2eRP_{\text{ref}}} &> \sqrt{4k_{\text{B}}T_{\text{temp}}G_{\text{TIA}}}, \\ P_{\text{ref}} &> \frac{4k_{\text{B}}T_{\text{temp}}}{2eG_{\text{TIA}}R}. \end{aligned} \tag{4-28}$$

Plug in the numerical values listed in Table 2-2, i.e. temperature T_{temp} = 300 K, TIA gain G_{TIA} = 16,000 V/A, and photodiode responsivity R = 0.95 A/W, we have

$$P_{\text{ref}} > \frac{4k_{\text{B}}T_{\text{temp}}}{2eG_{\text{TIA}}R} = 3.40\ \mu\text{W}. \tag{4-29}$$

According to section 2.4.1, ASD of the laser RIN is

$$\sigma_{\text{RIN}}(f) = G_{\text{TIA}}r_{\text{CMRR}}\sqrt{I_{\text{DC}}^2 \cdot RIN} = G_{\text{TIA}}r_{\text{CMRR}}\sqrt{R^2P_{\text{ref}}^2 \cdot RIN}. \tag{4-30}$$

Since the balanced detection scheme is not available when the back reflection is used as the reference path, the CMRR is now 0 dB, i.e.

$$\sigma_{\text{RIN}}(f) = G_{\text{TIA}}\sqrt{R^2P_{\text{ref}}^2 \cdot RIN}. \tag{4-31}$$

Compare it with the shot noise, when the shot noise is dominant, we have

$$\begin{aligned} \sigma_{\text{shot}}(f) &> \sigma_{\text{RIN}}(f), \\ G_{\text{TIA}}\sqrt{2eRP_{\text{ref}}} &> G_{\text{TIA}}\sqrt{R^2P_{\text{ref}}^2 \cdot RIN}, \\ P_{\text{ref}} &< \frac{2e}{R \cdot RIN}. \end{aligned} \tag{4-32}$$

Plug in the numerical values listed in Table 2-2, i.e. R = 0.95 A/W and RIN = -150 dBc/Hz, we have

$$P_{\text{ref}} < \frac{2e}{R \cdot RIN} = 337\ \mu\text{W}. \tag{4-33}$$

From Equation (4-29) and Equation (4-33), the shot noise limited detection can be achieved in our FMCW LiDAR when

$$3.40\ \mu\text{W} < P_{\text{ref}} < 337\ \mu\text{W}. \tag{4-34}$$

The optical power input to each channel of the fiber array in our FMCW LiDAR setup shown in Figure 4-29 is approximately 100 mW. A -34 dB reflection from the fiber array facet

and the on-chip grating coupler surfaces results in a reference path optical power of 39.8 μW, which is within the range derived above in Equation (4-34) for shot noise limited detection. Therefore, the SNR of the FMCW LiDAR system is determined by Equation (4-26), which does not depend on the optical power in the reference path. In other words, the SNR of our FMCW LiDAR system using the back reflection as the reference path should be the same as an FMCW LiDAR with the MZI architecture and balanced detection scheme, under the same beam scanner and object parameters.

4.4.3 3D imaging results

A representative beat signal spectrum from the FMCW LiDAR system with the 128×128 FPSA beam scanner is shown in Figure 4-32. The object spectral peak can be clearly seen in the spectrum with an SNR of approximately 28 dB. For each of the 128×96 beam steering angles, 10 distance measurements are repeated and the distance results are averaged to increase the ranging accuracy. An intensity threshold is applied to the measurement data points to filter out the noise.

3D point clouds captured by the FMCW LiDAR system with the 128×128 FPSA beam scanner of the three letters place on the same plane and different planes are shown in Figure 4-33. The points are color-coded by the *z* coordinates. The point clouds show that the shapes of the three letters are recovered with high fidelity, and the distance difference among the letters is also accurately measured. The results verify that the FPSA beam scanner works as the LiDAR transmitter and receiver as expected.

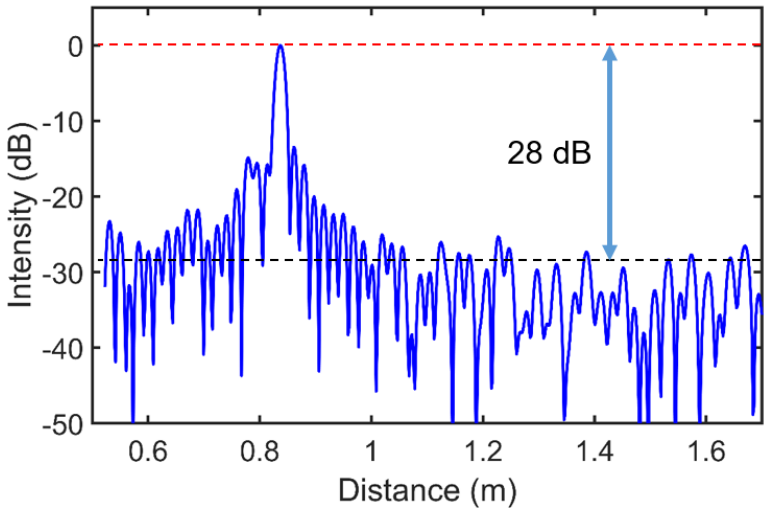

Figure 4-32. A representative FMCW LiDAR beat signal spectrum.

Several directions of optimization are worth pursuing to improve the performance of the FMCW LiDAR system with the FPSA beam scanner. (1) The SNR can be increased by reducing the optical loss in the FPSA beam scanner thus increasing the optical power of the returned light. According to Table 4-4, we expect to have a 16.2 dB roundtrip loss reduction on the FPSA chip by an improved fabrication process. With the higher SNR, objects at a longer distance or with lower reflectivity can be detected. (2) The polarization states of light in the fiber-based LiDAR system can be stabilized by using polarization-maintaining fibers for the optical paths and fiber components, which leads to a better polarization alignment of the probe and reference light at the

photodetector thus improves the SNR. (3) The reflection at the fiber array facet can be reduced by applying index matching gel, therefore an MZI architecture with full control on the reference light power and polarization as well as the balanced detection scheme can be used for the FMCW LiDAR system. (4) In the future, full integration of the LiDAR setup and the FPSA beam scanner on the silicon photonics platform is a promising direction towards a chip-scale solid-state FMCW LiDAR.

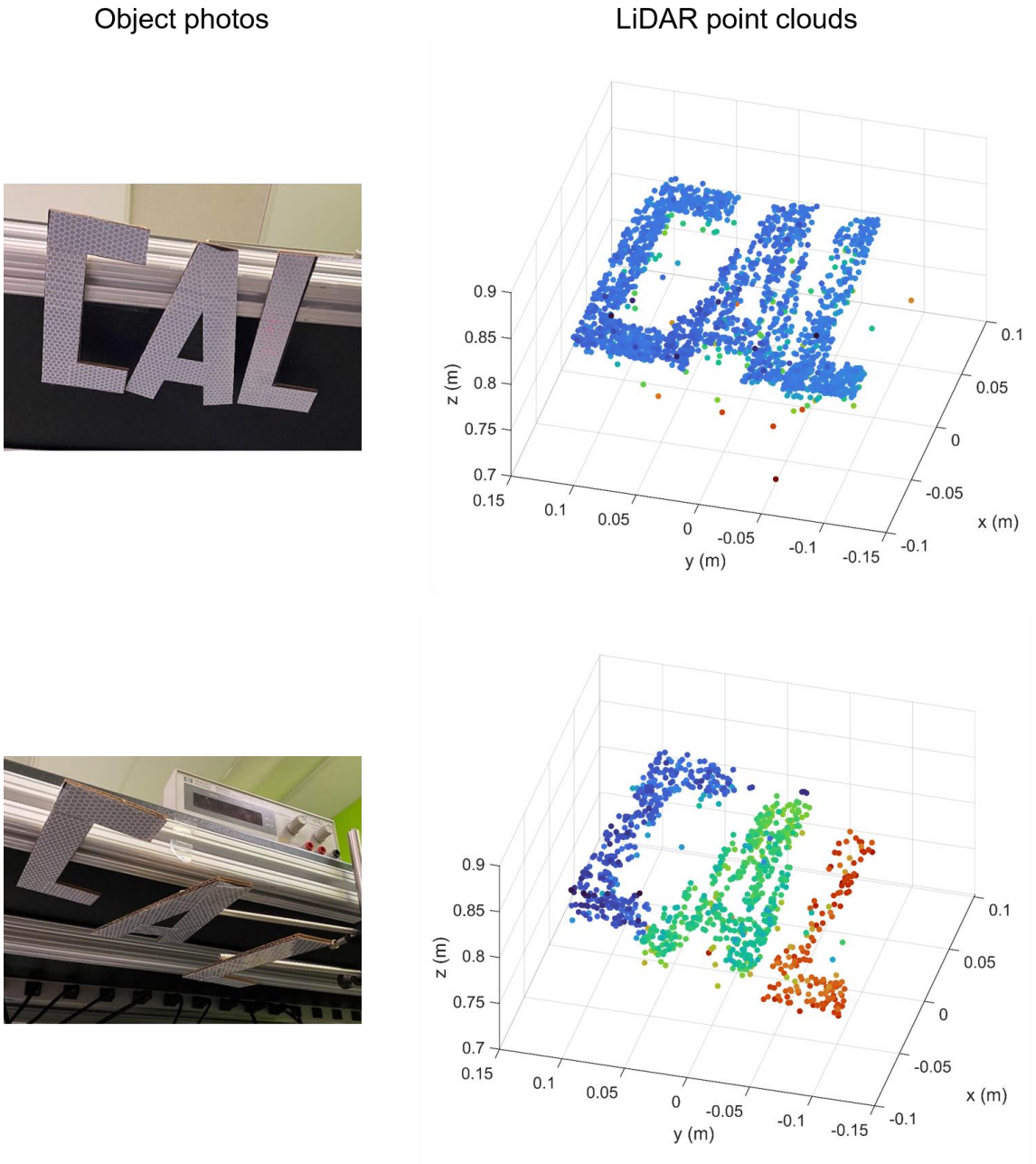

Figure 4-33. 3D point clouds measured by the FMCW LiDAR with FPSA beam scanner.

4.5 Chapter summary

In this chapter, we introduced the principle, parameters, common architectures, advantages, and challenges of the FPSA beam scanners. Some approaches to achieve continuous beam steering are also discussed. We then reported on a 20×20-element FPSA beam scanner and a 128×128-element FPSA beam scanner. Finally, we demonstrated 3D imaging by an FMCW LiDAR system with the 128×128-element FPSA beam scanner.

With the MEMS optical switch and the row-column addressing 2D array architecture, highly scalable 2D FPSA with a small pitch, large array size, high optical efficiency, fast response speed, and low power consumption can be realized. The wide selection of device lenses also introduces large flexibility in the FPSA beam scanner parameters such as beam steering FoV, resolution, and divergence to meet the requirements of various applications.

Beyond the LiDAR application, FPSA beam scanners can also be applied in optical beam steering for free-space optical communication [63], AR/VR display [64], ion probing for integrated quantum computing [65], etc. We believe this highly scalable architecture will be one of the mainstream beam scanner approaches for many solid-state systems.

The work in sections 4.2 and 4.3 of this chapter was performed in collaboration with Dr. Kyungmok Kwon. I also would like to thank Johannes Henriksson and Jianheng Luo for their contributions in the MEMS optical switch design [54][55].

5 Summary

5.1 Summary of this dissertation

In this dissertation, we explored some paths towards a high-performance integrated LiDAR sensor.

3D imaging sensors are important for the surrounding perception in modern intelligent and autonomous machines. Among various 3D senor principles, LiDAR has unique benefits in the high distance and lateral resolutions, which lead to more accurate 3D object reconstructions and classifications.

A scanning LiDAR is composed of a laser ranging system and an optical beam scanner. Compared with conventional laser ranging principles such as the pulsed time-of-flight (ToF) or amplitude-modulated continuous-wave (AMCW), frequency-modulated continuous-wave (FMCW) laser ranging employs the coherent detection scheme thus requires lower peak optical power and lower electronic bandwidth. It is intrinsically immune to interference from the ambient light or other LiDAR transmitters. Furthermore, it can detect the object velocity together with the distance at the same measurement.

A linearly frequency chirped laser with low phase noise is crucial for an FMCW LiDAR in order to achieve a long distance range and a high resolution. Instead of the complicated feedback control circuits or the computation-heavy resampling processing, in Chapter 2 we introduced a laser chirp linearization method by iterative learning pre-distortion of the drive waveform and a laser phase noise compensation method by using the information from a monitor MZI. Experimental results on a commercial DFB laser show that the laser chirp nonlinearity is reduced by 140× and 600× in the up and down-chirps after the iterative learning pre-distortion process, and the LiDAR distance range is extended to more than 150 m by the phase noise compensation method. These two methods have a simple setup and data processing, and can be applied to any type of lasers to realize a practical and low-cost FMCW LiDAR system with high performance.

Conventional optical beam scanners are mechanically rotating mirrors that are not compatible with solid-state LiDAR sensors. In this dissertation, we introduced two integrated optical beam scanner architectures. An optical phased array (OPA) steers the far-field angle of the output beam by controlling the amplitude and phases throughout the array of antennas. In chapter 3 we reported on a 160×160-element grating-based 2D MEMS OPA. Optical phase of the -1st order diffraction beam of the grating can be shifted by moving the grating in the device plane with comb-drive MEMS actuators. This design enables large-scale OPA with high-efficiency (>85%) and broadband operation (1200 – 1700 nm wavelength). The device achieves optical beam steering in a 6.6°×4.4° field-of-view (FoV) with a 0.040°×0.027° divergence and a 5.7 μs response time.

A focal plane switch array (FPSA) beam scanner steers the far-field angle of the output beam by turning on different optical antennas located on the back focal plane of the device lens. In Chapter 4 we reported on a 20×20-element and a 128×128-element 2D FPSA beam scanner with MEMS optical switches. The MEMS optical switch design offers low optical loss, a small footprint, fast response, and low power consumption. The row-column addressing scheme significantly reduces the number of electrical addressing signals. The digital switching operation of the FPSA as well as the independence between large FoV and small array pitch makes it a highly scalable integrated beam scanner architecture. The 20×20 FPSA beam scanner achieves optical beam steering in a 32°×32° FoV with a 1.7°×1.7° resolution, 0.064°×0.064° divergence,

and 1 μs response time. The large-scale 128×128 FPSA beam scanner achieves optical beam steering in a 70°×70° FoV with a 0.6°×0.6° resolution, 0.050°×0.050° divergence, and 2.7 μs response time.

Finally, we combined the FMCW ranging technologies and the FPSA beam scanners to demonstrate 3D imaging. The results show that the FPSA beam scanner is successfully implemented on the FMCW LiDAR to generate high-resolution 3D point clouds.

We believe the technologies reported in this dissertation make us one step closer to a high-performance chip-scale integrated LiDAR 3D sensor. We expect to see such LiDAR sensors being introduced to and widely used around the world in the near future.

5.2 Future directions

5.2.1 Discussions and future directions for FMCW LiDAR

In this section, we will discuss some directions of research and development that are worth to be explored in the future.

The laser performance is crucial for an FMCW LiDAR, therefore developing lasers with linear tuning capability and narrow linewidth is an important direction. A linear tunable laser that has an intrinsically linear relation between the applied voltage or current drive waveform and the laser frequency will eliminate the need for laser chirp linearization such can be directly implemented in FMCW LiDAR systems. The development of narrow-linewidth semiconductor lasers significantly extends distance range for coherent detection [66]. Besides the single wavelength lasers, advanced broadband laser sources like the optical frequency combs also open up new directions for FMCW LiDAR, such as the coherent combination of adjacent comb lines for a large chirp bandwidth [67], and the implementation of dispersive beam steering for ranging at multiple angles in parallel [68].

On the signal processing side, the FMCW LiDAR demands a high-speed Fourier Transform computation. Current implementations rely on the FFT algorithm running on a computer or an FPGA. The recent development of analog computing devices provides another approach for discrete Fourier Transform by the analog matrix multiplication operations, which can potentially speed up the signal processing [69]. On the FMCW beat signal spectrum, identifying the peaks corresponding to the same object when multiple moving objects are present is also a practical problem to be investigated into.

Thanks to the ability to detect Doppler shift, in addition to measuring the moving velocity of an entire object, the motions from moving parts on an object can also be detected by the FMCW LiDAR, for example, the rotating propellers on a drone and the flapping bird wings. These micro-Doppler effects can be analyzed by a joint time-frequency analysis of the beat signal by methods like short-time Fourier Transform or wavelet transform [70]. High-speed moving parts on an object can generate distinct micro-Doppler signatures that can be used for object classifications.

5.2.2 Discussions and future directions for integrated beam scanners

For the integrated beam scanners, optimizing the optical efficiencies and fully packaging the chips with mechanical mount, electrical controls, and optical input/outputs are some of the immediate steps to enhance the performance.

Novel optical antenna architecture with high optical efficiency and compact footprint is also a valuable direction to be explored. Some research works have proposed several new designs such as the 45° mirror at the waveguide end [71] or a vertical waveguide bend for vertical light emission [72]. Small footprint antennas can help achieve a high array density that enables large beam steering FoV for an OPA or high beams steering resolution for an FPSA beam scanner. Vertical emission can also increase the device lens collection efficiency for the antenna in the central area of the FPSA.

Integrated optical beam scanners working in a broad wavelength band are desired in LiDAR systems with multiple wavelengths, wavelength division multiplexing communications, as well as other novel applications like ion probing. Optical antennas based on grating structures usually output light at different wavelengths in different directions due to the grating dispersion. Novel optical antenna designs may also help achieve the same beam steering angle for multiple wavelengths.

The OPA and FPSA beam scanners both have random-access beam steering capability, therefore the beam steering pattern can be adjusted in real time. This provides opportunities on an adaptive LiDAR scanning FoV, for example, the regions with objects of interest are scanned with a higher resolution, and the regions without objects are scanned with a reduced resolution, which can reduce the amount of data and increase the LiDAR frame rate. Algorithms for point cloud data analyses, LiDAR data acquisition, and beam scanner control need to be designed based on the system specifications.

These directions of improvements and new functionalities together with a chip-scale integration of the LiDAR system with optical beam scanner will certainly enhance the performance of current 3D sensors and open up many novel applications in the future.

References

[1] B. Javidi, A. Carnicer, J. Arai, T. Fujii, H. Hua, H. Liao, M. Martínez-Corral, F. Pla, A. Stern, L. Waller, Q. Wang, G. Wetzstein, M. Yamaguchi, and H. Yamamoto, "Roadmap on 3D integral imaging: sensing, processing, and display," *Optics Express* **28**, 32266–32293 (2020).

[2] A. O'Riordan, T. Newe, G. Dooly, and D. Toal, "Stereo Vision Sensing: Review of existing systems," 2018 12th International Conference on Sensing Technology (ICST), 2018, pp. 178–184.

[3] Y. Yang, S. Jin, R. Liu, S. B. Kang, and J. Yu, "Automatic 3d indoor scene modeling from single panorama," in *Proceedings of the IEEE Conference on Computer Vision and Pattern Recognition* 2018, pp. 3926–3934.

[4] J. Geng, "Structured-light 3D surface imaging: a tutorial," *Advances in Optics and Photonics* **3**, 128–160 (2011).

[5] G. Allevato, J. Hinrichs, M. Rutsch, J. P. Adler, A. Jäger, M. Pesavento, and M. Kupnik, "Real-Time 3-D Imaging Using an Air-Coupled Ultrasonic Phased-Array," in *IEEE Transactions on Ultrasonics, Ferroelectrics, and Frequency Control* **68**, 796–806 (2021).

[6] M. A. Richards, Fundamentals of radar signal processing. McGraw-Hill Education, 2014.

[7] B. Behroozpour, P. A. M. Sandborn, M. C. Wu, and B. E. Boser, "Lidar system architectures and circuits," *IEEE Communications Magazine* **55**, 135–142 (2017).

[8] BIPM, "Resolution 1 of the 17th CGPM, Definition of the metre," the 17th Conférence Générale des Poids et Mesures (CGPM), 1983.

[9] T. Fortier, and E. Baumann, "20 years of developments in optical frequency comb technology and applications," *Communications Physics* **2**, 1–16 (2019).

[10] J. C. Owens, "Optical Refractive Index of Air: Dependence on Pressure, Temperature and Composition," *Applied Optics* **6**, 51–59 (1967).

[11] D. J. Lum, "Ultrafast time-of-flight 3D LiDAR," *Nature Photonics* **14**, 2–4 (2020).

[12] G. Wu, L. Liao, S. Xiong, G. Li, Z. Cai, and Z. Zhu, "Synthetic wavelength interferometry of an optical frequency comb for absolute distance measurement," *Scientific Reports* **8**, 1–7 (2018).

[13] C. Zhang, S. Y. Set, and S. Yamashita, "Enhancement in dynamic range of amplitude-modulated continuous-wave laser scanner having a coaxial configuration," *IEEE Transactions on Instrumentation and Measurement* **70**, 1–10 (2020).

[14] T. Hariyama, P. A. Sandborn, M. Watanabe, and M. C. Wu, "High-accuracy range-sensing system based on FMCW using low-cost VCSEL," *Optics Express* **26**, 9285–9297 (2018).

[15] J. T. Spollard, L. E. Roberts, C. S. Sambridge, K. McKenzie, and D. A. Shaddock, "Mitigation of phase noise and Doppler-induced frequency offsets in coherent random amplitude modulated continuous-wave LiDAR," *Optics Express* **29**, 9060–9083 (2021).

[16] J. Shi, J. Guo, M. Kagami, P. Suni, and O. Ziemann, "Photonic technologies for autonomous cars: feature introduction," *Optics Express* **27**, 7627–7628 (2019).

[17] Thorlabs, GVS102 - 2D Galvo System, Gold-Coated Mirrors. https://www.thorlabs.com/thorproduct.cfm?partnumber=GVS102

[18] S. T. S. Holmström, U. Baran, and H. Urey, "MEMS laser scanners: a review," *Journal of Microelectromechanical Systems* **23**, 259–275 (2014).

[19] K. Van Acoleyen, W. Bogaerts, and R. Baets, "Two-dimensional dispersive off-chip beam scanner fabricated on silicon-on-insulator," *IEEE Photonics Technology Letters* **23**, 1270–1272 (2011).
[20] S. D. Senturia, Microsystem design. Springer Science & Business Media, 2007.
[21] G. T. Reed, and A. P. Knights, Silicon photonics: an introduction. John Wiley & Sons, 2004.
[22] X. Zhang, J. Pouls, and M. C. Wu, "Laser frequency sweep linearization by iterative learning pre-distortion for FMCW LiDAR," *Optics Express* **27**, 9965–9974 (2019).
[23] A. Y. Alibhai, C. Or, and A. J. Witkin, "Swept source optical coherence tomography: a review," *Current Ophthalmology Reports* **6**, 7–16 (2018).
[24] K. Yuksel, M. Wuilpart, V. Moeyaert, and P. Mégret, "Optical frequency domain reflectometry: A review," in 11th IEEE International Conference on Transparent Optical Networks, 2009, pp. 1–5.
[25] B. Behroozpour, P. A. M. Sandborn, N. Quack, T. Seok, Y. Matsui, M. C. Wu, and B. E. Boser, "Electronicphotonic integrated circuit for 3D microimaging," *IEEE Journal of Solid-State Circuits* **52**, 161–172 (2017).
[26] P. A. M. Sandborn, T. Hariyama, and M. C. Wu, "Resolution-enhancement for wide-range non-linear FMCW lidar using quasi-synchronous resampling," in Imaging and Applied Optics 2017, OSA Technical Digest (online) (Optical Society of America, 2017), paper DW3F.3.
[27] X. Zhang, "Laser Chirp Linearization and Phase Noise Compensation for Frequency-modulated Continuous-wave LiDAR," M.S. Thesis, UC Berkeley, 2021.
[28] T. Fersch, R. Weigel, and A. Koelpin, "Challenges in miniaturized automotive long-range lidar system design," In Three-Dimensional Imaging, Visualization, and Display 2017, vol. 10219, p. 102190T. International Society for Optics and Photonics, 2017.
[29] Mathworks, "Power Spectral Density Estimates Using FFT," https://www.mathworks.com/help/signal/ug/power-spectral-density-estimates-using-fft.html.
[30] A. Vasilyev, "The Optoelectronic Swept-Frequency Laser and Its Applications in Ranging, Three-Dimensional Imaging, and Coherent Beam Combining of Chirped-Seed Amplifiers," Ph.D. Dissertation, Caltech, 2013.
[31] P. Sandborn, "FMCW Lidar: Scaling to the Chip-Level and Improving Phase-Noise-Limited Performance," Ph.D. Dissertation, UC Berkeley, 2019.
[32] J. W. Goodman, Introduction to Fourier optics. Roberts and Company Publishers, 2005.
[33] D. P. Resler, D. S. Hobbs, R. C. Sharp, L. J. Friedman, and T. A. Dorschner, "High-efficiency liquid-crystal optical phased-array beam steering," *Optics Letters* **21**, 689–691 (1996).
[34] J. Sun, E. Timurdogan, A. Yaacobi, E. S. Hosseini, and M. R. Watts, "Large-scale nanophotonic phased array," *Nature* **493**, 195–199 (2013).
[35] C. V. Poulton, M. J. Byrd, B. Moss, E. Timurdogan, R. Millman, and M. R. Watts, "8192-element optical phased array with 100° steering range and flip-chip CMOS," in Conference on Lasers and Electro-Optics, OSA Technical Digest (Optical Society of America, 2020), paper JTh4A.3.
[36] T. A. Bartlett, W. C. McDonald, and J. N. Hall, "Adapting Texas Instruments DLP technology to demonstrate a phase spatial light modulator," In Emerging Digital Micromirror Device Based Systems and Applications XI, (International Society for Optics and Photonics, 2019), paper 109320S.

[37] P. I. Oden, T. A. Bartlett, W. C. McDonald, J. C. Baker, and J. N. Hall, "Innovations with a massively paralleled, microelectromechanical systems (MEMS) toward piston-mode-based phase light modulator (PLM)," In Emerging Digital Micromirror Device Based Systems and Applications XII, (International Society for Optics and Photonics, 2020), Vol. 11294, p. 112940G.
[38] Y. Wang, G. Zhou, X. Zhang, K. Kwon, P.-A. Blanche, N. Triesault, K. Yu, and M. C. Wu, "2D broadband beamsteering with large-scale MEMS optical phased array," *Optica* **6**, 557–562 (2019).
[39] H. Larocque, L. Ranzani, J. Leatham, J. Tate, A. Niechayev, T. Yengst, T. Komljenovic, C. Fodran, D. Smith, and M. SoMani, "Nanophotonic Phased Arrays with Compact and Low Power Silicon Resonator Phased Shifters," in Conference on Lasers and Electro-Optics, OSA Technical Digest (Optical Society of America, 2020), paper STh3O.1.
[40] F. Ashtiani, and F. Aflatouni, "Optical Beam Steering Using an NxN Phased Array with 2N Phase Shifters," in Conference on Lasers and Electro-Optics, OSA Technical Digest (Optical Society of America, 2020), paper SM1O.1.
[41] A. Kazemian, P. Wang, Y. Zhuang, and Y. Yi, "Optimization of the silicon-based aperiodic optical phased array antenna," *Optics Letters* **46**, 801–804 (2021).
[42] P. Thureja, G. K. Shirmanesh, K. T. Fountaine, R. Sokhoyan, M. Grajower, and H. A. Atwater, "Array-scale inverse design of active metasurfaces," in Conference on Lasers and Electro-Optics, OSA Technical Digest (Optical Society of America, 2020), paper FW3B.4.
[43] Z. Kong, Y. J. Lee, A. A. Noman, Y. Tang, G. Chang, and M. Qi, "Design of 2D Optical Phased Array Emitters with Half-wavelength Spacing and Less Than -20 dB Crosstalk," in Conference on Lasers and Electro-Optics, OSA Technical Digest (Optical Society of America, 2020), paper AF3M.6.
[44] F. Bettonvil, "Fisheye lenses," *WGN, Journal of the International Meteor Organization* **33**, 9–14 (2005).
[45] H. Abe, M. Takeuchi, G. Takeuchi, H. Ito, T. Yokokawa, K. Kondo, Y. Furukado, and T. Baba, "Two-dimensional beam-steering device using a doubly periodic Si photonic-crystal waveguide," *Optics Express* **26**, 9389–9397 (2018).
[46] J. J. López, S. A. Skirlo, D. Kharas, J. Sloan, J. Herd, P. Juodawlkis, M. Soljačić, and C. Sorace-Agaskar, "Planar-lens enabled beam steering for chip-scale LIDAR," in Conference on Lasers and Electro-Optics, OSA Technical Digest (Optical Society of America, 2018), paper SM3I.1.
[47] D. Inoue, T. Ichikawa, A. Kawasaki, and T. Yamashita, "Demonstration of a new optical scanner using silicon photonics integrated circuit," *Optics Express* **27**, 2499–2508 (2019).
[48] H. Ito, Y. Kusunoki, J. Maeda, D. Akiyama, N. Kodama, H. Abe, R. Tetsuya, and T. Baba, "Wide beam steering by slow-light waveguide gratings and a prism lens," *Optica* **7**, 47–52 (2020).
[49] Y. Chang, M. C. Shin, C. T. Phare, S. A. Miller, E. Shim, and M. Lipson, "Metalens-enabled low-power solid-state 2D beam steering," in Conference on Lasers and Electro-Optics, OSA Technical Digest (Optical Society of America, 2019), paper SF3N.5.
[50] C. Li, X. Cao, K. Wu, X. Li, and J. Chen, "Lens-based integrated 2D beam-steering device with defocusing approach and broadband pulse operation for Lidar application," *Optics Express* **27**, 32970–32983 (2019).
[51] X. Cao, G. Qiu, K. Wu, C. Li, and J. Chen, "Lidar system based on lens assisted integrated beam steering," *Optics Letters* **45**, 5816-5819 (2020).

[52] C. Rogers, A. Y. Piggott, D. J. Thomson, R. F. Wiser, I. E. Opris, S. A. Fortune, A. J. Compston, A. Gondarenko, F. Meng, X. Chen, G. T. Reed, and R. Nicolaescu, "A universal 3D imaging sensor on a silicon photonics platform," *Nature* **590**, 256–261 (2021).
[53] E. H. Cook, S. J. Spector, M. G. Moebius, F. A. Baruffi, M. G. Bancu, L. D. Benney, S. J. Byrnes, J. P. Chesin, S. J. Geiger, D. A. Goldman, A. E. Hare, B. F. Lane, W. D. Sawyer, and C. R. Bessette, "Polysilicon grating switches for LiDAR," *Journal of Microelectromechanical Systems* **29**, 1008–1013 (2020).
[54] X. Zhang, K. Kwon, J. Henriksson, J. Luo, and M. C. Wu, "A 20x20 focal plane switch array for optical beam steering," in Conference on Lasers and Electro-Optics, OSA Technical Digest (Optical Society of America, 2020), paper SM1O.3.
[55] X. Zhang, K. Kwon, J. Henriksson, J. Luo, and M. C. Wu, "Large-scale Silicon Photonics Focal Plane Switch Array for Optical Beam Steering," in Optical Fiber Communication Conference (OFC) 2021, OSA Technical Digest (Optical Society of America, 2021), paper F4A.2.
[56] S. S. Polkoo, and C. K. Renshaw, "Hybrid imaging-based beam steering system using a sparse photonic integrated circuit outcoupling array," in Conference on Lasers and Electro-Optics, OSA Technical Digest (Optical Society of America, 2020), paper JTh2B.25.
[57] T. J. Seok, N. Quack, S. Han, R. S. Muller, and M. C. Wu "Large-scale broadband digital silicon photonic switches with vertical adiabatic couplers," *Optica* **3**, 64–70 (2016).
[58] K. Kwon, T. J. Seok, J. Henriksson, J. Luo, L. Ochikubo, J. Jacobs, R. S. Muller, and M. C. Wu, "128×128 Silicon Photonic MEMS Switch with Scalable Row/Column Addressing," in Conference on Lasers and Electro-Optics, OSA Technical Digest (online) (Optical Society of America, 2018), paper SF1A.4.
[59] T. J. Seok, K. Kwon, J. Henriksson, J. Luo, and M. C. Wu "Wafer-scale silicon photonic switches beyond die size limit," *Optica* **6**, 490–494 (2019).
[60] A. Michaels, and E. Yablonovitch, "Inverse design of near unity efficiency perfectly vertical grating couplers," *Optics Express* **26**, 4766–4779 (2018).
[61] S. Khajavi, D. Melati, P. Cheben, J. H. Schmid, Q. Liu, D. X. Xu, and W. N. Ye, "Compact and highly-efficient broadband surface grating antenna on a silicon platform," *Optics Express* **29**, 7003–7014 (2021).
[62] J. E. Tremblay, J. Henriksson, and M. C. Wu, "Polarization-Diversity Evanescent Coupler on Silicon with Integrated Polarization Splitter," in 2020 IEEE Photonics Conference (IPC), 2020, pp. 1–2.
[63] Y. Kaymak, R. Rojas-Cessa, J. Feng, N. Ansari, M. Zhou, and T. Zhang "A Survey on Acquisition, Tracking, and Pointing Mechanisms for Mobile Free-Space Optical Communications," *IEEE Communications Surveys & Tutorials* **20**, 1104–1123 (2018).
[64] F. Fidler, A. Balbekova, L. Noui, S. Anjou, T. Werner, and J. Reitterer, "Laser beam scanning in XR: benefits and challenges," in Optical Architectures for Displays and Sensing in Augmented, Virtual, and Mixed Reality (AR, VR, MR) II (Vol. 11765, p. 1176502). International Society for Optics and Photonics, 2021.
[65] J. Kim, S. Crain, C. Fang, J. Joseph, J. Kim, and P. Maunz, "Enabling trapped ion quantum computing with MEMS technology," in International Conference on Optical MEMS and Nanophotonics (IEEE, 2017).
[66] W. Jin, Q. F. Yang, L. Chang, B. Shen, H. Wang, M. A. Leal, L. Wu, M. Gao, A. Feshali, M. Paniccia, K. J. Vahala, and J. E. Bowers, "Hertz-linewidth semiconductor lasers using CMOS-ready ultra-high-Q microresonators," *Nature Photonics* **15**, 346–353 (2021).

[67] N. Kuse and M. E. Fermann, “Frequency-modulated comb LIDAR,” in Conference on Lasers and Electro-Optics, OSA Technical Digest (Optical Society of America, 2020), paper SM2N.3.
[68] J. Riemensberger, A. Lukashchuk, M. Karpov, E. Lucas, W. Weng, J. Liu, and T. J. Kippenberg, “Massively parallel coherent LiDAR using dissipative Kerr solitons,” in Conference on Lasers and Electro-Optics, OSA Technical Digest (Optical Society of America, 2020), paper SM2N.2.
[69] W. Haensch, T. Gokmen, and R. Puri, “The Next Generation of Deep Learning Hardware: Analog Computing,” *Proceedings of the IEEE* **107**, 108–122 (2019).
[70] V. C Chen, F. Li, S. S. Ho, and H. Wechsler, “Micro-Doppler effect in radar: phenomenon, model, and simulation study,” *IEEE Transactions on Aerospace and Electronic Systems* **42**, 2–21 (2006).
[71] J. Inoue, T. Ogura, K. Kintaka, K. Nishio, Y. Awatsuji, and S. Ura, “Fabrication of embedded 45-degree micromirror using liquid-immersion exposure for single-mode optical waveguides,” *Journal of Lightwave Technology* **30**, 1563–1568 (2012).
[72] Tomoya Yoshida, Syougo Tajima, Ryohei Takei, Masahiko Mori, Noboru Miura, and Youichi Sakakibara, “Vertical silicon waveguide coupler bent by ion implantation,” *Optics Express* **23**, 29449–29456 (2015).